Stefan Quabeck

Modeling of Parasitic Currents and Fault Detection in Electrical Traction Drives

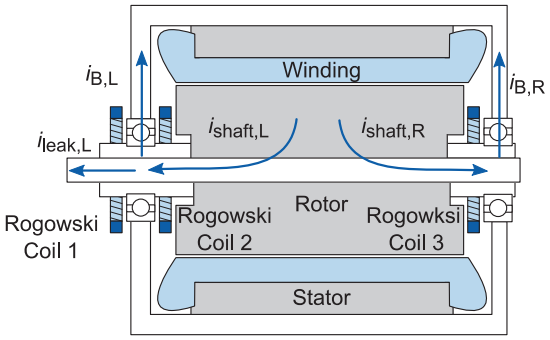

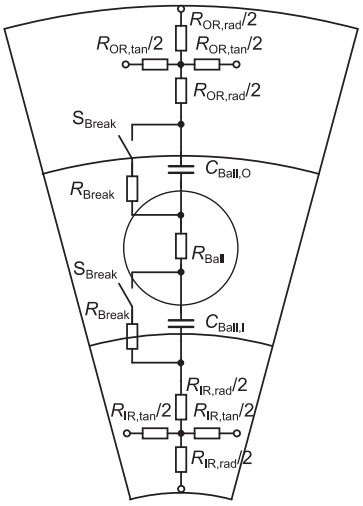

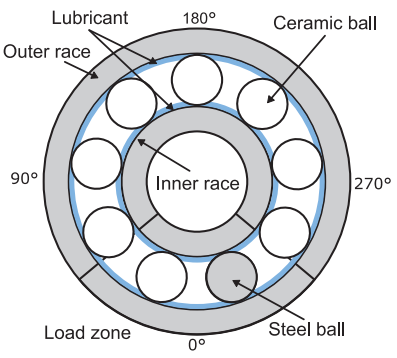

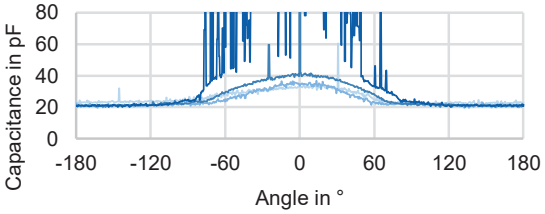

Aachener Beiträge des ISEA Band 170

Modeling of Parasitic Currents and Fault Detection in Electrical Traction Drives

Von der Fakultät für Elektrotechnik und Informationstechnik der Rheinisch-Westfälischen Technischen Hochschule Aachen zur Erlangung des akademischen Grades eines Doktors der Ingenieurwissenschaften genehmigte Dissertation

vorgelegt von
Stefan Quabeck, M. Sc.
aus Siegburg

Berichter:
Univ. Prof. Dr. ir. Dr. h. c. Rik W. De Doncker
Univ. Prof. Dr.-Ing. Annette Mütze

Tag der mündlichen Prüfung: 24. Februar 2023

AACHENER BEITRÄGE DES ISEA
Vol. 170

Editor:
Univ. Prof. Dr. ir. Dr. h. c. Rik W. De Doncker
Director of the Institute for Power Electronics and Electrical Drives (ISEA)
RWTH Aachen University

ISSN 1437-675X

Institute for Power Electronics and Electrical Drives (ISEA)
Campus-Boulevard 89 ▪ 52074 Aachen ▪ Germany
Tel: +49 (0)241 80-96920
Fax: +49 (0)241 80-92203
post@isea.rwth-aachen.de

Preface

Die vorliegende Dissertation ist im Rahmen meiner Tätigkeit als wissenschaftlicher Mitarbeiter am Institut für Stromrichtertechnik und Elektrische Antriebe (ISEA) der Rheinisch-Westfälischen Technischen Hochschule (RWTH) Aachen entstanden.

Mein besonderer Dank gilt meinem Doktorvater Professor Rik W. De Doncker für das in mich gesetzte Vertrauen und die Möglichkeit der Promotion am ISEA. Ebenso herzlich möchte ich mich bei Professorin Annette Mütze für die Übernahme des Koreferats bedanken.

Ich danke meinen Projektpartner*innen in den diversen Forschungsprojekten, die ich in der Zeit am ISEA bearbeiten durfte. Dabei sind besonders Roman Hudak und Francisco Gutierrez Guzman vom Institut für Maschinenelemente und Systementwicklung zu erwähnen, mit denen ich zahlreiche fachliche Diskussionen über Wälzlager führen durfte.

Dem gesamten ISEA danke ich für den fachlichen Austausch, die zahlreichen spannenden Events und den grandiosen Zusammenhalt in der Gruppe. Dabei gilt mein besonderer Dank natürlich der Antriebsgruppe, die mit zahlreichen Grillevents, Antriebsbieren und sonstigen Aktionen immer einen guten Ausgleich zur Arbeit geschaffen hat. Vivien Grau, Daniel Rodriguez Pinto, Xinyi Yu, und Alexander Stippich danke ich für 1.592 Kommentare und Korrekturvorschläge die einiges zur Verbesserung der Qualität dieser Arbeit beigetragen haben.

Neben den Kollegen haben mich auch zahlreiche Student*innen unterstützt, bei denen ich mich auch recht herzlich bedanken möchte. Meinen Abschlussarbeiter*innen Juri, Lukas, Berkay, Yaowen, Wenbo, Xinyi und Weihang danke ich für ihre Unterstützung bei meinen Forschungsprojekten, Veröffentlichungen und natürlich meiner Dissertation.

Meinen Eltern und meinen Geschwistern danke ich für ihre Unterstützung auf dem ganzen Weg bis zur Dissertation. Meinen Kindern Lotta und Lasse danke ich dafür, dass sie mir immer wieder gezeigt haben, dass es Dinge im Leben gibt, die deutlich wichtiger sind als Arbeiten. Zu guter Letzt gilt mein ganz besonderer Dank meiner Frau Laura, dafür, dass sie mir mit Ihrer Dissertation immer einen Schritt voraus war und so die Motivation ständig aufrechterhalten hat.

Abstract

The trend towards increasing integration of electric machine, inverter, and gearbox into an e-axle yields significant advantages in terms of power density and ease-of-use. Moreover, with the reduced size and increased temperature resilience of wide-bandgap semiconductors, the inverter can be integrated closer to the windings of the machine. This reduces cable length and increases the power density even further. However, this close integration also poses several new challenges that must be overcome. Parasitic capacitive and inductive coupling between the windings and other parts of the drive increases due to the close proximity. The combination of steep voltage slopes from the wide-bandgap devices and increased parasitic capacitances causes high parasitic currents to flow through the drive.

These parasitic currents can significantly reduce the lifetime of an electrical drive. They flow through the bearings and any components connected to the shaft, can cause severe damage to the bearings and gearbox, and deteriorate the insulation and the lubricants used in the machine. To understand the physical causes and to estimate parasitic currents inside electric machines, this work, therefore, presents a high-frequency model of an electrical machine. An automated parameter fine-tuning procedure helps to increase the model accuracy and reduces parameterization effort. The model is experimentally verified with a minimally-invasive bearing current measurement method. The model successfully predicts the amplitude of bearing voltages and is used to evaluate countermeasures, such as a shaft grounding brush. The effectiveness of this shaft grounding brush is confirmed with measurements.

However, faults are still bound to occur in the machine even when parasitic bearing currents are mitigated. For reliable electrical powertrains, fault detection is therefore essential. For this purpose, the frequency spectrum of the phase current can be analyzed, since it contains much more information than only the torque and speed of the machine. Many faults leave detectable signatures in the spectrum. The accuracy of traditional spectrum-based fault detection methods, however, severely depends on the operating point. This work proposes a combination of spectrum-based fault detection methods, information known from the controller, and machine learning. This combination leads to high fault detection and classification accuracy over the whole operating range. Even incipient faults are reliably detected.

Faults also influence the parasitic behavior of electric machines. This interdependence is investigated in detail and the occurrence of full and partial bearing voltage breakdowns

is analyzed. Thus, this thesis delivers an in-depth understanding of the parasitic effects in electric machines and how they are influenced by machine faults. While bearing faults cause more bearing voltage breakdowns to occur, for broken rotor bars, no such influence is observed.

Contents

1 Introduction

The development of electric machines started over two centuries ago with the first practical traction application dating back to 1835 [1]. Improving the power density and reliability of electrical drives has since been a key development objective. With the introduction of semiconductor-controlled variable-frequency drives in 1961, a completely new range of applications became viable [2]. In 1984, the insulated-gate bipolar transistor (IGBT) was invented [3]. Four years later, it was first employed in a variable frequency drive, increasing the efficiency and thus the power density of electrical drives significantly [4].

Electric machines driven by voltage-source inverters were not just subject to sinusoidal voltages and currents at a fixed frequency (e.g. 50 Hz), but also to high-frequency switching harmonics and common-mode (CM) voltages. Due to comparatively high voltage slopes, high-frequency switching harmonics and CM voltages that the new IGBT caused in electric machines, CM and bearing currents suddenly posed a problem for reliability at that time [5]. These high-frequency and CM voltages put additional stress on the windings and cause unwanted high-frequency currents to flow through the machine. These currents can reach amplitudes of several amperes and flow in a path that is not typically designed for current flow. The fast switching transients lead to high peak CM currents flowing through the machine. Moreover, when the inverter is connected to the machine with long cables, the high overvoltages from switching transients cause more stress on the insulation of the machine [6]. With the increased use of wide-bandgap (WBG) semiconductors in electrical drives, and the subsequent increase in voltage slopes, these problems arise anew.

The largest improvements in power density of electric machines in the past stem from more resilient winding insulation, which allowed to increase the operating temperatures. Integration of the whole drive, i.e., inverter, electric machine and, if required, a gearbox, is the next step in increasing the power density even further. With the reduced length of interconnections and combined housing of multiple components, system weight and volume can be reduced significantly. Shorter current paths often also mean reduced impedance, which reduces ohmic losses from the phase currents. However, with increasing integration of the inverter and the electric machine, the switching nodes of the voltage source inverters move into the machine and the parasitic current paths become shorter. Thus, the impedance of the parasitic current paths decreases, leading to an increase in CM currents and, consequently, an increase in bearing currents. Further, the space for filters and other countermeasures that mitigate these effects shrinks further and further. When integrating WBG inverters into an electric machine, parasitic effects inside that

machine therefore have to be considered carefully. In order to achieve a high lifetime of the machine, bearing currents and voltages need to be minimized.

While understanding the principles behind parasitic current flow in an electric machine can help improve machine design and reliability, faults are still bound to occur. Knowledge about the state-of-health of the electric machine can lessen the impact of these faults on machine operation, warning the user in due time before a critical fault occurs. The high-frequency voltages and currents flowing through an electric machine are often seen as disturbances for their control and are suppressed with filters. However, these high-frequency components contain information about different parts of the machine and can be used to estimate its state-of-health [7].

Aim of this Work and Statement of Novelty

This work aims to give an in-depth understanding of the modeling and measurement of parasitic effects in electric machines. To this end, a high-frequency machine model is developed. The parameterization of this model and the required measurements are described in detail. This process is automated using a particle swarm algorithm, allowing to quickly adapt this model to other machines.

While many other publications view the bearing as one lumped electric capacitance, this work provides a method for measuring the distributed bearing capacitance in an electrical machine, which varies with temperature, radial load, speed and angular position. The resulting model gives an in-depth understanding of the electrical behavior of rolling element bearings over a wide operating range.

Furthermore, this work provides an overview over classical fault detection methods in electric machines. These methods have several shortcomings, such as a low fault detection capability in low-load operating points. With the help of a k-nearest neighbor (k-NN) algorithm, this thesis shows how to overcome these shortcomings and achieve high fault detection accuracy over the whole operating range.

Finally, the influence of electric machine faults on the bearing voltage, on the bearing current, and on electric discharge machining (EDM) events is analyzed. These investigations deepen the understanding of fault propagation in electric machines and can additionally be used to develop fault detection methods based on the bearing current.

Outline of This Work

This thesis consists of three main chapters. Chapter 2 focuses on parasitic effects in electric machines. Chapter 3 deals with faults and fault detection in electric machines. Then, in chapter 4, the models and effects described in the two previous chapters are evaluated based on measurements, and interactions between faults in electric machines and these parasitic effects are shown.

Chapter 2: Parasitic Effects in Electric Machines

The second chapter focuses on parasitic effects in electric machines. First, the necessary fundamentals concerning electric machines, rolling element bearings, CM current, bearing current, and bearing voltage in electrical machines are presented. Then, a high-frequency machine model that includes these parasitic effects is developed. A parameterization procedure for this model and the required measurements are presented thereafter. Finally, methods of measuring bearing current and bearing voltage in electric machines are presented and compared in terms of suitability for the measurements to be conducted in chapter 4.

Chapter 3: Faults in Electric Machines

The third chapter investigates fault detection in electric machines. Traditional fault detection methods are presented and evaluated under varying operating conditions. Machine-learning methods help overcome the discovered shortcomings. Then, an algorithm for the automated detection of bearing voltage breakdowns is presented. Finally, it is shown that disturbances of the bearing current measurements from axial stray flux can be used to detect broken rotor bar faults.

Chapter 4: Evaluation

The fourth chapter investigates the interdependence of the bearing voltage, full and partial bearing voltage breakdowns, and electric machine faults. An in-depth analysis of full and partial breakdown events is given, showing a self-reinforcing relation between bearing faults and bearing voltage breakdowns.

Chapter 5: Conclusions and Outlook

The last chapter summarizes the previous chapters and highlights the contributions of this thesis. Finally, it gives an outlook on possible future work.

2 Parasitic Effects in Electric Machines

This chapter focuses on parasitic capacitances, leakage currents, and bearing currents in electric machines. In section 2.1, the electrical behavior of electric machines and different parasitic effects such as bearing currents are described. Next, section 2.2 presents how to incorporate these aforementioned effects into machine models and which measurements are required to parameterize these models. Finally, section 2.3 describes how to measure leakage current, bearing current and bearing voltage in electric machines.

2.1 Fundamentals

Besides the current flowing through the windings of an electric machine, there is unwanted current flow through several parasitic paths. The windings are capacitively coupled to all parts of the machine and apart from the desired magnetic coupling between the windings and the rotor, there is unwanted magnetic coupling between different parts of the machine, such as the coupling between the common-mode (CM) current path and the rotor and the stator. In order to understand the desired and undesired behavior of electric machines, their structure is briefly described in this section. Note that this work focuses on radial flux rotating field machines, which are the most widely used electric machines, and that the following sections are only valid for them. Many of the observations made in this work can, however, be applied to other types of electric machines as well.

2.1.1 Electric Machines

The axial cross section of an electric machine is shown in Figure 2.1. An electric machine consists of several phase windings that are usually connected in parallel or series to form three or more phases. These phase windings can be *concentrated*, meaning that there is only one winding per stator tooth and that the winding distribution is rectangular. Or the phase windings can be *distributed*, i.e., they span several stator teeth and that winding distribution approximates a sine wave. All analyses in this work are done on a three phase induction machine, but with small adaptations, they also apply to all other rotating machine types.

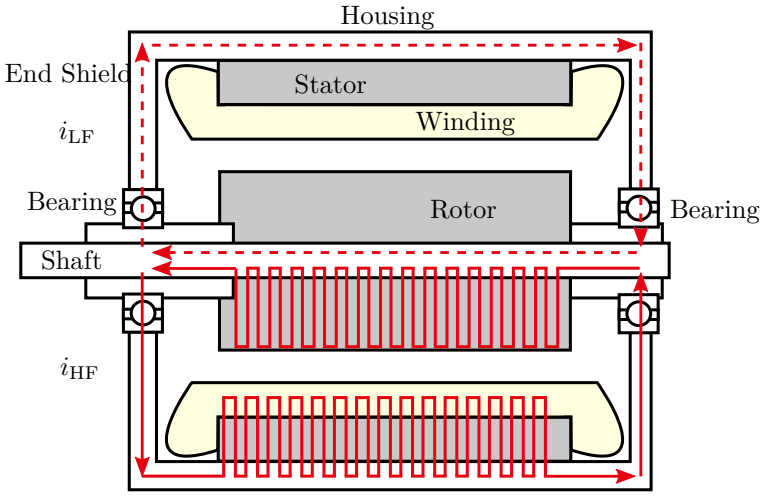

Figure 2.1: Axial cross section of an electric machine with low- and high-frequency circulating bearing current

The phase windings are located in the stator of the machine, which is made of laminated steel sheets. The rotor is also made of laminated steel sheets and can contain either permanent magnets, rotor windings, rotor bars, specially designed air gaps or a combination of them. The exact rotor topology is highly relevant for the design and control of these machines, since this determines the relation between current and torque. A detailed explanation on design, control and functionality of rotating field machines can be found in [8], [9] and [10]. When looking at high-frequency CM currents, however, the exact rotor design has little relevance. Because of the sheeted design, high-frequency currents in the axial direction, such as the inductive bearing current, which is induced by the CM current (c.f. section 2.1.4), will be subject to longer paths, and thus to a higher impedance than low-frequency currents. This is due to the proximity effect, which causes high-frequency currents to enter deep into the lamination instead of following the shortest current path through the housing and the shaft of the machine [11], [12]. This effect is illustrated in Figure 2.1. The current path of a low-frequency current i_{LF} is shown in the upper half of Figure 2.1 with the dashed red line. The noticeably longer current path of a high-frequency current i_{HF} is shown in the lower half of Figure 2.1 with the solid red line. The number of loops through the rotor and the stator of the machine serves only as an illustration. In reality, these loops occur per each laminated sheet, i.e., up to several hundred times. When comparing squirrel cage induction machines with other types of rotating field machines, the rotor impedance will be much lower and less frequency-dependent, since the rotor bars effectively short-circuit the iron sheets in the rotor [12].

The rotor is mounted on the shaft of the machine, which is then connected to the load either on one side or on both sides of the machine. The shaft is usually made of solid steel, and it is supported by two bearings, one on either side of the machine. In special cases such as liquid-cooled rotors or integrated e-axles with a differential, a hollow shaft can be used. In machines with only one end connected to the load, these bearings are referred to as driven end (DE) and non-driven end (NDE) bearings.

2.1.2 Bearings

Bearings are a peculiar part of electric machines. While they have no influence on the intended electrical behavior and traditionally fall under the field of activity of mechanical engineers, they exhibit a complex electrical behavior and are subject to parasitic currents. These currents can have a significant impact on their lifetime [13]. Therefore, in this section, the fundamentals of rolling element bearings with a focus on their electrical behavior is presented.

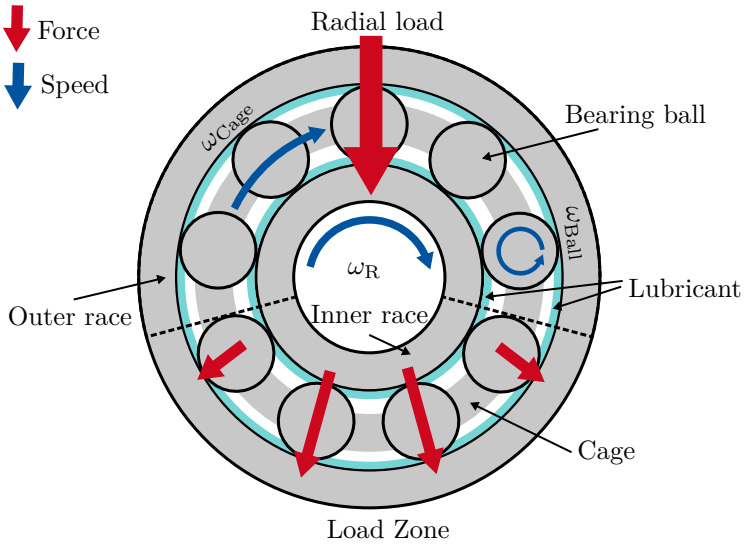

Figure 2.2: Radially loaded rolling element bearing

Figure 2.2 shows a radially loaded rolling element bearing. Rolling element bearings consist of an inner ring, an outer ring, several rolling elements and a lubricant, usually grease or different types of oil. The radial load applied to the inner ring (in the case of an electric machine, the gravitational force on the rotor and occasionally unbalanced magnetic pull) is distributed between the bearing balls in the load zone, which is located at the bottom of the bearing. The width of the load zone depends on the radial load. In electric machines, there will be some additional constant axial load since the bearings are spring-loaded to ensure that the minimum required load is always applied. However, it can be assumed that the radial load is dominant. The radial load and its distribution are depicted in red in Figure 2.2. The bearing balls in the middle of the load zone hold most of the load and the load decreases towards the borders of the load zone. Because of the increasing radial load, the load zone is also characterized by an increasing rotational speed ω_{Ball} of the rolling elements. The decreasing speed outside the load zone leads to slip of the bearing ball versus the raceway. The cage speed ω_{Cage}, i.e., the speed at which the bearing balls rotate around the shaft, is constant at approximately half of the shaft speed ω_{R} [14].

2.1.2.1 Lubrication

In lubricated bearings, a lubricant film forms between the rolling elements and the inner and outer raceways of the bearing. The thickness of this lubricant film depends on several factors: the *rotational speed* of the machine ω_{R}, which determines the cage speed of the bearing balls ω_{Cage} and their own rotational speed ω_{Ball}, the *contact pressure* ρ, which is determined by the radial load on the bearing ball, and the *lubricant viscosity* η, which exhibits a strong dependency on temperature. The viscosity ratio κ is often used to describe the lubrication regimes of a bearing:

$$\kappa = \frac{\eta}{\eta_0}, \tag{2.1}$$

where η_0 is the rated viscosity. Figure 2.3 shows the different lubrication regimes of a rolling element bearing along with the load carried by the lubricant film.

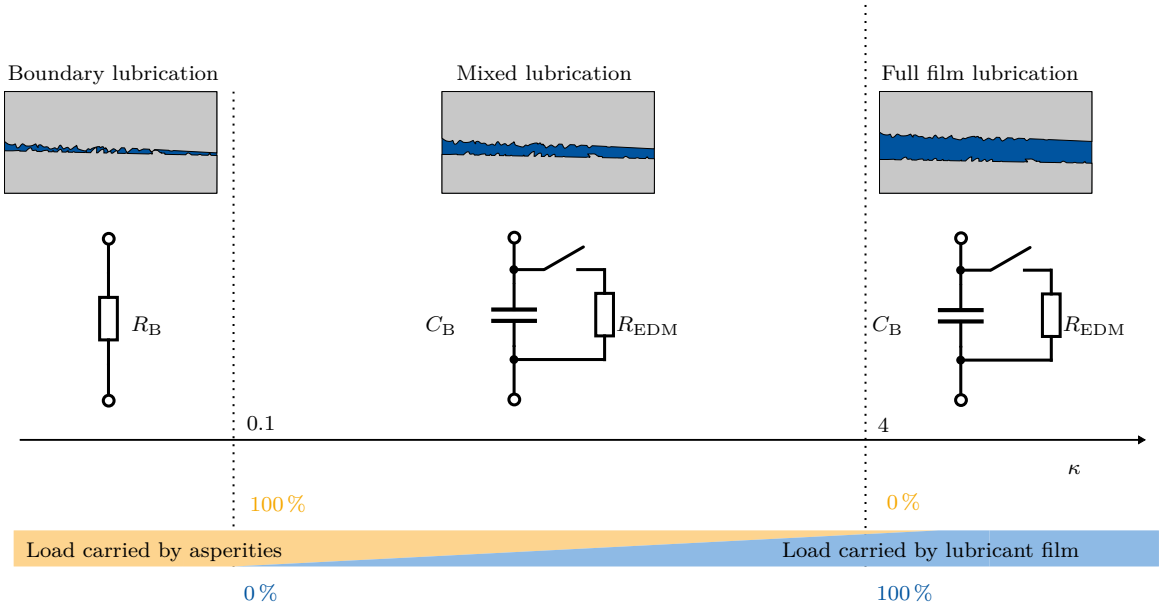

Figure 2.3: Lubrication regimes of a rolling element bearing for different viscosity ratios and equivalent electrical models [15]

For simplification, it is assumed that the radial load in an electric machine is constant. At a low speed, the bearing is in *boundary lubrication*. There is metallic contact between the bearing balls and raceways. The bearing thus exhibits a purely ohmic behavior and the bearing capacitance is short-circuited. At a higher speed, the lubricant film thickness increases and there is less contact between the bearing balls and the raceways. The bearing is thus in the *mixed lubrication* regime. The lubricant film is thicker than in boundary lubrication, but contact between the steel elements of the bearing still occasionally occurs. Furthermore, when the voltage applied to the bearing is too high, the lubricant film will break down. When the speed is increased further, the bearing enters the *full film lubrication* regime. The lubricant film is now fully formed and no contact

between the raceways and the bearing balls occurs. In this case, the bearing behaves purely capacitively. Lubricant film breakdowns caused by high bearing voltage can still occur. The lubricant film thickness of a rolling element bearing over speed for different lubricant temperatures is depicted in Figure 2.4.

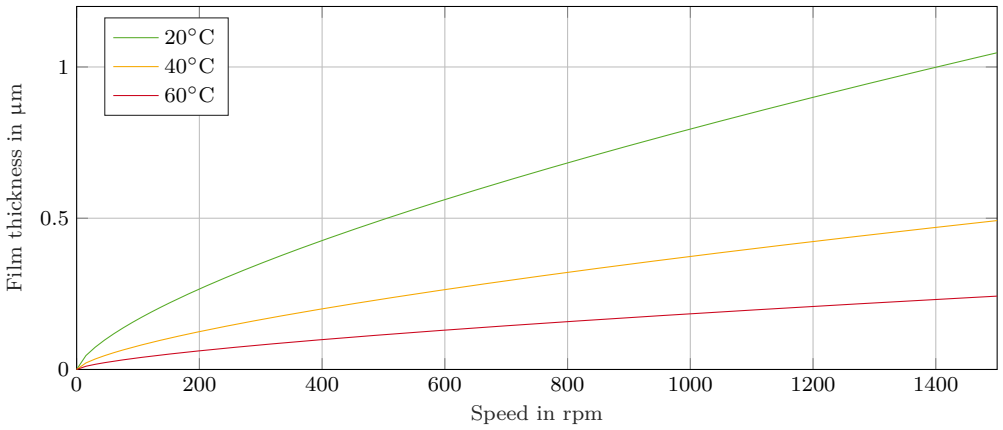

Figure 2.4: Lubricant film thickness over speed for different temperatures as per [16]

2.1.2.2 Bearing Capacitance

The parasitic capacitance of a rolling element bearing consists of three parts. The first part is the capacitance between the inner and outer raceway of the bearing $C_{\mathrm{B,IO}}$. Its value is determined by the geometry of the raceways and by the average dielectric properties of the materials between the raceways, i.e., the amount of air and lubricant. $C_{\mathrm{B,IO}}$ can be approximated as a cylindrical capacitor,

$$C_{\mathrm{B,IO}} = \frac{2\pi\epsilon W}{\ln\frac{d_{\mathrm{I}}}{d_{\mathrm{O}}}}, \tag{2.2}$$

where W corresponds to the width of the bearing, d_{I} corresponds to the diameter of the inner raceway d_{O}, corresponds to the diameter of the outer raceway and ϵ is the average dielectric constant of the mixture of lubricant and air in the bearing.

The second and third parts are the capacitances between the bearing balls and the inner raceway, $C_{\mathrm{B,I}}$, and the outer raceway, $C_{\mathrm{B,O}}$. They are often calculated from the lubricant film thickness h and the so-called Hertzian contact area A_{Hertz} , and they are modeled as a parallel plate capacitor,

$$C_{\mathrm{B,I}} = K\frac{\epsilon_{\mathrm{Lubricant}} A_{\mathrm{Hertz}}}{h_{\mathrm{I}}} \tag{2.3}$$

and

$$C_{\mathrm{B,O}} = K\frac{\epsilon_{\mathrm{Lubricant}} A_{\mathrm{Hertz}}}{h_{\mathrm{O}}}. \tag{2.4}$$

Note that the equation for the parallel plate capacitor is multiplied with a factor K, which varies depending on the publication [17]. This is because, as it can be noted in Figure 2.5, the electric field lines also extend outside the very small Hertzian contact area. These stray fields make up a large portion of the capacitance value.

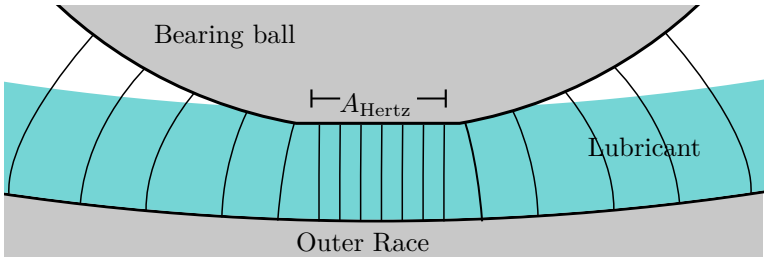

Figure 2.5: Illustration of electric field lines and Hertzian contact area between a bearing ball and the outer raceway of the bearing

In radially loaded bearings, the load is distributed non-uniformly between the bearing balls. Assuming that the gravitational force on the rotor is the main force component, the load zone (and with it also the point with the highest load) is located at the bottom of the bearing. The combination of high load and high rotational speed, as discussed in the previous section, leads to a low lubricant film thickness in the middle of the load zone (0°). Since equation (2.3) shows that the parasitic capacitance of an individual bearing ball is inversely proportional to the lubricant film thickness h, the bearing ball capacitance is maximal when the ball is a the bottom of the bearing, it decreases towards the borders of the load zone and it is constant outside of the load zone. The expected capacitance of one bearing ball over one rotation within the bearing is shown in Figure 2.6. This capacitance profile is expected to be similar for the inner and outer raceways with slight differences due to the bending of the surface.

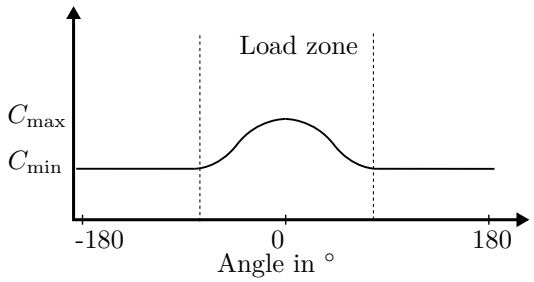

Figure 2.6: Expected parasitic capacitance of one bearing ball over one rotation

These three capacitances can either be added up (in the case of the ball-to-raceway capacitances after multiplication with the number of bearing balls) and used in a lumped model, or they can be used separately in a distributed model. Both types of models are presented in section 2.2.5.

2.1.3 Common Mode Current

The CM current is the most widely known type of parasitic effect in electric machines. It is caused by the CM voltage applied to the machine and flows through its parasitic capacitances. In a machine that is excited by a CM-free voltage (e.g. three perfect sine waves with a phase shift of 120°), no CM currents occur. However, since most machines in electric traction drives are driven by two-level inverters, usually, no CM-free voltage can be applied. Even when using three-level inverters and applying CM-free modulation schemes as in [18], the instantaneous CM voltage during the switching events will not be zero due to the dead time of the inverter. Therefore, the CM voltage and the CM current have to be considered in all electric traction drives. Figure 2.7 illustrates the path of the CM current through the machine. The current flows through the parasitic capacitances C_{WS},C_{WR}, and C_{RS} (capacitances between winding and stator, winding and rotor, and rotor and stator, respectively), and through the bearing. The current loop then closes over the ground connection between the machine and the inverter.

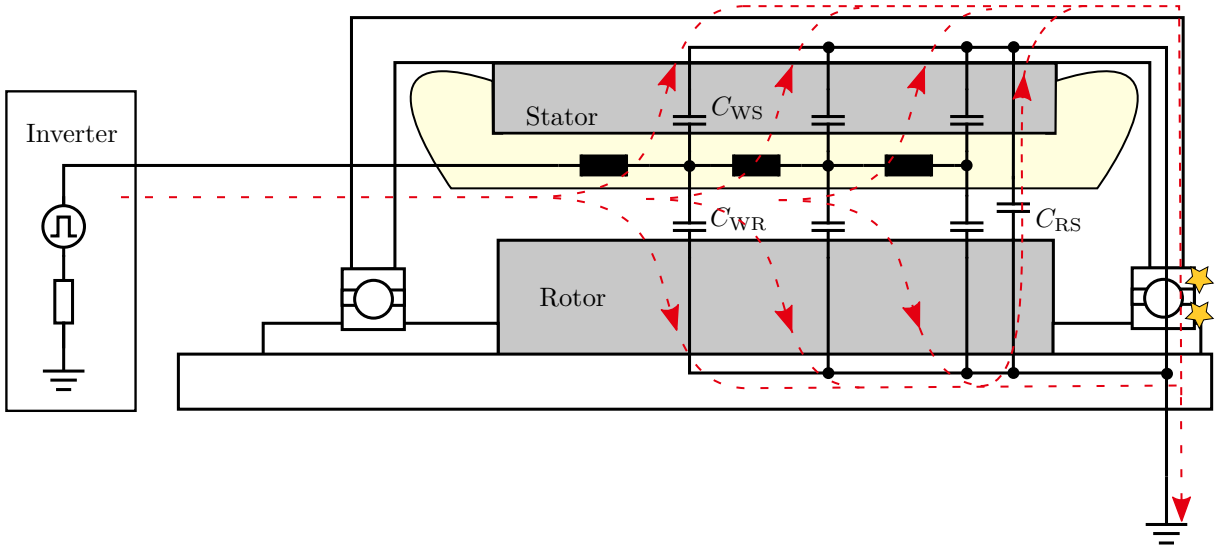

Figure 2.7: CM current path

2.1.4 Bearing Current

As already mentioned in the previous section, a part of the CM current flows through the bearing. The CM current is only one of three parasitic effects that cause current flow in the bearing. How detrimental the current flowing through the bearing is to its lifetime strongly depends on its amplitude and frequency of occurrence. There have been different approaches in the literature to classify bearing currents into harmful and non-harmful currents.

The *apparent bearing current density* is the amplitude of the bearing current divided by the Hertzian contact area of a bearing ball [6].

$$J_{\mathrm{B}} = \frac{i_{\mathrm{b}}}{A_{\mathrm{Hertz}}} \tag{2.5}$$

An apparent bearing current density below $0.3\,\mathrm{Amm}^{-2}$ is assumed to be uncritical while a bearing current density above $0.8\,\mathrm{Amm}^{-2}$ is deemed critical for the bearing lifetime [19].

Tischmacher [20] introduces the bearing apparent power (BAP)

$$S_{\mathrm{B}} = v_{\mathrm{B}} \cdot i_{\mathrm{b}} \tag{2.6}$$

as a means of identifying harmful bearing current events . The investigations conducted in [20] show that below a limit of $S_{\mathrm{B}} = 20\,\mathrm{VA}$, no damage is expected; while above $S_{\mathrm{B}} = 60\,\mathrm{VA}$, the bearing is sure to be damaged by the current.

Both evaluation methods have advantages and disadvantages. While the apparent bearing current density only requires bearing current measurements, BAP additionally requires bearing voltage measurements. Conversely, BAP does not require any further knowledge about the bearing's lubrication condition, load and speed, i.e., the Hertzian contact area.

2.1.4.1 Inductive Bearing Current

The first effect to mention are inductive or circulating bearing currents. Magnetic fields tangential to the machine induce circular currents that flow through the shaft, one bearing, the stator and back to the shaft through the second bearing. These fields can be caused by magnetic asymmetries in the machine or by CM current flowing through the machine in the axial direction. While magnetic asymmetries are minimized as much as possible during design and production, they are still present due to inaccuracies in production.

But even in a perfectly symmetrical machine, the CM current flows from the phase connections to the ground connection of the machine. Unless the CM current path is very carefully designed, part of the CM current will flow in the axial direction and thus cause inductive bearing currents. The end-to-end shaft voltage V_{Shaft} is usually considered to estimate the circulating bearing currents, since these bearing currents cannot be measured from outside the machine. It is important to note, however, that inductive bearing currents play a larger role in large-scale machines such as generators for power plants or wind turbines [6].

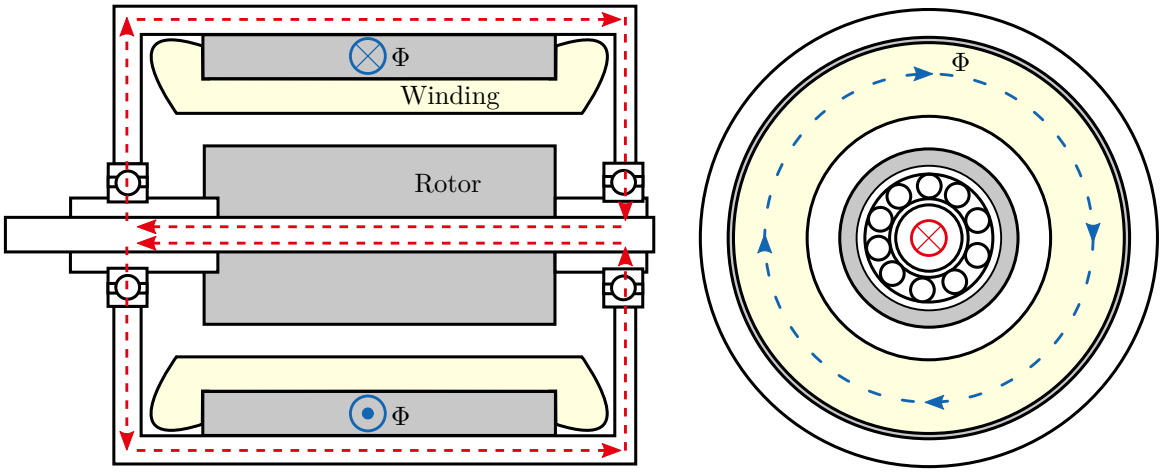

Figure 2.8: Inductive bearing current path

2.1.4.2 Capacitive Bearing Current

The second effect is the one already mentioned in section 2.1.3. When a CM voltage is applied to the machine, a CM current flows through it. The ratio between the CM current and the capacitive current $i_{\mathrm{B,cap}}$ flowing through one bearing can be estimated from the capacitive current divider [21].

$$i_{\mathrm{B,cap}} = i_{\mathrm{CM}} \cdot \frac{C_{\mathrm{B}}}{2C_{\mathrm{B}} + C_{\mathrm{RS}}} \cdot \frac{C_{\mathrm{WR}}}{C_{\mathrm{WR}} + C_{\mathrm{WS}}} \tag{2.7}$$

2.1.4.3 Bearing Breakdown Current

A part of the CM voltage is applied to the bearing. This voltage is called *shaft voltage* in many publications. To avoid confusion between the shaft-to-ground voltage and the end-to-end shaft voltage V_{Shaft}, the shaft-to-ground voltage will be called *bearing voltage* or v_{B} in this work. The shaft-to-ground voltage is equal to the voltage applied to the bearing unless an additional insulation layer is introduced between the bearing and the stator or the rotor. The bearing voltage can be calculated from the capacitive voltage divider as

$$v_{\mathrm{B}} = v_{\mathrm{CM}} \cdot \frac{C_{\mathrm{WR}}}{C_{\mathrm{WR}} + C_{\mathrm{RS}} + 2C_{\mathrm{B}}}. \tag{2.8}$$

The ratio between the CM voltage and the bearing voltage is also called the bearing voltage ratio (BVR). The bearing voltage v_{B} that is calculated from this BVR is often taken as an estimate to easily assess whether a bearing will be subject to electric discharge machining (EDM) currents. However, there is no fixed limit of bearing voltage at which EDM currents occur. The lubricant film in the bearing insulates the bearing balls from the bearing raceways and thus forms the dielectric of the parasitic capacitance between those parts of the bearing. The breakdown voltage of this lubricant film strongly depends

on its thickness and dielectric properties. Several publications aim to measure the bearing capacitance and breakdown voltage under different operating conditions [22]–[24].

The breakdown current itself strongly depends on the breakdown resistance R_{EDM} and the energy stored in the bearing capacitance E_{EDM}. Assuming that the inductances inside the bearing are negligible and the breakdown current is thus critically dampened, the breakdown current can be estimated as follows.

$$i_{\mathrm{b}}(t) = \frac{v_{\mathrm{B}}(t=0)}{R_{\mathrm{EDM}}} \cdot e^{\frac{t}{R_{\mathrm{EDM}} C_{\mathrm{B}}}} \tag{2.9}$$

The minimum energy that is discharged into the bearing can be calculated as

$$E_{\mathrm{EDM}} = \int_0^{\mathrm{inf}} v_{\mathrm{B}}(t) \cdot i_{\mathrm{b}}(t) \mathrm{d}t = \int_0^{\mathrm{inf}} \frac{(v_{\mathrm{B}}(t=0) \cdot e^{\frac{t}{R_{\mathrm{EDM}} C_{\mathrm{B}}}})^2}{R_{\mathrm{EDM}}} \mathrm{d}t = \frac{C_{\mathrm{B}} {v_{\mathrm{B}}}^2(t=0)}{2} \tag{2.10}$$

This means that the energy discharged into the bearing during a breakdown only depends on the bearing voltage v_{B} and the bearing capacitance C_{B}. In reality, the breakdown behavior will not be purely resistive. Instead, it will be similar to other breakdown phenomena with a certain forward voltage, a resistive part during breakdown and a certain threshold below which the breakdown current is extinguished. The breakdown resistance itself is likely not constant over the course of one breakdown but it will change with the local increase in temperature. Investigating and modeling the breakdown effect itself is, however, not part of this thesis and thus the resistive modeling approach will be used in the remaining part of the thesis. Section 2.2.5 includes a short explanation on how to integrate these nonlinear effects into the model.

In addition to a breakdown caused by a high bearing voltage, the bearing capacitance can also be quickly discharged when a direct contact between the bearing balls and raceways occurs. This can happen, for example, when the bearing leaves hydrodynamic lubrication because of a decrease in speed, or an increase in temperature or in static or dynamic radial load, e.g. due to a point defect in the bearing.

Based on the distributed bearing model presented in section 2.2.5, a second breakdown phenomenon can be derived theoretically. The bearing capacitance over one bearing ball is split into the capacitance between the ball and the inner raceway $C_{\mathrm{B,I}}$ and the capacitance between the ball and the outer raceway $C_{\mathrm{B,O}}$. Thus, a breakdown will always initially occur at only one of these capacitances. If the conditions are right, i.e., if the shaft voltage is high enough, the other capacitance will break down immediately afterwards, making the event look like a single breakdown. This is shown by the measurements conducted in section 4.2. Depending on the voltage amplitude and the cause of the initial breakdown, it is also possible that the second breakdown does not occur at all. This type of breakdown event will be called *partial bearing breakdown* and can be observed in shaft voltage measurements. It is important to note that the bearing voltage does not break down to 50 % of its initial value during a partial breakdown. Instead, the ratio of

the voltage amplitude before and after the breakdown varies greatly even under the same conditions. Section 4.2.3 elaborates further on this. Section 2.2.8 shows that the value of $C_{\mathrm{B,O}}$ and $C_{\mathrm{B,I}}$ changes as a function of the position of the bearing ball, even when the total bearing capacitance is constant.

2.2 Modeling of Parasitic Effects

There is extensive literature on the electrical behavior of electric machines [8]–[10]. The different modeling approaches range from simple steady-state lumped parameter models ,to models including an ideal rotating transformer, and up to models with separate circuits for the d- and q-axis of a machine. All these models serve the purpose of understanding, modeling and controlling the intended low-frequency behavior of the machine. While some models (in addition to the fundamental frequency) consider skin effect and higher order harmonics, none of the aforementioned models include the high-frequency electrical behavior of electric machines.

The simplest approach used to model capacitive currents and the bearing voltage v_{B} in electric machines is a purely capacitive model, e.g. [11], [25]–[27]. Other publications, such as [6], [12], [28], [29] use per-phase models with the inductive and resistive behavior of the phases included, offering a more precise model over a wider frequency range.

In the following sections, a high-frequency model of an electrical drive train, which includes inverter, cable and electrical machine, is developed. The model can be supplied with measured voltage waveforms. If no measured waveforms are available or if the simulation time has to be short, the input voltages can be synthesized in MATLAB® by providing the following parameters: switching speed, modulation index, dc-link voltage and switching frequency. The electric machine and the inverter do not necessarily share a common ground potential. The model outputs are the CM voltage with reference to the inverter midpoint, the star-point voltage with reference to machine ground, the CM current as well as the bearing currents and voltages for both the DE and the NDE bearing. An overview of the model is shown in Figure 2.9. The model includes capacitive and inductive bearing currents and allows asymmetrical states of the machine windings and the motor cable.

The model consists of a simplified representation of an inverter, a cable model, N_{ph} (Number of phases, in this case three) coupled phase winding models, and a model of the rotor and stator of the machine, including the bearings. These models are interconnected at various points and can be reconfigured according to the utilized grounding concept. The machine cable can be parameterized separately from the rest of the model, allowing to test the influence of different cable configurations such as shielded vs. unshielded cables, cable length, connection of the shield etc. The model is based on the study published in [30].

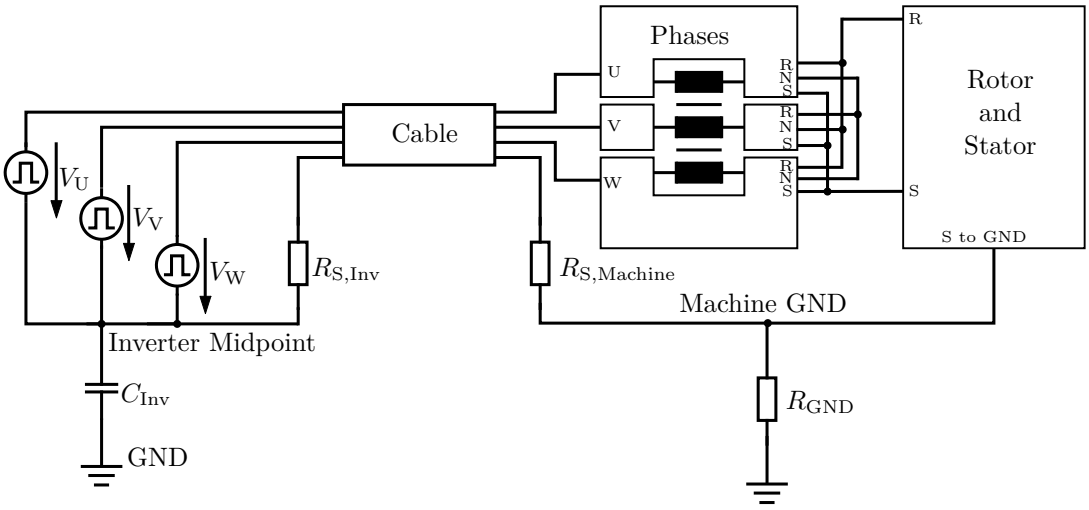

Figure 2.9: Full equivalent circuit model

2.2.1 Inverter Model

The inverter is modeled as N_{ph} voltage sources connected to a common reference potential on one side and to the phase connections of the machine on the other side. The reference potential can either be the inverter midpoint or the DC- or DC+ terminal. In this work, the midpoint is chosen as a reference, since a grounded midpoint should in theory lead to the lowest CM voltage amplitudes. The voltage waveforms that are fed into the voltage sources in the model should be referenced to the correct reference potential. Either measured voltage waveforms or synthetic waveforms, e.g. generated in MATLAB®, can be used. All the parasitic capacitances from the inverter to ground are lumped into the inverter parasitic capacitance C_{Inv}. The inverter model is shown in the left part of Figure 2.9.

2.2.2 Cable Model

The cable is modeled as a simple π-equivalent circuit, similar to the models presented in [6], [27]. When considering very long cables, a distributed cable model could also be used. For the reduction of computational complexity the simpler π-equivalent circuit was used in this work.

2.2.3 Phase Winding Model

There are many different approaches for modeling the high-frequency behavior of the phases of an electric machine. In [28], four different phase models are compared, showing

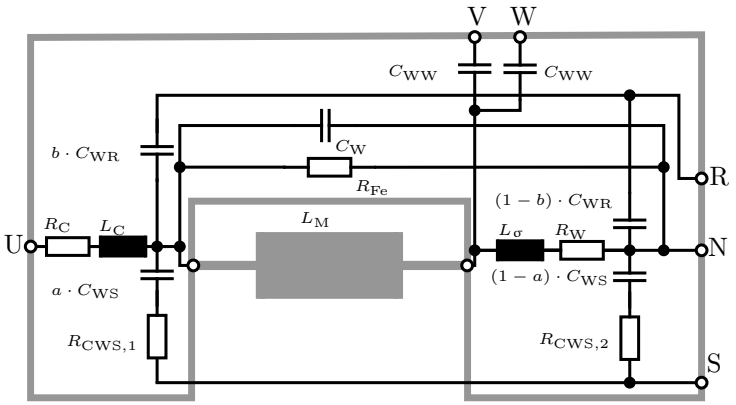

Figure 2.10: Phase winding equivalent circuit

that the placement of the series resistance of the parasitic capacitance has great influence on the frequency range in which the model is valid. An asymmetrical phase model in combination with a purely capacitive model of the rotor is used in [29]. In [31], the phase impedance is split into a main inductance and a stray inductance. In [11], the stray inductance from [31] is split into two parts in order to create a symmetrical model, allowing flexible reconfiguration. In addition, this work considers the phase coupling as well. Similar to [31], this is done to account for differences in the CM and differential-mode (DM) inductances.

Figure 2.10 shows the phase winding equivalent circuit in more detail. The elements of the phase winding circuit model are placed in a way that their location resembles the physical design of the machine to allow a comprehensible parameterization. L_C and R_C model the internal cabling of the machine from the connection box to the phase windings. C_{WS} is the coupling capacitance from winding to stator and C_{WR} is the coupling capacitance from winding to rotor. They are split into two parts using the factors a and b, respectively. The capacitance can be distributed unevenly between both ends, e.g. in the case of a random wound machine. When, for example, the beginning of the phase winding is located closer to the stator and the end is located closer to the rotor, a larger part of C_{WR} is shifted to the right capacitance closer to the star point. Section 2.2.9 shows that above 100 kHz, the impedance of the machine is dominated by $a \cdot C_{WS}$, L_C and R_C, meaning that the phase inductances block high-frequency currents.

An additional resistance R_{CWS} is introduced in series with $a \cdot C_{WS}$ in order to dampen the highest resonance of the machine without introducing more resistive elements in the main current path. In contrast to [31], the second resistance towards the stator is neglected, since it only influences the behavior at lower frequencies, where the CM impedance is high. C_{WW} models the capacitive coupling between the phases, while C_W models inter-winding capacitances. L_M and L_σ are the main and stray inductances. L_M is an N_{ph}-by-N_{ph} inductance matrix, which includes the inductive coupling between the phases. R_W represents the resistance of the winding. The iron losses, which strongly dampen the first resonance of the machine, are represented by R_{Fe}.

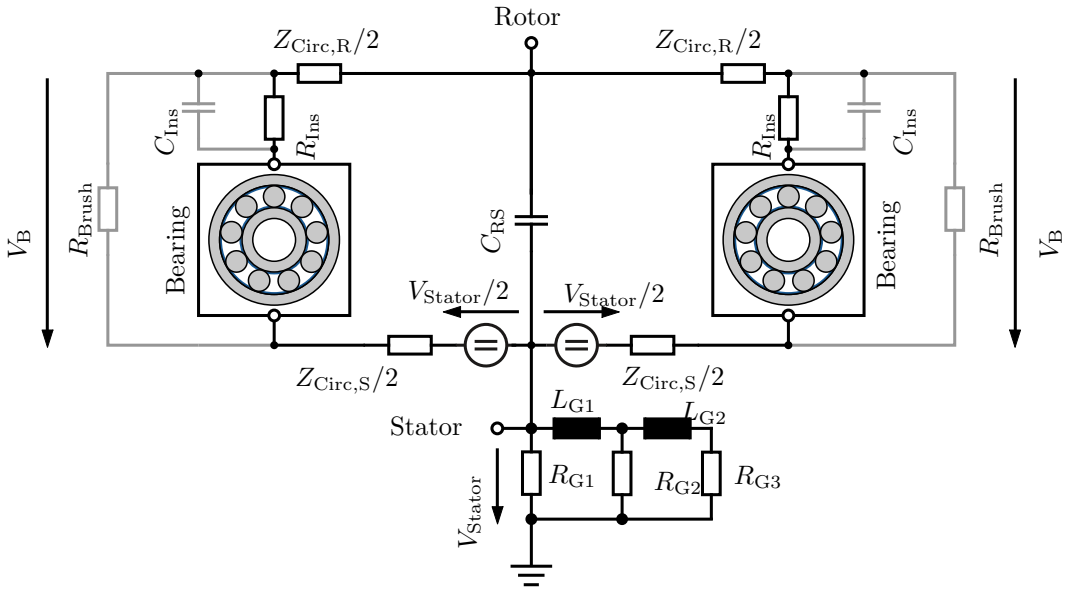

Figure 2.11: Rotor and stator equivalent circuit model with external countermeasures

2.2.4 Stator and Rotor Model

Figure 2.11 shows the rotor and stator equivalent circuit. The rotor and stator impedances $Z_{\mathrm{Circ,R}}$ and $Z_{\mathrm{Circ,S}}$ are used to model the current path for the inductive bearing current, while the two voltage sources $V_{\mathrm{Stator}}/2$ model the end-to-end shaft voltage that is induced by the CM current. The end-to-end shaft voltage is the driving force behind the inductive bearing current [6]. The voltage-controlled voltage sources $v_{\mathrm{Stator}}/2$ emulate a parasitic transformer between the CM current path and the inductive bearing current path [12]. C_{RS} is the capacitance between rotor and stator. The bearing model is covered in the next section. The ladder circuit, which consists of L_{G1}, L_{G2}, R_{G1}, R_{G2}, and R_{G3}, models the path that the CM current takes through the machine [11]. In the following, this impedance is referred to as Z_{Ladder}.

The gray elements in Figure 2.11 are used to model the different bearing current countermeasures which are investigated in this work. The combination of R_{Ins} and C_{Ins} can be used to model an additional insulation layer outside the bearing, as in [32]. This reduces the voltage applied to the bearing and the current flowing through it. R_{Brush} is used to model a carbon shaft grounding brush that directly connects the stator and the machine shaft. This brush reduces the impedance between rotor and stator and effectively short-circuits the bearing capacitance [33]. Instead of a carbon brush, a ring with carbon fibers, which contact the shaft can be used as well [34]. Since these countermeasures are applied outside the bearing, they are called *external bearing current countermeasures* in this work. Further *internal countermeasures*, i.e., bearing current countermeasures that are applied directly within the bearing, can be realized in the bearing model (cf. section 2.2.5). Other external bearing current countermeasures, which are not covered in

this work, include conductive slot wedges [35], a comb-like coil inserted into the stator slots [36] or electrostatic shielding on the rotor side [37].

2.2.5 Bearing Model

The electrical behavior of rolling element bearings can be modeled in different ways. As presented in section 2.1.2, at standstill and at low speeds, a bearing is conductive, since the inner and outer raceways of the bearing are in direct contact with the rolling elements. Its electrical behavior is purely resistive in this area. The bearing resistance consists of the contact resistance between the rolling elements and the raceways as well as the resistance of the rolling elements and the raceways themselves.

When speed is increased, a lubricant film between the bearing balls and the raceways forms. Its thickness depends on temperature, rolling element speed, and radial load of the bearing. The bearing now behaves like a capacitor, where the capacitance is defined by the lubricant film thickness d_{film} and the Hertzian contact area A_{Hertz}. In [38], a universal per-ball equivalent circuit model of a bearing is presented and a reduced model, i.e., lumped model, is derived.

2.2.5.1 Lumped Model

Lumped bearing models are used in many publications. In contrast to the model presented in [38], in most publications, (such as [23], [24], [39]), the bearing is modeled as a capacitance with a series resistance. Some publications go even further and model the bearing as purely capacitive [11], [40]. Other publications [6], [41], [42] replace the parallel variable resistance from [38] with a combination of a switch and a resistor.

When looking at the different operating areas of a bearing, different modeling approaches are applicable. At standstill and at low speed, the bearing is modeled as a purely resistive. This resistor includes the resistance of the inner and outer raceway, of the bearing balls and the contact resistance between the metal and the lubricant. At higher speeds, a series capacitance is added. The capacitance value depends on the speed and the temperature of the bearing, as well as on the properties of the lubricant. It is usually calculated from the Hertzian contact area A_{Hertz}, the lubricant film thickness d_{film} and the dielectric properties of the lubricant ϵ:

$$C_{\text{B}} = \frac{A_{\text{Hertz}} \cdot \epsilon}{d_{\text{film}}} \cdot X \tag{2.11}$$

Additionally, a factor X is introduced, which aims to include the stray capacitances outside of the primary contact area. This factor varies according to [6], [22], [41] and is sometimes integrated into ϵ [24]. This factor's variation indicates that there is a certain portion of the bearing capacitance that cannot be expressed with (2.11).

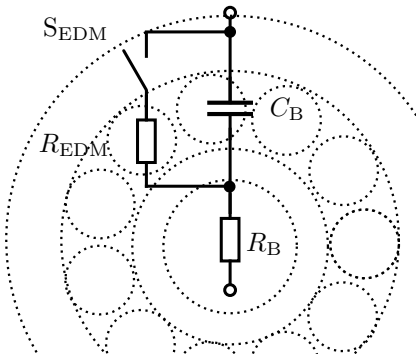

Figure 2.12: Lumped bearing model

2.2.5.2 Spatially Distributed Model

While the external electrical behavior of a rolling element bearing can be modeled with the aforementioned lumped models, they give no indication on the processes happening inside the bearing. Conversely, a spatially distributed model can help understand the electrical processes inside a bearing, such as the flow of parasitic currents and the current distribution during a breakdown. The per-ball model presented in [24], [38], [39] is adapted in order to model the current flowing in tangential direction, in addition to the radial current flow in the bearing. The resulting spatially distributed model of a rolling element bearing with nine bearing balls is shown in Figure 2.13. The model is split into nine slices, each containing one rolling element and a corresponding part of the inner and outer raceway of the bearing. It is assumed that the bearing cage plays a minimal role in the electrical behavior of the bearing. When the cage is made of a non-conductive material, it only influences the raceway-to-raceway capacitance by increasing the average dielectric constant in the region between the raceways. When it is made of a conductive material, two cases can occur: The cage either has direct contact with the bearing balls, i.e., an ohmic connection is added between adjacent bearing balls; or a lubricant film forms between the bearing balls and the cage, i.e., an additional capacitive connection between adjacent bearing balls is formed. Since the bearing balls are nearly on the same voltage level, the connection through the cage is neglected and the additional capacitance is added to the other capacitances in the bearing to compensate for its effect.

The resistive parts of the model are assumed to be constant with a slight change over temperature, which is neglected in this work. In the case of the resistances of the inner raceways outer raceway and bearing balls, this is because of the relatively low thermal coefficient of the resistance of $0.000\,94\,{}^{1}/_{\mathrm{K}}$. In the case of the breakdown resistance, this is due to a lack of reliable data of controlled breakdowns at different bearing temperatures under constant film thickness. The values for the breakdown resistance have been supplied by an external partner and are based on experimental investigations.

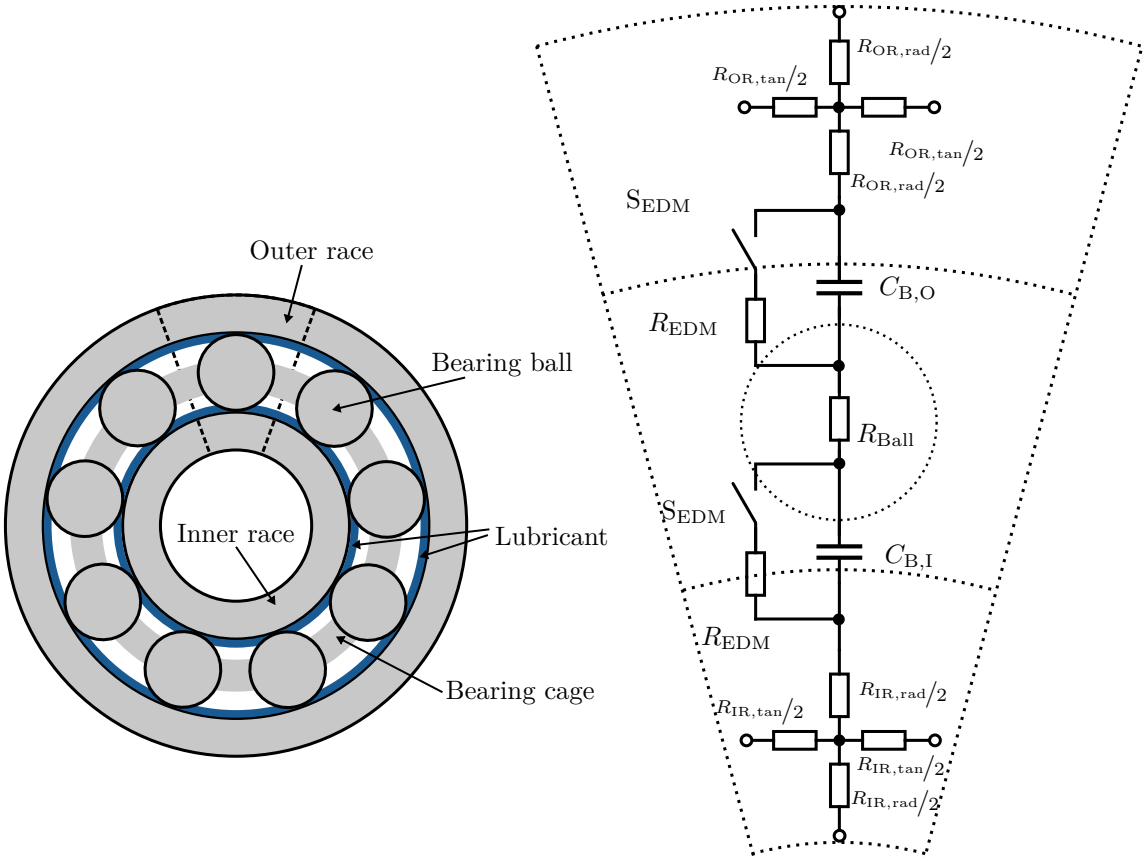

Figure 2.13: Distributed bearing model

The capacitances between the rolling elements and the inner and outer raceways, however, not only depend on the temperature, but also on the rotational speed and on the radial force on the bearing. Since the radial force, in contrast to speed and temperature, is not uniformly distributed around the circumference of the bearing, the capacitance must also change depending on the position of the rolling element. Assuming that the main force component is the gravitational force on the rotor, the capacitance will be greatest for rolling elements at the bottom of the bearing and lower for rolling elements at the top of the bearing. A more detailed investigation of this effect is given in section 2.2.8.

Note that in this work, a radially loaded bearing is investigated. When using an electric machine of which the axis is oriented in the vertical direction, the bearing will be loaded primarily in the axial direction, which leads to a uniform contact pressure distribution among the bearing balls and therefore also a uniform capacitance distribution within the bearing.

2.2.5.3 Internal Bearing Current Countermeasures

Apart from the external bearing current countermeasures introduced in section 2.2.4, additional measures can be taken inside the bearing itself. Similar to adding an additional insulation layer outside the bearing, the insulation voltage of the bearing can be increased by using a hybrid bearing with steel raceways and ceramic balls, or a full ceramic bearing. These types of bearings, however, come with their own disadvantages, such as a lower load capacity, a higher susceptibility to thermal shocks, and an increased cost. The distributed model cannot be applied to a hybrid or ceramic bearing, since the bearing balls are not conductive. The bearing capacitance is determined by the capacitance between the inner and outer bearing raceways, in the case of a hybrid bearing, and by the increase of the rotor-to-stator capacitance from introducing a dielectric, i.e., ceramic, in the case of a ceramic bearing. A sketch of a hybrid bearing and the resulting equivalent circuit model is shown in Figure 2.14.

Finally, similar to adding a shaft grounding brush outside the bearing, conductive grease can be used inside the bearing. This serves the same purpose of reducing the impedance between the rotor and the stator and thus short-circuiting the bearing capacitance. The impact of a shaft grounding brush on the bearing voltage and currents is investigated in section 4.5.

When the bearing breakdown behavior shall be modeled more precisely, the switch and the resistor can for example be replaced with two antiparallel thyristors, as shown in Figure 2.15. The conduction behavior of the thyristors has to be parameterized accordingly. The thyristors have to be triggered by a comparator when the breakdown voltage is exceeded. Furthermore, the electrical model can be coupled with a thermal model of the bearing to include temperature dependencies.

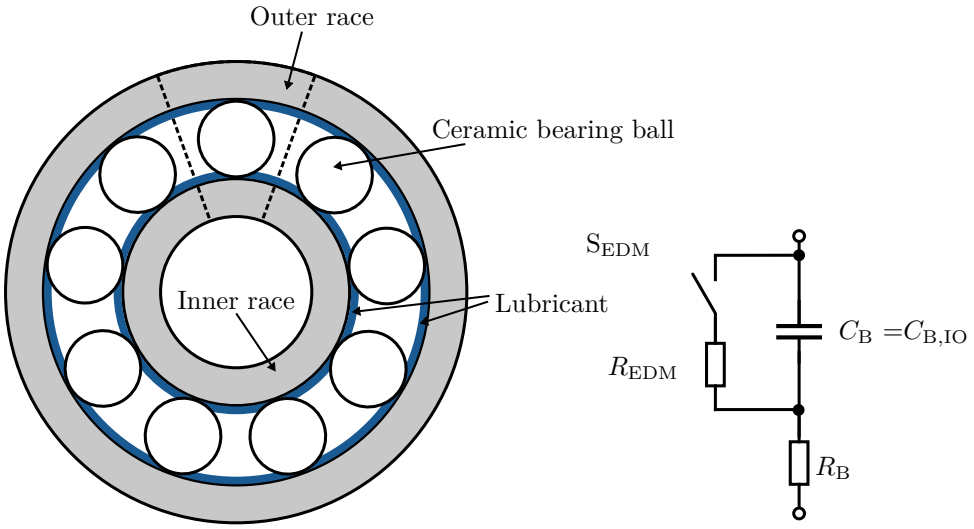

Figure 2.14: Hybrid bearing and resulting lumped bearing model

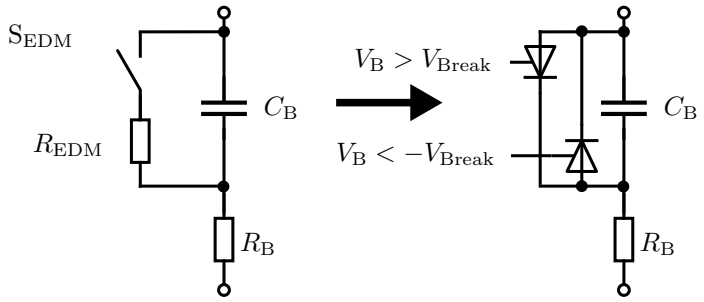

Figure 2.15: Thyristor-based breakdown model

2.2.6 Sensitivity Analysis

After introducing all parts of the model, in this section, a sensitivity analysis of the model parameters is conducted. The initial parameters are extracted manually from the first set of impedance measurements. To determine which parameter influences which part of the model, each parameter is varied from 50 % to 200 %. The relative deviation in the magnitude of all the following is calculated for each parameter: the CM impedance, the phase-to-phase impedance and the phase-to-star-point impedance, and the phase-to-shaft transmission ratio. The correlation coefficient between the relative deviation of the aforementioned impedances and transmission ratio, and the relative parameter change is calculated, and normalized, as a function of each parameter, while keeping the rest of the parameters constant. The impedance or transmission ratio that is influenced the most by a given parameter should thus have a normalized correlation coefficient of one. Consequently, this is the modeling methodology from which the given parameter can be extracted.

An exception is made for the cable parameters. Since the motor cable can be removed and characterized separately, its parameters are extracted from this additional measurement. The parameter extraction is done manually due to the low number of parameters related to the cable. The parameters are still included in the sensitivity analysis to show where its parameters should be extracted in the case the cable cannot be removed from the machine.

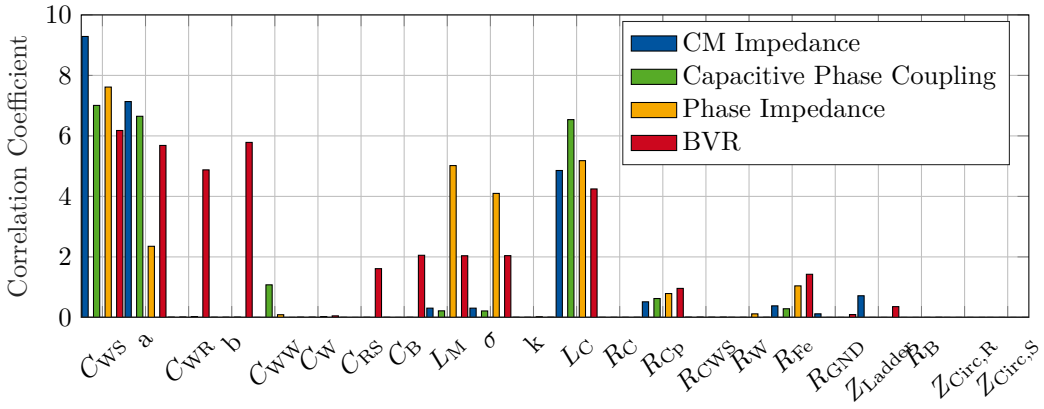

Figure 2.16: Influence of the model parameters on the emulated impedance and transmission ratio measurements

Figure 2.16 shows the results of the sensitivity analysis. The correlation coefficients of the parameter change and the resulting relative rms change in impedance or transmission ratio are shown on the y-axis. Each color indicates each of the different measurements described in section 2.2.7 that are emulated in the model. It can be observed that C_{WS} and a influence the CM impedance the most. Thus, the CM impedance measurement is used to estimate these parameters. C_{WW} and L_{C} are extracted from the measurement of the capacitive phase coupling, as their influence is largest there. L_{M}, σ, and k are extracted from the phase impedance measurement. As already suggested by equation (2.8), C_{WR},b, C_{RS}, C_{B} greatly influence the BVR measurement. Additionally, R_{Fe} is extracted from this measurement. R_{B}, $Z_{\mathrm{Circ,R}}$ and $Z_{\mathrm{Circ,S}}$ have nearly no influence on any of the measurements conducted with the vector network analyzer (VNA). Thus, they have to be extracted from time domain measurements of the bearing current.

2.2.7 Machine Impedance and Transmission Ratio Measurement

In this section, the measurements that have to be conducted for the parameterization of the developed model are shown. The device under test (DUT) is a 400 V, 5.5 kW industrial standard induction machine. Impedance measurements and transmission ratio measurements are conducted with a Bode100 VNA. The machine is insulated from ground and at standstill. The bearings are removed and replaced with plastic spacers to eliminate the influence of the bearing capacitance. The bearing capacitance varies with the rotational

speed and the temperature of the machine. In addition, at standstill and at low speed, the bearing acts as a short-circuit. Therefore, it is not possible to measure the rotor-to-stator capacitance C_{RS} under these conditions. The bearing capacitance is measured separately in a specially designed test bench and added to the model after the final parameterization (c.f. section 2.2.8).

First, the CM impedance of the machine is measured by connecting all three phase terminals to the output of the VNA and the stator ground connection of the machine to the ground of the VNA. The measurement setup is shown in Figure 2.17.

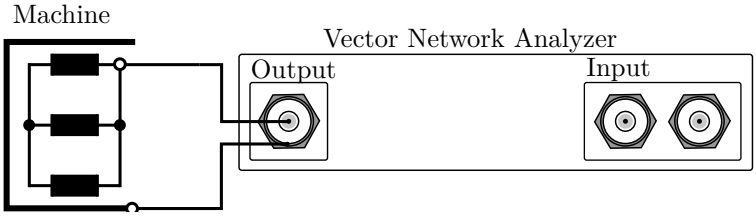

Figure 2.17: VNA setup for the CM impedance measurement, the input is connected internally

Next, the bearing voltage ratio measurement is conducted. The setup is shown in Figure 2.18. The output of the VNA is again connected to all three phase terminals and the ground node is connected to the stator. Then, using a carbon brush, the input of the VNA is connected to the machine shaft and the reference potential of the input is connected to the stator. This allows to measure the bearing voltage ratio. Note that the bearing was replaced by a plastic spacer, so the measurement does not provide the exact BVR. However, it is still required in order to parameterize the model.

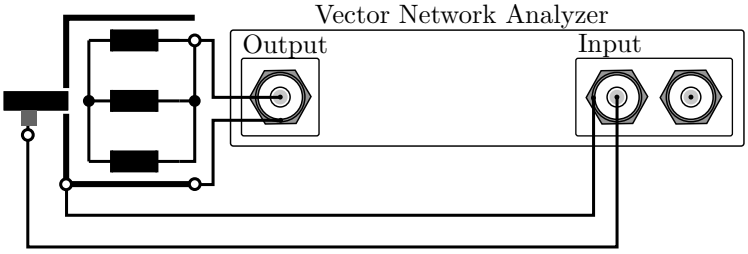

Figure 2.18: VNA setup for the BVR measurement

Third, the phase impedance measurements are conducted. The star-point connection is removed so that the phases can be measured separately. The VNA output terminals are then connected to each end of one of the phases, as shown in Figure 2.19. The measurements are carried out for each of the phases, these three measurements are shown in the appendix in Figure A.1. Phase V appears to have approximately 5 % greater inductance than the two other phases, which can indicate that one of the coils of this phase has an additional winding. The measurements are still similar enough so that only one measurement is used for parameterization and the differences between the phases are neglected in the model.

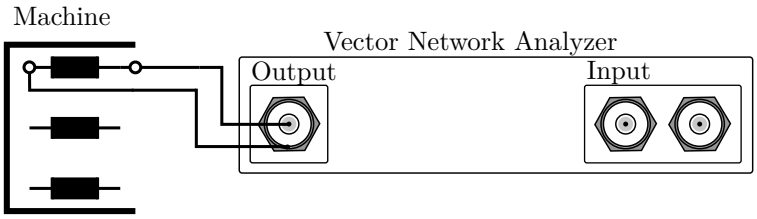

Figure 2.19: VNA setup for the phase impedance measurement, the input is connected internally

Finally, the capacitive coupling between the phases is measured by using the setup shown in Figure 2.20. The star-point connection is removed and the output of the VNA is connected to both ends of one phase while its ground is connected to both ends of another phase. Similar to the phase impedance measurements, these measurements are conducted for the coupling between the three phases and are similar enough to each other,so as to use the same measurement for all three phase coupling capacitances. The three measurements are shown in Figure A.2.

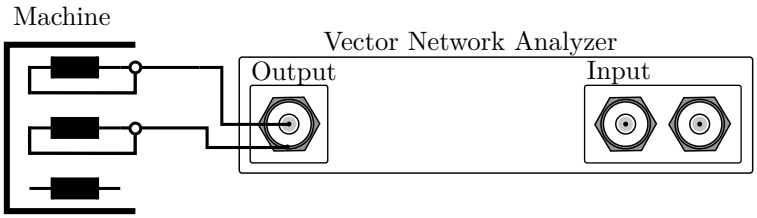

Figure 2.20: VNA setup for the measurement of the capacitive phase coupling, the input is connected internally

2.2.8 Bearing Capacitance Measurement

Since the bearings were removed for the measurements in the previous section and replaced with plastic spacers, the bearing capacitance cannot be extracted from these impedance measurements. Thus, additional measurements are required to parameterize the models presented in section 2.2.5. Parts of this section have been investigated as a part of this work and were published in [43].

These measurements are conducted on a radial load test bench depicted in Figure 2.21. The test bench includes three bearings: one load bearing and two test bearings. The load bearing applies the radial load, which is set via a spring in the radial load unit, to the test bearings. The radial load test bench has to be modified to enable the bearing capacitance measurement of one of the test bearings by minimizing the influence of all other parasitic capacitances in the test bench. Thus, the load bearing and one of the test bearings are replaced by ceramic bearings. Since the distributed bearing model presented in section 2.2.5 requires single ball-to-raceway capacitances, the bearing under test is also modified. Here, a special hybrid bearing is used, in which one bearing ball and the

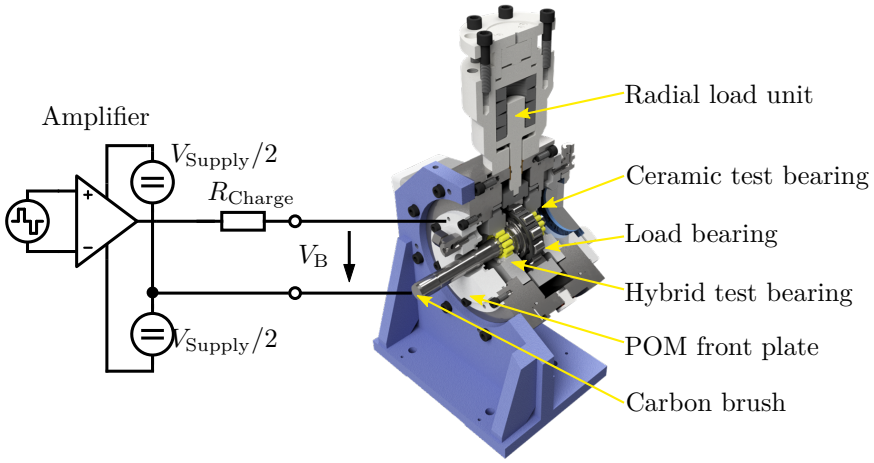

Figure 2.21: Radial load test bench for bearing capacitance measurements

raceways are made of steel whereas the remaining bearing balls are made of ceramic, as displayed in Figure 2.22. Thus, the sum of both ball-to-raceways capacitances of one bearing ball plus the raceway-to-raceway capacitance can be measured as a function of the position of the bearing ball. When using a normal steel bearing, only the lumped bearing capacitance can be measured. The front plate of the test bench, which is usually made of steel, is replaced with a plate made of polyoxymethylene (POM) and a connection to the outer ring of the bearing is made. To connect the inner ring, a carbon brush is placed on the shaft. Since the other two bearings on the shaft are ceramic bearings and the shaft is driven by a belt drive, the bearing under test is assumed to be fully insulated from ground with minimal parasitic capacitance. Note that the bearing capacitance is tested under pure radial load. However, in electric machines, there will also be some constant axial load since the bearings are spring-loaded to ensure that the minimum required load is always applied.

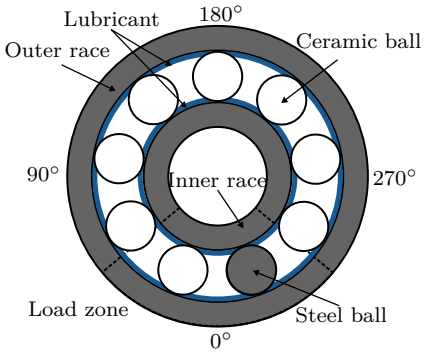

Figure 2.22: Hybrid bearing with one steel ball for single ball-to-raceways capacitance measurements

The bearing capacitance has to be measured while the shaft rotates at a speed of up to 6000 rpm. In order to achieve a sufficiently large angular resolution of less than 1°, the impedance has to be measured within 50 µs. Thus, conducting a full impedance sweep, e.g.

with an impedance analyzer, is not an option. There are different measurement methods that are suitable for bearing capacitance measurements. In [24], a sinusoidal voltage from a signal generator is applied to the bearing via a high precision resistor, and the phase shift and amplitude reduction of the bearing voltage is measured. Thus, the bearing capacitance and resistance can be extracted. In [23], a rectangular waveform is used to charge the bearing capacitance. In this thesis, the method from [23] is implemented with small adaptations. A bipolar voltage of $\pm 5\,\mathrm{V}$ is applied to the bearing and the parallel resistance from [23] is omitted The hybrid test bearing is charged and discharged via a resistor R_{charge} of $10\,\mathrm{k\Omega}$. From the rise and fall times of the bearing voltage, the time constant of the charging process can be calculated and thus the capacitance value. When eliminating most of the other capacitances from the test bench by design, as described in the beginning of this section, and the rest (such as the raceway-to-raceway capacitance $C_{\mathrm{B,IO}}$) by proper calibration, the sum of the capacitances $C_{\mathrm{B,I}}$ and $C_{\mathrm{B,O}}$ of the steel ball in the bearing can be measured.

The maximum temporal resolution depends on the longest expected charging time. A switching and sampling frequency of 20 kHz is chosen. Thus, at 6000 rpm, an angular resolution of 0.7° could be achieved. For lower speeds, the angular resolution is naturally finer. It is worth pointing out that while the absolute angular position of the bearing ball is unknown, its relative angular position can be calculated from the speed. When the bearing capacitance is properly charged and discharged via the charging resistor R_{Charge}, a continuous capacitance waveform is produced. When the bearing is, however, discharged via a breakdown or from contact between the raceways and the steel bearing ball, much faster fall times are measured, which can be falsely interpreted as very high capacitance values.

The bearing capacitance measurements are conducted at four different speeds, 1000 rpm, 3000 rpm and 6000 rpm; at four different temperatures 20 °C, 30 °C, 50 °C and 80 °C; and with three different lubricants, automatic transmission fluid (ATF), polyalphaolefin (PAO) and grease.

First, the bearing capacitance of a hybrid bearing, i.e., a bearing with steel raceways and ceramic balls, is measured. The measured capacitance value corresponds to the capacitance between the inner and outer raceways $C_{\mathrm{B,IO}}$. Its value varies with the rotational speed, the bearing temperature and the utilized lubricant. The measurement results can be found in the appendix in Figure A.3, Figure A.4 and Figure A.5. They are used as calibration values for the single-ball bearing capacitance measurements. These measurements could only be conducted with ATF and PAO, since these lubricants were pumped through the bearing during the measurements. The grease lubricated bearing was fully closed during the measurements. Since no hybrid bearing with the same grease was available, the calibration could not be conducted. This means that the single-ball bearing capacitance measurement for grease accounts for $C_{\mathrm{B,I}} + C_{\mathrm{B,O}} + C_{\mathrm{B,IO}}$ instead of $C_{\mathrm{B,I}} + C_{\mathrm{B,O}}$.

Figure 2.23 shows a single-ball bearing capacitance measurement at 1000 rpm. The utilized lubricant is ATF. Outside the load zone, the capacitance is constant with respect

to the angular position and only slightly varies with temperature. Within the load zone, i.e., approximately between −75° and 75°, the change in the lubricant film thickness and thus in the bearing capacitance can be clearly observed. At 20 °C, the capacitance increases from 22 pF to 39 pF. The spikes in the capacitance waveform correspond to faster discharges of the bearing capacitance, either because of contact between the raceways and the bearing ball or because of breakdowns of the insulating lubricant film. At 30 °C, the decreased viscosity leads to a reduced lubricant film thickness and thus an increased bearing capacitance peak of 49 pF in the middle of the load zone (0°). The number of breakdowns also significantly increases. At 50 °C and 80 °C, the lubricant film thickness in the load zone is so low that the bearing capacitance cannot be fully charged anymore. The lubricant film either immediately breaks down because it cannot block the voltage or the capacitance is quickly discharged due to the increased probability of contact between the bearing ball and the raceways.

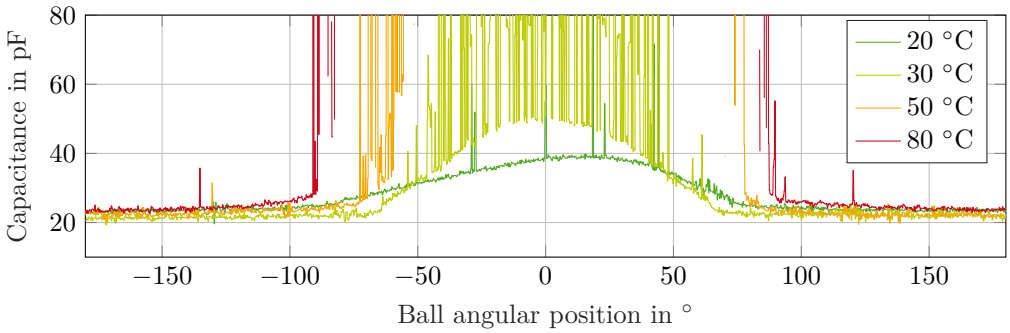

Figure 2.23: Parasitic capacitance of an ATF lubricated single bearing ball at 1000 rpm

Next, the influence of the rotational speed on the bearing capacitance is investigated. Figure 2.24 shows the same type of measurement at 6000 rpm. The higher speed of the bearing leads to a higher lubricant film thickness. Outside the load zone, this has nearly no influence. At 0°, the bearing capacitance peak values result lower than the values at 1000 rpm (Figure 2.23). At 20 °C, a peak value of 33 pF is reached. At 30 °C, it increases to 35 pF. Even at 50 °C, the bearing capacitance is reliably charged to the full ±5 V. At 80 °C, the lubricant film thickness is again so thin that the lubricant film breaks down before the capacitance is fully charged.

In a next step, the influence of different lubricants is investigated. Figure 2.25, shows the same layout of results when PAO is used as a lubricant at a speed of 1000 rpm. PAO has a much higher viscosity than ATF and should thus lead to higher lubricant film thickness. Despite the thicker lubricant layer, the higher electrical permittivity of PAO causes a higher peak bearing capacitance with respect to ATF. Outside the load zone, the difference is less noticeable because there, the air and the ceramic balls of the bearing have a great influence on the parasitic capacitance. Within the load zone, the peak capacitance value is, however, mainly determined by the lubricant film thickness and the dielectric properties of the lubricant. At 20 °C, the bearing capacitance increases to up to 64 pF. At 30 °C, it goes up to 80 pF and at 50 °C, it even exceeds 100 pF. These increased capacitance values stem from a combination of a greater dielectric constant and

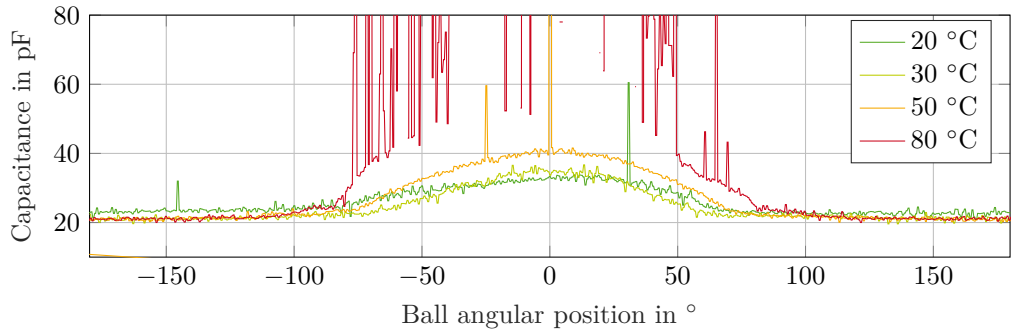

Figure 2.24: Parasitic capacitance of an ATF lubricated single bearing ball at 6000 rpm

a greater breakdown field strength. At 80 °C, the lubricant film breaks down again within the load zone, and thus no capacitance value can be extracted.

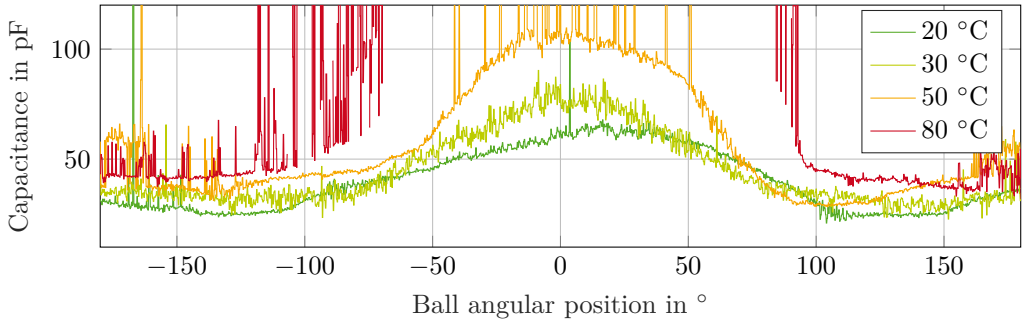

Figure 2.25: Parasitic capacitance of a PAO lubricated single bearing ball at 1000 rpm

Since many bearings are lubricated with grease, in a final step, a grease lubricated bearing is tested. Note that here, $C_{\mathrm{B,IO}}$ is included in the measurement, in addition to the sum of $C_{\mathrm{B,I}}$ and $C_{\mathrm{B,O}}$. The bearing capacitance is subject to larger fluctuations outside the load zone. Within the load zone, the typical increase in capacitance is visible. The lubricant film only behaves capacitively at 20 °C. Here, the capacitance increases from 55 pF to 73 pF. At higher temperatures, too many breakdowns occur within the load zone and the bearing capacitance values cannot be extracted.

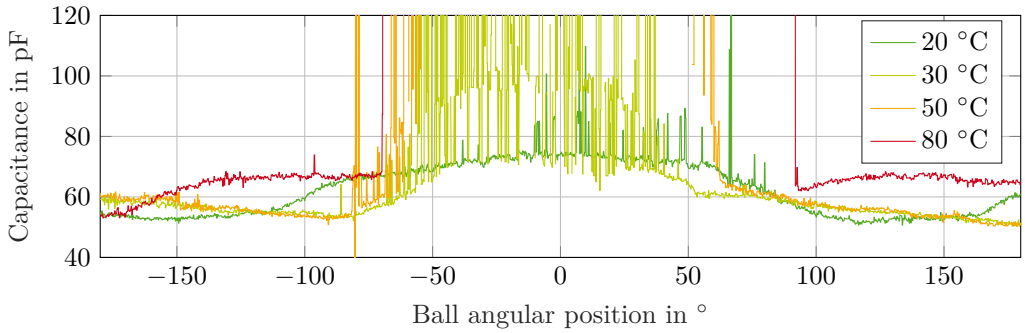

Figure 2.26: Parasitic capacitance of a grease lubricated single bearing ball at 1000 rpm

As already mentioned before, the spikes in the capacitance waveforms are due to breakdowns of the lubricant film because of the applied bearing voltage. In a breakdown, the voltage is discharged much more quickly during a breakdown event than it is during the bipolar switching over the relatively large charging resistor R_{Charge}. Therefore, the expected result would be a much lower rise or fall time and thus a much lower calculated capacitance value. Figure 2.27 shows why that is not the case. The rise time is calculated as the time that the voltage needs to go from 10 % to 90 %, so in this case from $\pm 4\,\mathrm{V}$ to $\mp 4\,\mathrm{V}$, given that the excitation voltage is $\pm 5\,\mathrm{V}$. When the bearing capacitance is large, the rise and fall times are long (c.f. $t_{\mathrm{Rise},1}$). When the bearing capacitance is small, the rise and fall times are short (c.f. $t_{\mathrm{Fall},1}$). However, when a breakdown occurs, the fall time starts before the actual switching event. Since the bearing voltage only drops to 0 V, the criterion for the end of the fall time is not met until the next switching event occurs. Therefore, $t_{\mathrm{Fall},1}$ appears much longer than the fall times of both the breakdown itself and the subsequent switching event.

The proportions between the switching frequency and the rise and fall times are not to scale in Figure 2.27. In reality, the rise and fall times are much shorter compared to the switching period. Figure 2.27 shows why, when a breakdown occurs, the detected fall time (in this case $t_{\mathrm{Fall},2}$) and thus the resulting calculated capacitance value is much larger than the actual bearing capacitance. This problem could be remedied by using a unipolar excitation waveform instead of a bipolar waveform. However, in this thesis, this is seen as an advantage, since the bipolar excitation allows to clearly distinguish between valid capacitance measurements and breakdown events. If the breakdown resistance is large, this distinction is not as clear when using unipolar excitation.

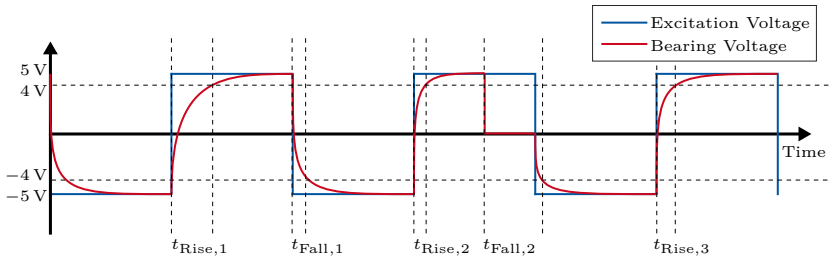

Figure 2.27: Illustration of capacitance measurement waveforms

The single bearing ball capacitance measurements conducted in this section are finally superposed to calculate the total bearing capacitance. For the bearing lubricated with ATF, the total capacitance varies between 261 pF and 336 pF. For the bearing lubricated with PAO, the capacitance varies between 468 pF and 711 pF. These capacitance ranges are valid for speeds between 300 rpm and 6000 rpm and for temperature between 20 °C and 80 °C. In many machines, this variation would not have a significant influence on the BVR, as already stated in [6], since C_{RS} is usually much larger than C_{B}. In the investigated machine, however, C_{RS} is only approximately ten times greater than C_{B}, depending on the operating point.

2.2.9 Model parameterization

In section 2.2.6, the different model parameters are assigned to four different types of measurements by analyzing which of these measurements they influence the most. This is used as a basis to decide, which parameter can be extracted from which of the measurements. Now, the parameterization of the model will be described. The four types of measurements from section 2.2.7 are replicated in the model.

Table 2.1: Nameplate parameters of the DUT

Nominal power	P_N	$= 5.5\,\mathrm{kW}$
Nominal current	I_N	$= 18.6\,\mathrm{A}$
Nominal voltage	U_N	$= 230\,\mathrm{V}$
Nominal speed	n_N	$= 1460\,\mathrm{rpm}$
Pole pairs	p	$= 2$

Starting with the CM impedance measurement, the parameters are adapted so that the measurement matches with the simulations. Figure 2.28 shows the results. After manually adjusting the parameters for a good fit between the simulation and the measurement, the parameterization is finalized by means of a particle swarm algorithm. To this end, a minimization of the relative root-mean-square deviation between the modeled and the measured impedance is conducted. It is important to use the relative deviation to achieve high accuracy even in low-impedance parts of the spectrum. After fine-tuning the model parameters with a particle swarm algorithm, the measurement and the simulation match well over the whole frequency range.The following parameters were extracted from this measurement: C_WS,a,R_CWS, and R_GND.

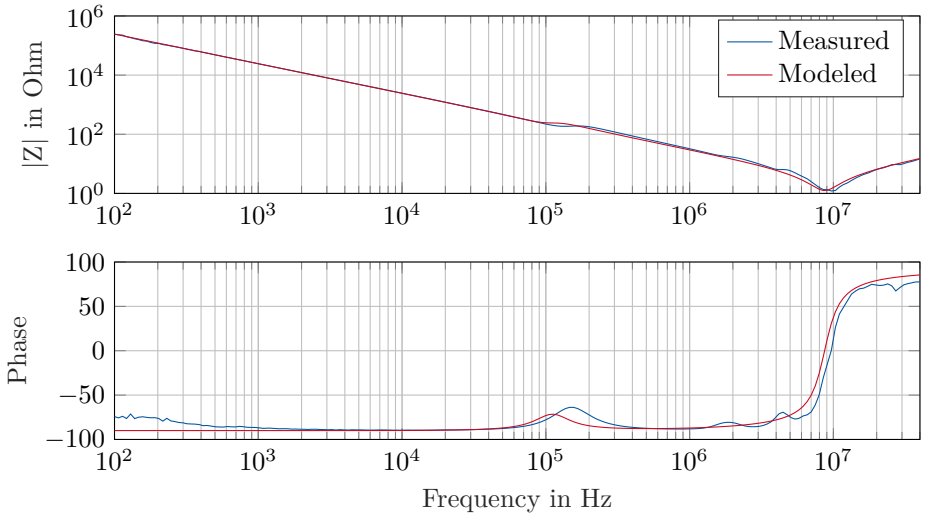

Figure 2.28: Modeled and measured CM impedance

Next, the phase impedance simulation is matched to the measurement. Figure 2.29 shows the results after the fine-tuning. This measurement was used to extract the following parameters: L_{M},L_{σ} andR_{Fe}. The measurement and the simulation match well for most of the spectrum, but some deviations occur in the higher frequency range. These deviations could not be eliminated by the particle swarm algorithm, and thus point to the fact that a higher order model of the windings might be necessary to model the high-frequency part of the impedance more accurately.

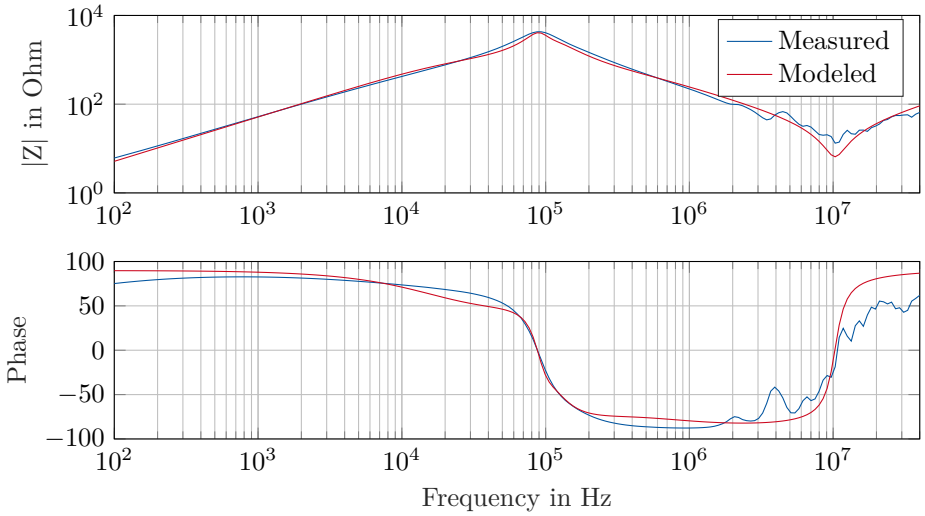

Figure 2.29: Modeled and measured phase impedance

Subsequently, the BVR measurement is compared to the simulation. Figure 2.30 shows the measured and modeled BVR. The differences in the shape of the impedance curves are uncanny. The measured shape could not be reproduced with any combination of parameters, which either means that the measurement setup shown in Figure 2.18 is inadequate for this type of measurement or that the model does not include some effects that are required to precisely replicate the BVR.

Since the BVR is dominated by C_{RS} and C_{WR}, these two parameters could not be extracted from the frequency domain measurements. The rotor-to-stator capacitance C_{RS} was therefore calculated according to the formulas presented in [44] and according to the formula for a cylindrical capacitor as

$$C_{\mathrm{RS}} = 2\pi l \cdot \ln\left(\frac{r_{\mathrm{stator}}}{r_{\mathrm{rotor}}}\right). \tag{2.12}$$

Here, r_{stator} is the inner radius of the stator, r_{rotor} is the outer radius of the rotor and l is the iron length. The two approaches lead to similar results with less than 1 % deviation.

To obtain the remaining model parameters, time domain simulations are conducted. The model is fed with waveforms that are calculated from the measured CM voltage in such a way that they result in the same CM voltage levels. Then, first, the CM voltage is ana-

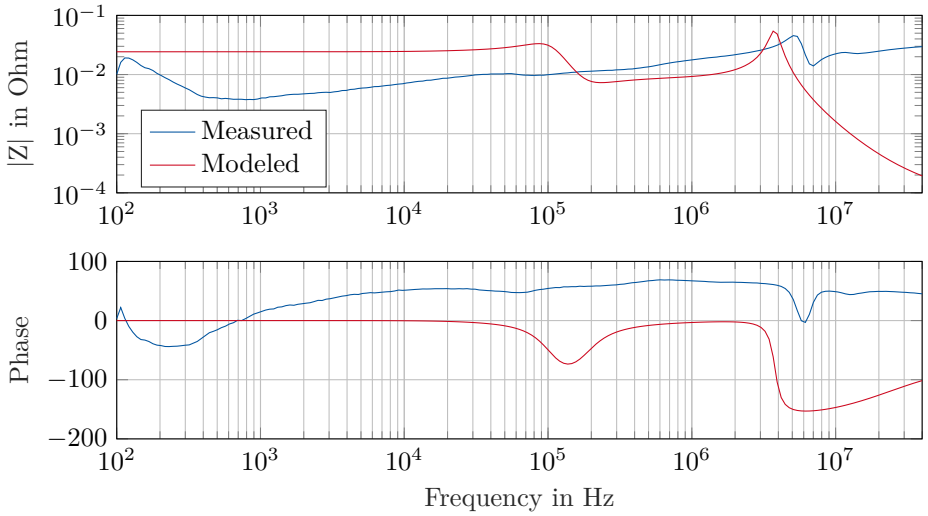

Figure 2.30: Modeled and measured BVR

lyzed. It is used to extract the model parameters for the motor cable, i.e., its inductance, its resistance and the coupling capacitance between the leads. Figure 2.31 shows that the waveforms match well. The amplitude, frequency and decay of the switching event are nearly identical after adapting the cable parameters.

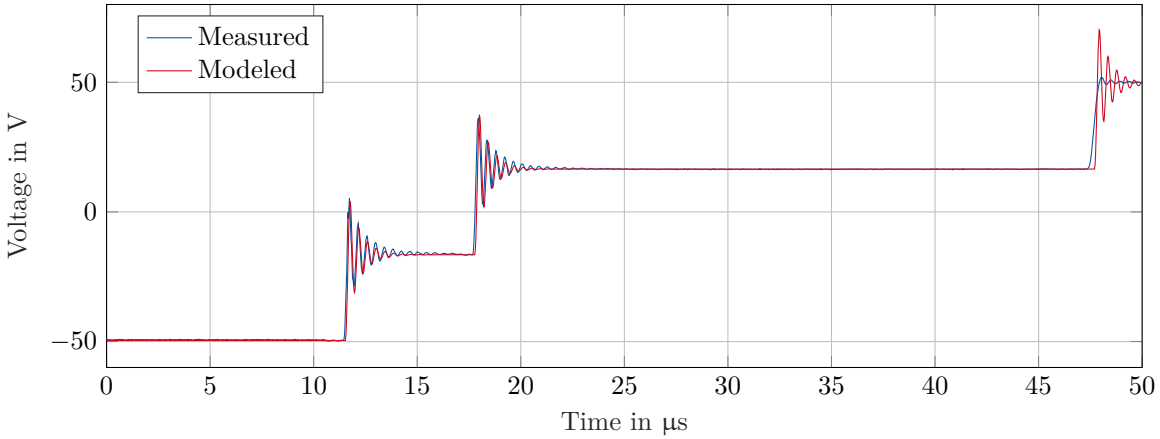

Figure 2.31: Modeled and measured CM voltage

Afterwards, the star point voltage v_{STP} is analyzed. Figure 2.32 shows the results. Again, after adjusting the necessary parameters, i.e., the winding-to-rotor capacitance C_{WR} and the main inductance L_{M}, the waveforms match well.

The internal model parameters that could not be measured separately were calculated analytically according to the approaches presented in the literature [6], [44].

After finalizing the model parameterization, the current distribution inside the bearing during an EDM event is analyzed. Figure 2.33 shows the simulation results. The current

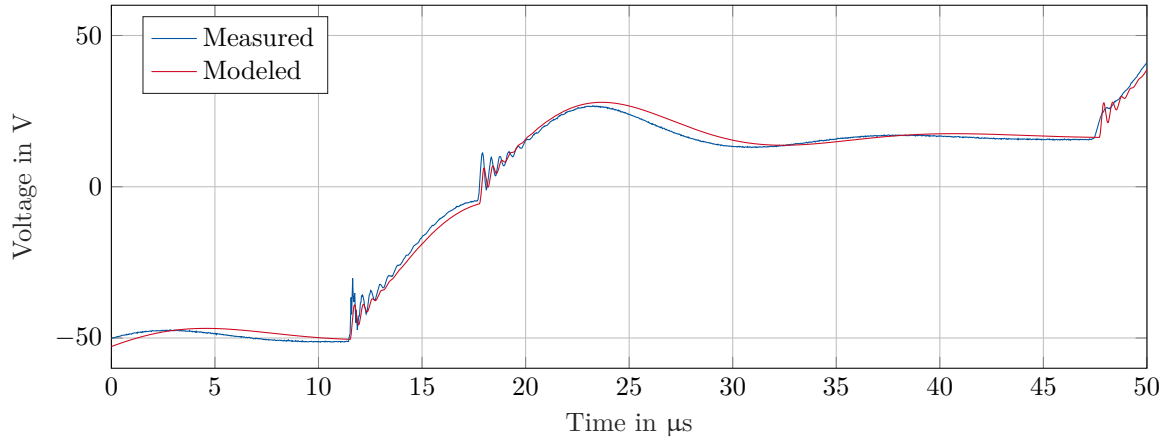

Figure 2.32: Modeled and measured star point voltage

inside the bearing from the lumped and the distributed model during a breakdown is plotted in Figure 2.33a. When the models are parameterized correctly, they give the same results. The current that flows inside the bearing ball, at which the breakdown occurs, is shown in Figure 2.33b. Note that the axis scaling is different to Figure 2.33a both in current amplitude and time. The model suggests that during an EDM event, a short current peak occurs with an amplitude that is much higher than the current measured from outside the bearing. This is because the distributed bearing capacitance is interconnected via low-impedance paths and the capacitances inside the bearing thus discharge into the breakdown very quickly.

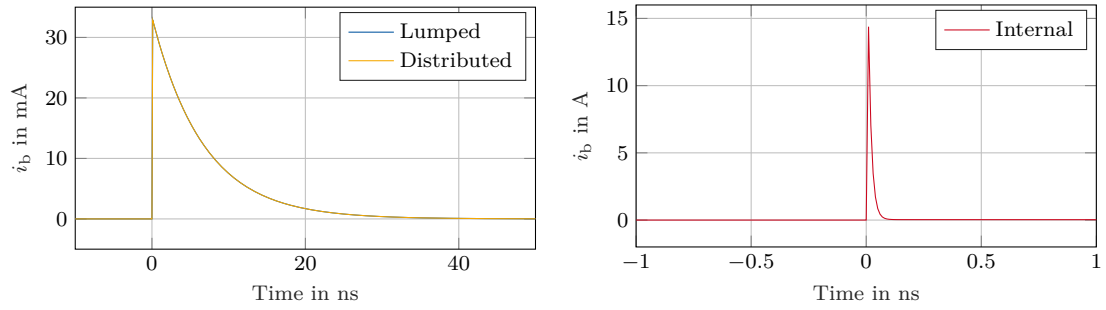

(a) Outside of the bearing

(b) Within the bearing

Figure 2.33: Simulated current flow outside and within the bearing during a EDM event

2.3 Measuring Parasitic Currents and Voltage

In the literature, many different measurement methods are used for measuring parasitic currents. For CM currents, there are mainly two measurement points available. They can either be measured in the motor cable between inverter and machine, or in the return path, e.g.,the ground connection between machine and inverter or the motor cable shield. In [45], a CM current prediction is verified by measuring the return path current. Which measurement method is applicable strongly depends on the configuration of the machine and the inverter, whether the motor cable is shielded, and how closely the inverter and the machine are integrated.

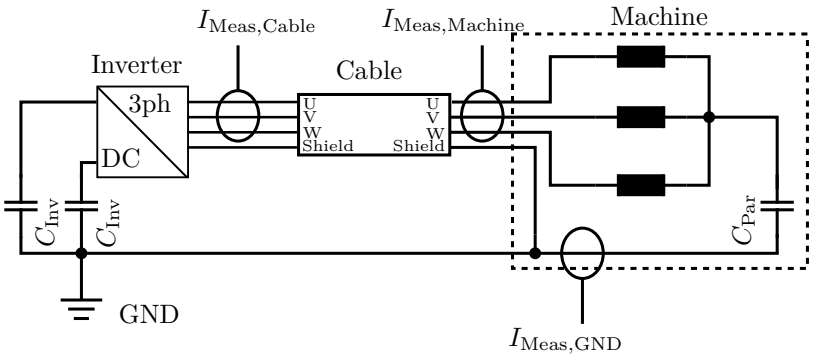

Figure 2.34: Measurement points for CM current

A standard configuration of an inverter and an electric machine connected via a shielded cable is shown in Figure 2.34. $I_{\text{Meas,Cable}}$ represents the full CM current flowing into the machine and the current charging the parasitic capacitances of the motor cable. When moving the measurement point to the machine side of the cable, most of the cable charging currents bypass the measurement and only the CM current flowing into the machine is measured. For both of these measurement points, it is important only to measure the current through the motor cables connected to the phases of the machine and to leave the shielding or possible connections to the star point out of the measurement.

There are two ways to achieve this. The first method is to measure each of the phase currents and add them up. Although this sum is usually assumed to be zero, a value different than zero corresponds to the CM current. The advantage of this method is that it does not require additional sensors, since the phase currents are usually measured at the inverter terminals, because their instant values are required for the control. The sensors in the inverter are designed to be accurate enough for control, but when the phase currents are added, the error of each phase current sensor is also added up, leading either to a low measurement accuracy of the CM current or to a much higher accuracy requirement for the sensors than what is usual. Additionally, the phase current sensors can only measure $I_{\text{Meas,Cable}}$. When the goal is to measure the CM current into the machine, this is another error source, since the current $I_{\text{Meas,Cable}}$ includes the charging currents of the

cable capacitance. In $I_{\text{Meas,Machine}}$, these charging currents are not measured. Also, the measurement points $I_{\text{Meas,Cable}}$ and $I_{\text{Meas,Machine}}$ are subject to high-frequency CM voltages, which can cause disturbances in the current measurement. Finally, the phase current sensors are usually not designed for measuring high-frequency currents and the sensor signals are usually low-pass filtered, since the high-frequency CM current components are not needed for the control and are thus treated as disturbances.

For the second method, instead of adding up the phase currents, an additional CM current sensor can be used to measure the CM current. In a laboratory setting, Rogowski coils are often used for this purpose. A comparison of Rogowski coils and Pearson probes in [46] shows that Rogowski coils are better suited for CM current measurement. But a CM current sensor could also be integrated into the inverter or into the machine. This has the advantage that the CM current sensor can be designed independently from the phase current sensors, so that the CM current sensor is capable of capturing a greater range of amplitudes and frequencies of the CM currents. This way, the current can be measured at $I_{\text{Meas,GND}}$, which has several advantages. First, only the CM current flowing out of the machine is measured. Second, since the housing of the machine is usually connected to ground, no disturbances from CM voltages occur. And third, non-insulated measurement devices, such as shunt resistors, can be used, reducing the cost of the sensor. The disadvantage is that when the motor cable is shielded and the shield is connected to the machine, it is difficult to place the current sensor in a way that it only measures the CM current in the machine. When there is no defined ground path, for example when machine and inverter are both connected directly to the chassis, this type of measurement is not possible or requires adaptations in the mounting and ground connections of the drive. Additionally, in highly integrated e-axles, the inverter is directly connected to the machine phases and the return path is the housing of the e-axle, requiring a specialized solution for CM current measurement that is integrated into the housing.

In this work, the inverter is connected to ground via a grounding cable; which can be either connected to its DC-terminal, to the midpoint of the inverter, or to its housing; which means that the inverter is only connected to ground via its parasitic capacitances to the housing. Based on the findings of [47], the CM current is measured with a Rogowski coil. The foundations for the investigations in the following sections were published by the author in [48] within the scope of this thesis.

2.3.1 Bearing Current Measurement

In addition to the CM current, this work focuses on measuring the bearing current in the investigated electric machine. The literature shows mainly three different approaches for bearing current measurement.

The first and most widely used approach is to insulate either the bearing from the stator or the end shield of the machine from the main body of the stator, as shown in Figure 2.35

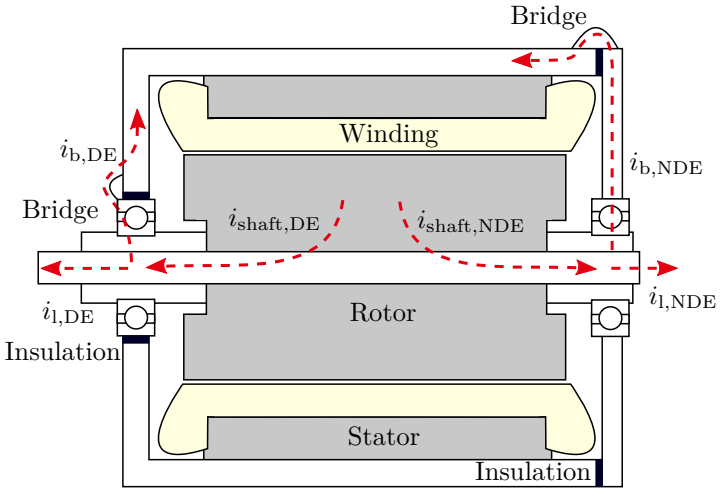

Figure 2.35: Machine axial cross-section with insulated bearing (left) and insulated end shield (right) and bridges for current measurement [48]

[40], [42], [49]–[52]. The insulation is then bridged with a wire or a shunt resistor and the current through the wire or shunt is measured. The advantage is that this approach is very simple and applicable to almost all machines. Adding a thin insulation layer usually does not require extensive mechanical changes and almost any current measurement device can be used. The disadvantage is that the parasitic current path for the bearing current changes, leading to a change in impedance. This also influences the current, leading to systemic measurement errors. Moreover, when using non-galvanically-insulated measurement devices, additional parasitic current paths might emerge. These currents can influence the measurement results and lead to errors.

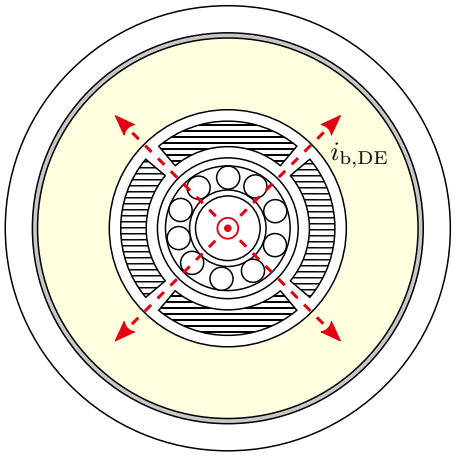

Figure 2.36: Machine end shield with bridges for bearing current measurement and bearing current paths [48]

The second approach is to remove most parts of the end shield of the machine, leaving only small bridges around which a Rogowski coil can be fitted, as shown in Figure 2.36 [18]. Since the bearing current has to flow through the end shield, the sum of the currents

through the bridges is equal to the bearing current. If the bridges are distributed evenly and are designed to be as wide as possible, the impact on the parasitic current path is much lower than when insulating the bearing or the end shield. However, this method comes with several disadvantages. First, it requires extensive mechanical changes to the end shield, which might inhibit its mechanical stability. These modifications might even be impossible when cooling channels are integrated into the end shield, or when a direct oil cooling is used for the end windings. Second, adding the current measurements from several Rogowski coils inherently leads to a greater measurement error than measuring the current with a single Rogowski coil. Furthermore, when overlaying ground currents drive the individual coils out of their measurement range, large measurement errors will occur.

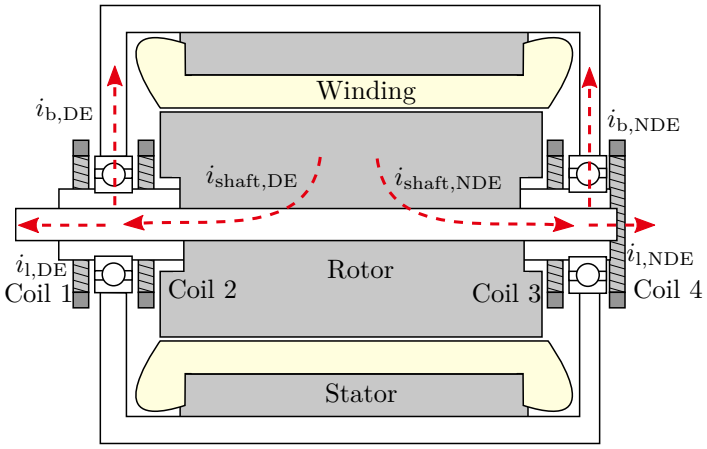

Figure 2.37: Machine axial cross-section with parasitic currents and Rogowski coils for bearing current measurement [48]

The third approach, presented in [48], [53]–[55], is to integrate Rogowski coils into the machine. This approach was chosen for this work. By placing the coils on the left and right sides of the DE and NDE bearings, as illustrated in Figure 2.37, and subtracting the measurements from each other, the bearing current can be measured. The advantage of this method is that apart from the hole for the cable of the Rogowski coil, no mechanical changes to the machine are required, and the parasitic current path remains unchanged. The disadvantage is that the Rogowski coils are placed in an environment that is highly disturbed by electromagnetic interference (EMI) from the end windings of the machine. This imposes high requirements on the CM rejection of the coils. Furthermore, when adding the measured signals from two coils, the measurement error adds up again. When the leakage current is too high, Rogowski coils with a low gain have to be used, increasing the measurement error even more. However, when the leakage current at either end is zero, the respective outer Rogowski coil can be omitted, removing a potential source of measurement error. For the measurements conducted in this work, the machine is operated at no-load, without anything else connected to the shaft. Therefore, only the two inner Rogowski coils are required. In theory, this setup allows to separate the capacitive bearing current from the total measured bearing current. When defining the direction of

the inductive bearing current as shown in Figure 2.38, the DE and NDE bearing currents can be defined as:

$$i_{\mathrm{b,DE}} = i_{\mathrm{b,cap,DE}} + i_{\mathrm{b,ind}} = x i_{\mathrm{b,cap}} + i_{\mathrm{b,ind}} \tag{2.13}$$

and

$$i_{\mathrm{b,NDE}} = i_{\mathrm{b,cap,NDE}} - i_{\mathrm{b,ind}} = (1-x) i_{\mathrm{b,cap}} - i_{\mathrm{b,ind}} \tag{2.14}$$

with $x \in [0,1]$ being the portion of the capacitive bearing current that flows to through the DE of the machine and assuming that the rest of the capacitive bearing current flows through the NDE. Summing the bearing currents from both ends of the machine gives the capacitive bearing current:

$$i_{\mathrm{b,DE}} + i_{\mathrm{b,NDE}} = i_{\mathrm{b,cap,DE}} + i_{\mathrm{b,ind}} + i_{\mathrm{b,cap,NDE}} - i_{\mathrm{b,ind}} = i_{\mathrm{b,cap,DE}} + i_{\mathrm{b,cap,NDE}} = i_{\mathrm{b,cap}} \tag{2.15}$$

When the capacitive bearing current is distributed equally between the two bearings, subtracting the measured currents gives twice the inductive bearing current.

$$i_{\mathrm{b,DE}} - i_{\mathrm{b,NDE}} = i_{\mathrm{b,cap,DE}} + i_{\mathrm{b,ind}} - i_{\mathrm{b,cap,NDE}} + i_{\mathrm{b,ind}} = (2x-1) i_{\mathrm{b,cap,DE}} + 2 i_{\mathrm{b,ind}} \tag{2.16}$$

For $x = 0.5$:

$$i_{\mathrm{b,DE}} - i_{\mathrm{b,NDE}} = (2x-1) i_{\mathrm{b,cap,DE}} + 2 i_{\mathrm{b,ind}} = 2 i_{\mathrm{b,ind}} \tag{2.17}$$

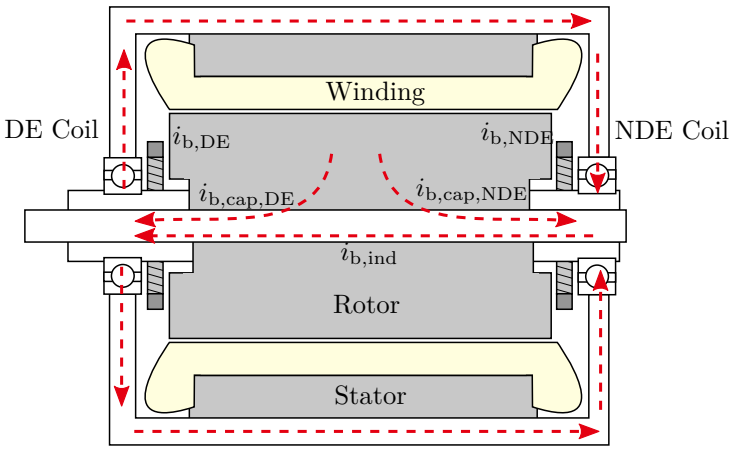

Figure 2.38: Machine axial cross-section with inductive and capacitive bearing current two integrated Rogowski coils

Further bearing current measurement methods include high-frequency near-field probes [56] or antennas [49]. These methods are especially suited for detecting EDM current events.

2.3.2 Rogowski Coils for Bearing Current Measurement

Estimating the bearing current by measuring the shaft current imposes several restrictions on the utilized Rogowski coils. The diameter of the Rogowski coils need to be large enough to fit around the shaft of the machine, while the thickness needs to be small enough to fit into the restricted space between rotor, shaft, bearing and end winding. The CWT MiniHF06 Rogowski coil from PEM UK fits into the available space in the DUT, it is shielded to deal with the expected EMI inside the machine, and it has a gain of 100 $^{\mathrm{mV}}/_{\mathrm{A}}$, which was deemed sufficient for this use.

The measurement method shown in Figure 2.37 is tested on a 5.5 kW induction machine driven by an inverter. The tests are conducted at a dc-link voltage of 100 V and at a speed of 1475 rpm at no-load operation. Two Rogowski coils are placed around the shaft to measure the bearing current. Since the only object connected to the shaft is the DUT, the Rogowski coils only measure the bearing current. Additionally, the shaft voltage is measured via a carbon brush.

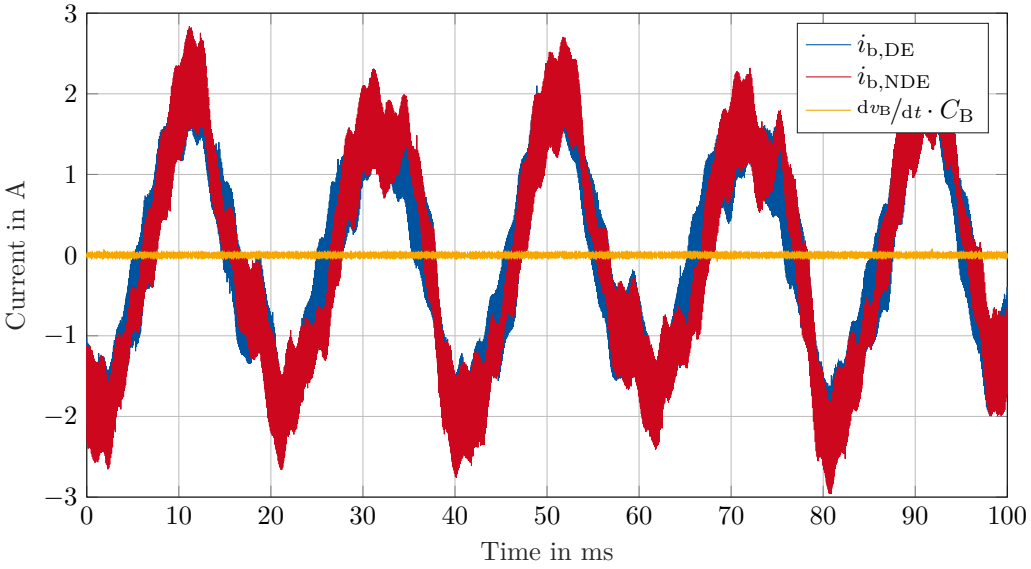

Figure 2.39: Measured $i_{\mathrm{b,DE}}$, $i_{\mathrm{b,NDE}}$ and expected capacitive bearing current

Figure 2.39 shows the measurement results. The measured bearing currents contain large sinusoidal components at the fundamental frequency of the phase current. The expected bearing current is plotted in orange. It is calculated from the derivative of the shaft voltage and the bearing capacitance as

$$i_{\mathrm{B,calc}} = C_{\mathrm{B}} \frac{\mathrm{d}v_{\mathrm{B}}}{\mathrm{d}t}. \tag{2.18}$$

When looking more closely at the switching events (c.f. Figure 2.40 at $t = 4.5\,\mu\mathrm{s}$), it can be observed that the characteristic waveform of the bearing current also appears in

the measured bearing current. Frequency, amplitude and duration of the oscillation are similar. However, it is superimposed with large low-frequency components.

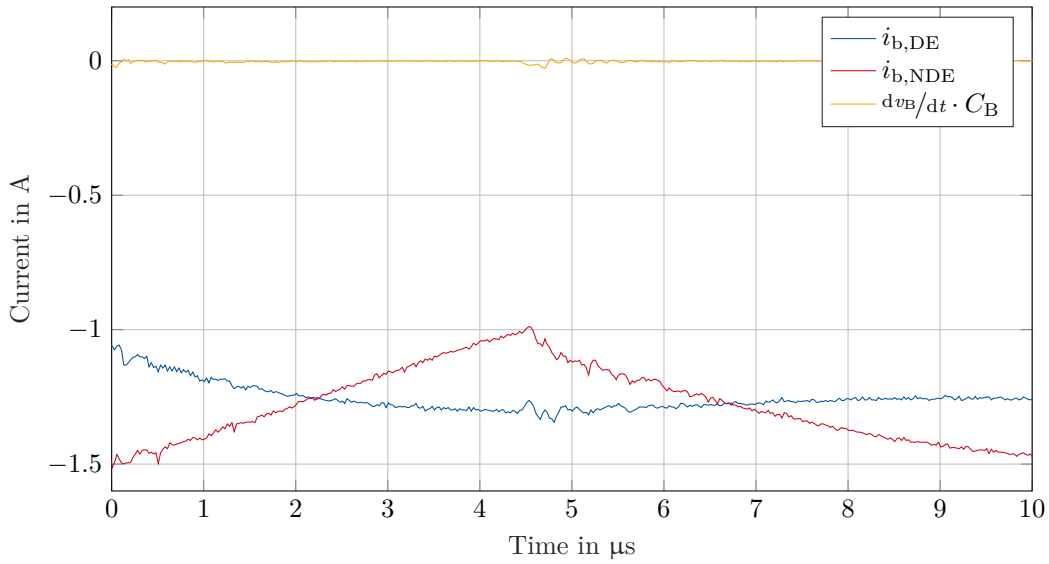

Figure 2.40: Measured $i_{b,DE}$, $i_{b,NDE}$ and expected capacitive bearing current

By looking at the low-frequency spectrum of the bearing current, shown in Figure 2.41, the low frequency components can be identified. At 50 Hz, the fundamental frequency f_s of the phase current can be distinguished. Further, at 640 Hz, the rotor slot harmonics of the machine are visible. This frequency can be calculated as

$$f_{RSH} = f_s \left(\frac{N_B(1-s)}{p} \pm 1 \right) \tag{2.19}$$

with the number of rotor bars $N_B = 28$ and the slip $s = 0.0143$.

The two aforementioned frequency components likely stem from axial stray flux that couples into the Rogowski coil and disturbs the measurements. The spectrum of the axial stray flux that is analyzed in [57] contains the same frequency components.

In order to cope with the disturbances from the axial stray flux inside the machine, in this work, a differential Rogowski coil is developed. It is similar to the one built in [58] and is specially designed for measuring bearing currents in this machine. The design is based on the study presented in [48].

2.3.2.1 Design of a Differential Rogowski Coil

To achieve a differential design, the Rogowski coil is split in half. Using a back and forth winding for each coil half helps mitigate the influence of axial field components in the

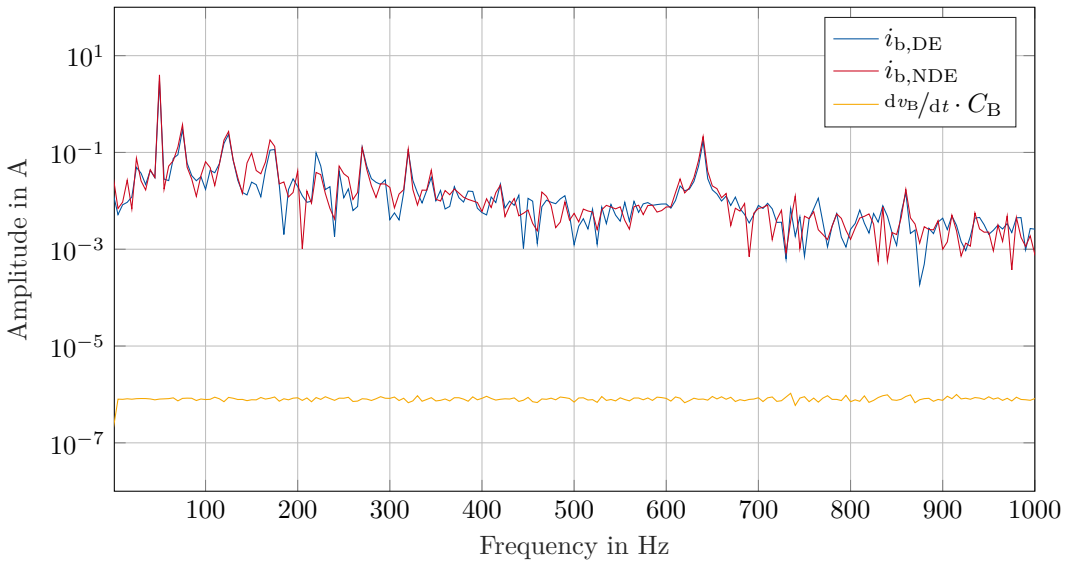

Figure 2.41: Low-frequency spectrum of $i_{b,DE}$, $i_{b,NDE}$ and expected capacitive bearing current

machine. The signals from both coils are then subtracted either in post-processing or directly in the integrator circuit. Thus, common mode disturbances are eliminated and the measured current signal is amplified. The distance between the two coil halves has to be maximized in order to reduce the capacitive coupling and, thus, increase the resonant frequency.

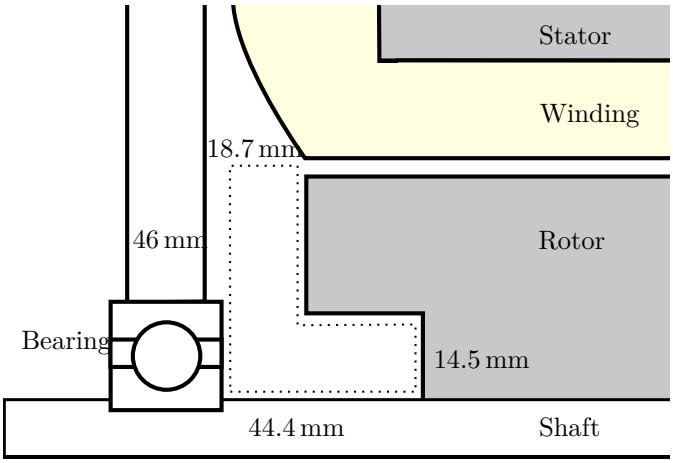

Figure 2.42: Machine axial cross-section with available design space

The design space for integrating the Rogowski coil into the machine is shown in Figure 2.42. In industrial induction machines, such as the investigated machine, where power density is less important than cost, there is plenty of space between the rotor, the windings, the shaft and the end shield of the machine. In machines with a high power density, which is usually the case in e-axles, the available design space is smaller. However, it will

usually still be large enough to integrate a Rogowski coil. The models used in this work require approximately 5 mm of axial space.

Commercially available Rogowski coils usually exhibit a round cross-section, which offers increased flexibility and a simpler winding geometry. The differential Rogowski coil used in this work has a square cross-section. This has two reasons. On one hand, the available design space is rectangular, which means that a coil with a square cross-section will be able to span a larger area. Even though the design space in the investigated machine is not so restricted that a coil with a round cross-section would be a problem, for machines with a high power density, a square cross section can lead to a higher current gain due to a better utilization of the available space. On the other hand, preliminary analytical investigations have proven that Rogowski coils with a square cross section have a three times higher resonance frequency when compared to round Rogowski coils. This is valid assuming that the same square space is available, i.e., that the sides of the square are as long as the diameter of the round coil.

The general requirements for measuring bearing currents are taken from literature. In [6], peak bearing currents of 20 A with frequencies up to 1 GHz have been reported. Shaft voltage measurements of the investigated electric machine showed that an upper bandwidth limit of 100 MHz is sufficient. The supply voltage of the integrator circuit is set to ±10.5 V. This is due to the fact that the output voltage of ±12 V of the galvanically isolated dc-dc converter, which is used as a power supply, has to be filtered by a stage of linear regulators to eliminate noise from the supply voltage. The output voltage of the coil is, therefore, limited to ±10 V. The winding configuration of the proposed Rogowski coil is shown in Figure 2.43. The first coil half is wound clockwise and back while the second coil half is wound counterclockwise and back.

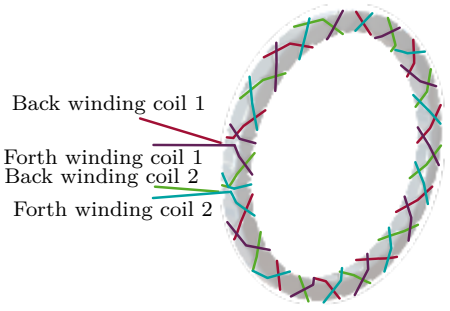

Figure 2.43: Winding configuration of the designed differential Rogowski coil

The coupling inductance M and the self inductance L_S of a Rogowski coil with a rectangular cross section can be calculated by

$$M = \mu_0 \cdot \frac{N \cdot a}{2 \cdot \pi} \cdot \ln\left(1 + \frac{a}{d_{\text{inner}}}\right) \tag{2.20}$$

and

$$L_S = N \cdot M, \tag{2.21}$$

where a is the width of the coil cross section, N is the number of turns and d_{inner} is the inner diameter of the coil. Due to the complex coupling between the two coils, these analytical equations do not accurately calculate the inductance of the Rogowski coil.

In addition to the main design parameters M and L_{S}, the winding resistance R_{W} and the parasitic coupling capacitance C_{W} strongly influence the behavior of the Rogowski coil, especially around its resonant frequency. Usually, Rogowski coils are wound with copper wires and thus require an external resistor to dampen the resonance. In this work, a high-impedance wire made of a copper-nickel alloy with a per-length resistance of $R'_{\text{W}} = 100.8\,\Omega/\text{m}$ was used. Each individual coil has a resistance of $R_{\text{W}} = 46\,\Omega$ and, thus, no external damping resistor is required. Furthermore, internal oscillations inside the coil are dampened directly at the source.

Due to the high number of crossing points between the back and forth windings and the overall complex winding geometry, no simple analytical approach for calculating the parasitic capacitance could be found. Since the 3D model of the bobbin already exists for manufacturing, a finite element method (FEM) simulation is used to extract the coil parameters.

An equivalent circuit model generated from ANSYS Q3D Extractor resulted in a dc self-inductance of 122 nH and a self inductance of 108 nH at 1 MHz. The parasitic capacitance between the two winding halves, which is the largest parasitic capacitance in the coil, has a value of 22.6 pF, which is constant for frequencies up to 1 MHz.

2.3.2.2 Signal Conditioning Circuit

Since the output of the Rogowski coil is the derivative of the current, an additional signal conditioning circuit is required. It features a differential-to-single-ended conversion, an active and a passive integration stage, an amplifier and several filters. The equivalent circuit diagram is shown in Figure 2.44.

The differential Rogowski coil is modeled by its induced voltage V_{Ind}, its self inductance L_{S} and the winding resistance R_{W}. An INA849 instrumentation amplifier by Texas Instruments Inc. converts the differential output voltage of the Rogowski coil into a single-ended signal. The gain is set to 108.

The active integration stage with an integration range from 10.6 Hz to 10.6 kHz is built with a THS4631 operational amplifier (OP) by Texas Instruments. A non-inverting integrator topology is chosen to avoid pre-shoot effects [59], [60]. The passive integration is done by an RC-low-pass filter with its cutoff frequency at 10.6 kHz, achieving seamless integration over a wide frequency range.

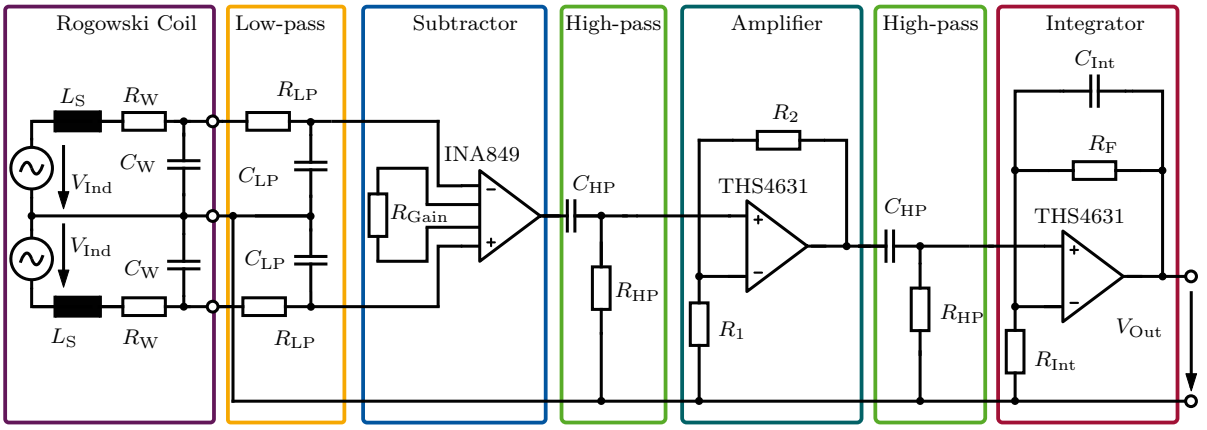

Figure 2.44: Equivalent circuit of the Rogowski coil and the signal conditioning circuit

The RC-low-pass filter shown in Figure 2.44 in orange is placed before the subtractor circuit as a safety measure to dampen transient voltage spikes from the Rogowski coil, which can occur during high current gradients. A resistance $R_{\mathrm{LP}} = 15\,\mathrm{k\Omega}$ and a capacitance $C_{\mathrm{LP}} = 100\,\mathrm{pF}$ result in the required corner frequency of the low-pass filter.

$$f_{\mathrm{LP}} = \frac{1}{2\pi \cdot C_{\mathrm{LP}} R_{\mathrm{LP}}} = 10.6\,\mathrm{kHz} \tag{2.22}$$

The integrator marked in red in Figure 2.44 can be described by the following transfer function:

$$G = \left(1 + \frac{R_{\mathrm{F}}}{R_{\mathrm{Int}}}\right) \cdot \frac{1}{1 + R_{\mathrm{F}} C_{\mathrm{Int}} \cdot s}. \tag{2.23}$$

The integrator capacitance is calculated from the cutoff frequency of the RC low-pass filter as $C_{\mathrm{Int}} = 100\,\mathrm{nF}$.

The high-pass filters marked in green remove unwanted DC and low-frequency components from the measured signal and the output voltage. In order not to disturb the transmission behavior of the circuit, their cutoff frequency is set to

$$f_{\mathrm{HP}} = \frac{1}{2\pi \cdot R_{\mathrm{HP}} C_{\mathrm{HP}}} = \frac{1}{2\pi \cdot 47\,\mathrm{k\Omega} \cdot 100\,\mathrm{nF}} = 34\,\mathrm{Hz} \tag{2.24}$$

The non-inverting amplifier stage, marked in green in Figure 2.44, increases the gain of the circuit to achieve a better signal-to-noise ratio. To achieve a gain of 100, the resistance values are chosen to be $R_{\mathrm{Int}} = 1.5\,\mathrm{k\Omega}$ and $R_{\mathrm{F}} = 150\,\mathrm{k\Omega}$.

Figure 2.45 shows the transfer functions of the different amplifier and filter stages of the signal conditioning circuit shown in Figure 2.44 and the resulting transfer function of the complete system. The transfer functions are acquired from LTspice simulations using component models provided by the manufacturers.

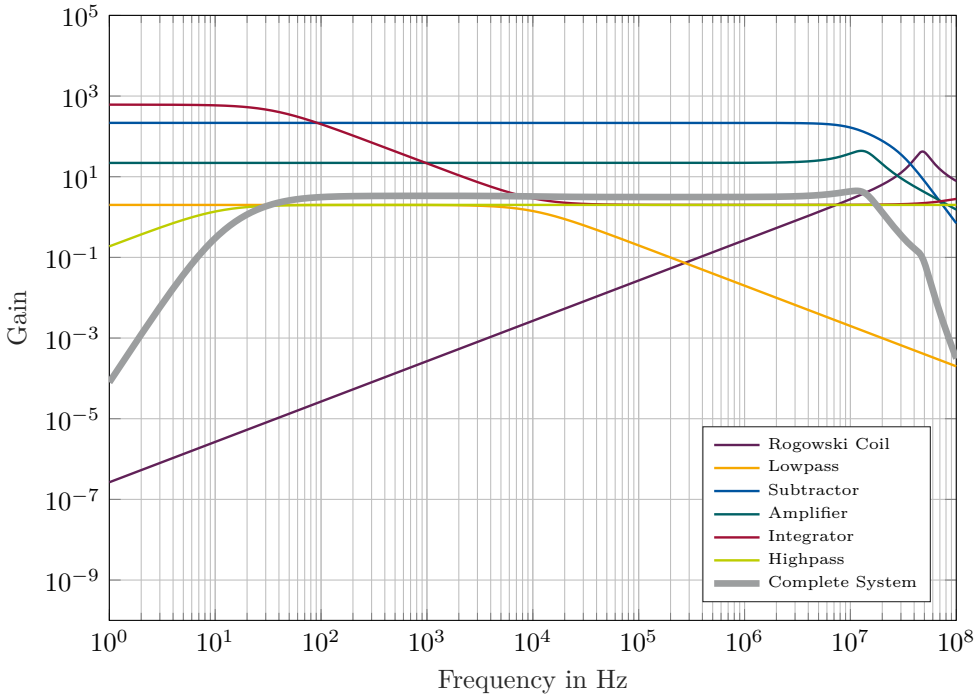

Figure 2.45: Transfer functions of each part of the circuit and the complete system

2.3.2.3 Rogowski Coil Evaluation

In this section, the Rogowski coil developed in [48] is evaluated and compared with two commercially available Rogowski coils, one shielded and one unshielded. The coil that is best suited for bearing current measurements is selected for the measurements presented in chapter 4.

The evaluation is conducted in the frequency domain and in the time domain. First, a Tektronix TTR506A VNA is used to measure the self inductances and the voltage-to-voltage transfer functions of the developed differential coil. To measure the current-to-voltage transfer function of the developed Rogowski coil (together with its signal conditioning circuit), as well as the transfer function of the two commercial Rogowski coils, the measurement setup shown in Figure 2.46 is used.

Figure 2.47a shows the self-impedance of the developed differential Rogowski coil. The two coil halves are measured separately and show a good match with each other in terms of impedance, confirming the high reproducibility and precision achieved with the 3D-printed bobbin. In addition to the high-impedance coil marked as CuNi in the Figure 2.47, the impedance of a copper coil wound on the same bobbin is measured. The measured impedance shows that the resonant frequency is dampened much better in the high-impedance coil, confirming that a high-impedance wire can allow eliminating the external damping resistor. Furthermore, the resonant frequency of the copper coils is at approximately 42 MHz, while the resonant frequency of the high-impedance coils is

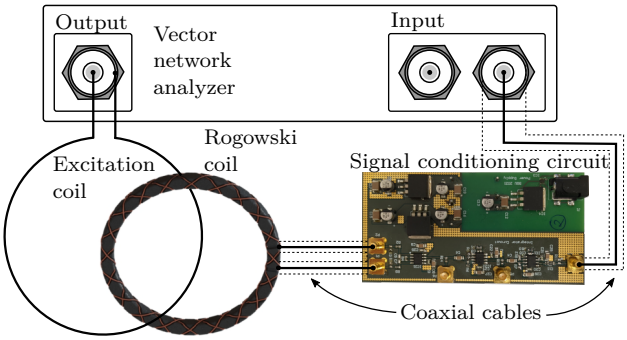

Figure 2.46: Setup for transfer function measurements

slightly lower at 33 MHz. This can be attributed to the different types of insulation used for the wires and the wire diameter. While the CuNi-wire has a fabric insulation, the copper wire is insulated with enamel resin. The CuNi-wire has a diameter of 80 µm while the copper wire has a diameter of 400 µm. The copper wire is, therefore, much more rigid and the crossing points in the copper coils are slightly further apart than in the high-impedance coils. Thus, the parasitic capacitances at the crossing points are higher for the high-impedance wire. Since it can be assumed that the capacitances at the crossing points, i.e., the crossing points between the coil halves and the crossing points between the back and forth windings, dominate the overall parasitic capacitance of the Rogowski coils, the increase of these capacitances is responsible for the reduced resonant frequency.

The voltage-to-voltage transmission ratios of the coils is shown in Figure 2.47b. In a perfectly coupled transformer, a transmission ratio of 0.05 would be expected from the winding ratio. The real transmission ratio is much lower, which is due to the high stray inductance and low number of windings on the primary side. When comparing the transmission ratios of the copper coils and the high-impedance coils, the improved damping of the copper-nickel alloy is clearly visible. Deviations between the coil-halves are attributed to inaccuracies in the coil placement and the winding geometry.

Figure 2.48 shows the measured transfer functions of the developed high-impedance Rogowski coil and the two reference Rogowski coils, as well as the transfer function of the developed system that was extracted from LTspice simulations. Since the VNA is terminated with 50 Ω, the gain of the unshielded reference coil is reduced to 25 $^{\mathrm{mV}}/_{\mathrm{A}}$ and the gain of the shielded reference coil is reduced to 50 $^{\mathrm{mV}}/_{\mathrm{A}}$, in contrast to the expected values of 50 $^{\mathrm{mV}}/_{\mathrm{A}}$ and 100 $^{\mathrm{mV}}/_{\mathrm{A}}$, respectively [61], [62]. According to their data sheets, the −3 dB point of both reference Rogowski coils should be located at 30 MHz. The transfer function measurements show, however, that for the unshielded Rogowski coil, the −3 dB point is passed at around 6 MHz. The −3 dB point of the shielded Rogowski coil matches with the value from the data sheet.

Finally, the CM voltage rejection of all three coils is analyzed. Since the coils are insulated and thus the CM voltage cannot be directly applied to them, a capacitive testing method is developed in this work. The coils are placed between two copper plates that are connected

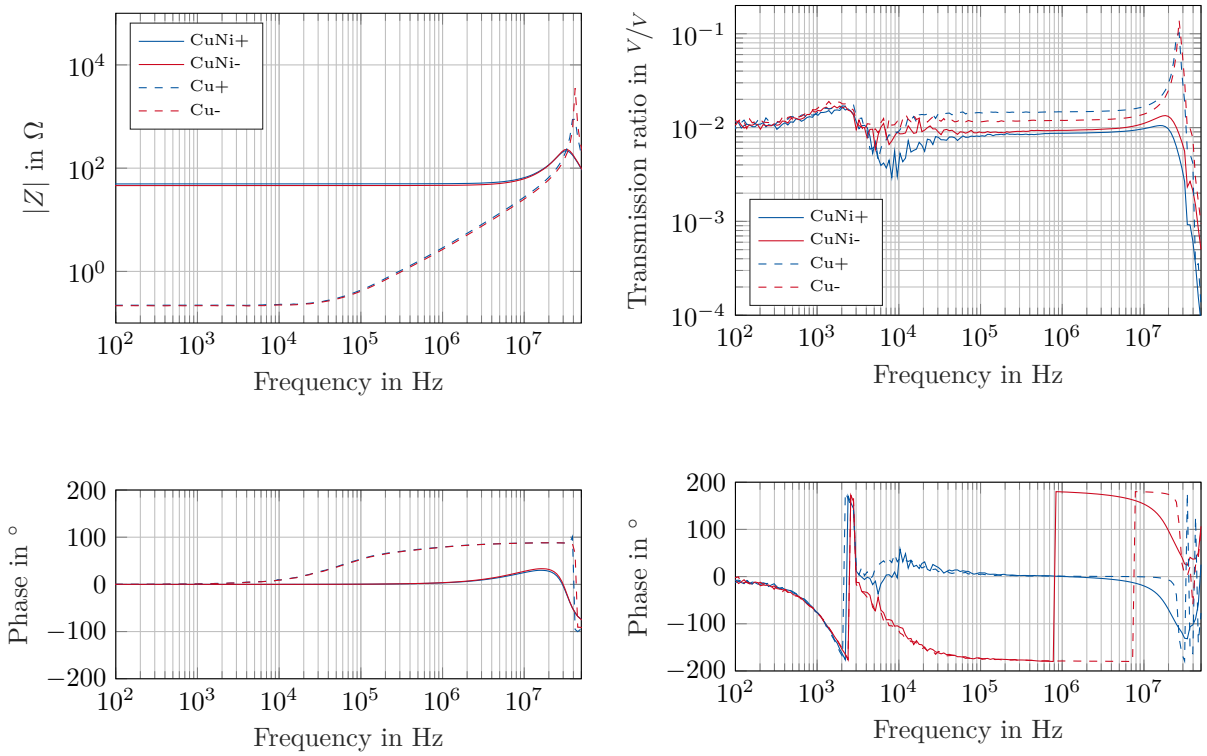

(a) Measured self-impedances of the developed Rogowski coils

(b) Measured voltage-to-voltage transmission ratios of the developed Rogowski coils

Figure 2.47: VNA measurement results

to the output of the VNA. The voltage-to-voltage transfer function from the copper plates to the outputs of the Rogowski coils is measured and used as a qualitative measure for the CM rejection. As a baseline, the copper plates are connected to ground and the output voltage of the Rogowski coils is measured. This measured base noise level is the lower limit, below which the CM rejection cannot be measured anymore. The voltage excitation of the VNA is set to the highest possible level.

Figure 2.49 shows the measurement results. The shielded reference coil suppresses the CM disturbances below its base noise level below 1 MHz. Only at frequencies above 1 MHz, CM disturbances above the base noise level occur. The unshielded reference coil and the developed differential coil are subject to CM disturbances over the whole frequency range. The CM disturbances are also more pronounced at frequencies above 1 MHz. Compared to the base noise level, the shielded reference coil has the highest CM rejection, while the unshielded reference coil has the lowest CM rejection. With a higher precision in the fabrication of the windings, better common-mode rejection can be expected for the developed differential Rogowski coil, since the transmission ratios of the coil halves would match more closely.

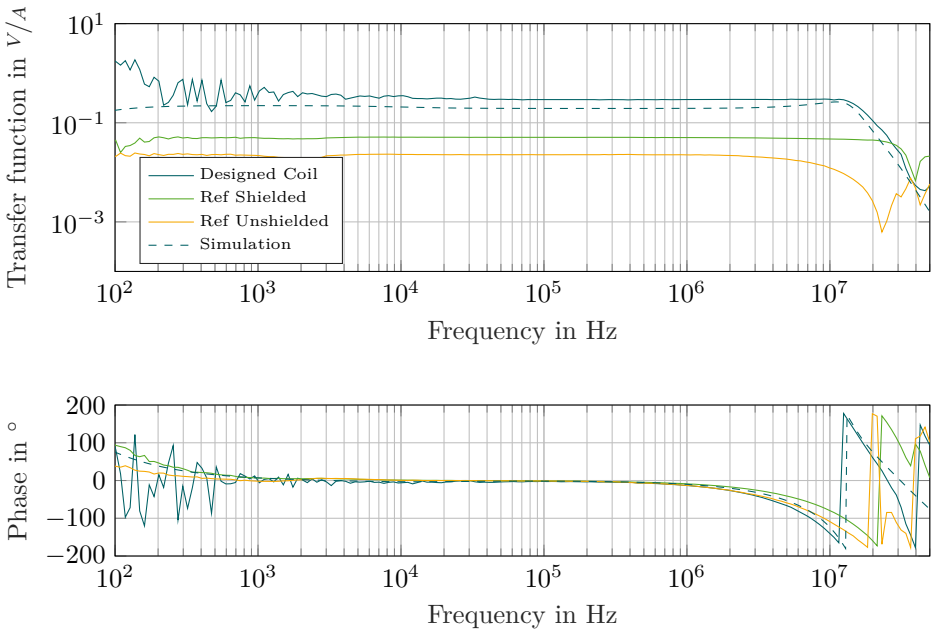

Figure 2.48: Simulated and measured transfer functions of the developed circuit and the shielded and unshielded reference Rogowski coils

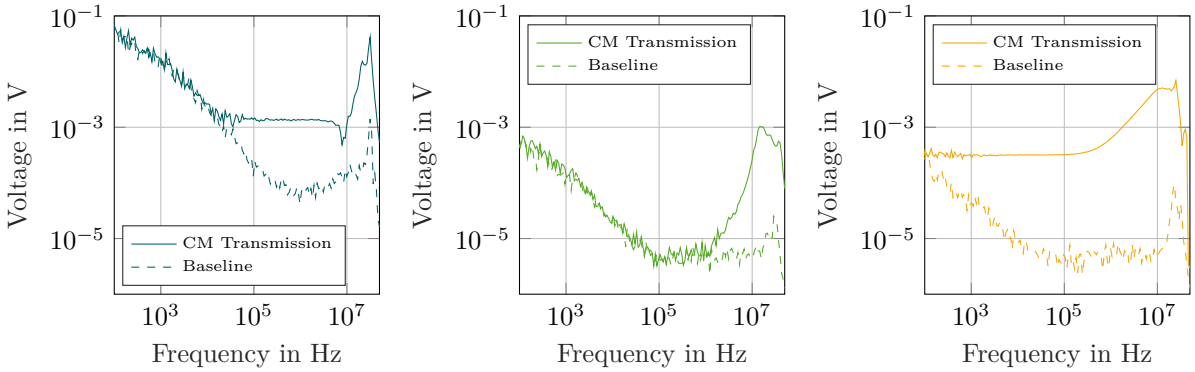

(a) Developed Rogowski coil

(b) Shielded reference Rogowski coil

(c) Unshielded reference Rogowski coil

Figure 2.49: Measured common mode transmission of the three Rogowski coils

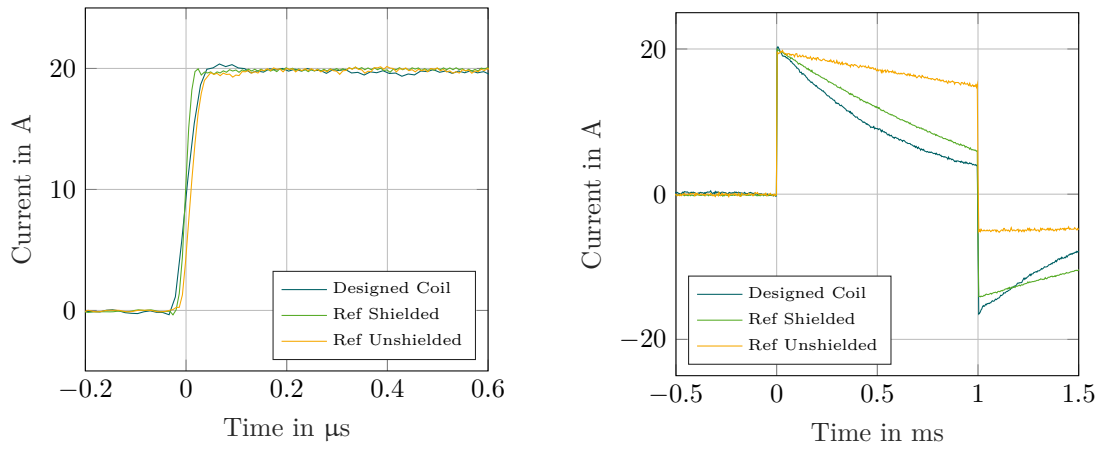

(a) Rising edge of current pulse test

(b) Full current pulse test

Figure 2.50: Current pulse measurements with $i = 20\,\mathrm{A}$ and a pulse duration of 1 ms

After the frequency-domain validation, the three Rogowski coils are tested in the time domain. A KSZ 100 D calibration generator for current probes from PMK is used to generate a trapezoidal current pulse with a rise and a fall time of 15 ns. All three Rogowski coils are used to measure this current.

The measurements in Figure 2.50 confirm the overall design process, but minor differences allow further conclusions. The current gradient measured by the differential coil is slightly lower than that measured by the reference coils. This is due to its lower bandwidth. Over the pulse duration of 1 ms, a droop of 1 % is expected, based on the information from the data sheet of the current probe calibrator [63]. The measured droop is, however, much higher for all three Rogowski coils. This is because of their high lower-end measurement bandwidth. For the shielded reference coil, a droop of 78 % is expected after 1 ms, the measured droop is slightly lower at 70 %. The unshielded reference coil exhibits the lowest droop with a measured value of only 25 % after 1 ms, although 35 % was expected from the data sheet. The developed differential coil exhibits the highest droop with 81 % after 1 ms. All three coils measure the correct current amplitude with nearly no overshoot.

Finally, the differential Rogowski coil and the shielded Rogowski coil are placed around the shaft of the DUT. Since the unshielded reference coil is too short to fit around the shaft of the machine, it is not used for comparison. The measured current is shown in Figure 2.51. The bearing current is still subject to disturbances from axial fields, and additionally, the signal from the designed coil is overlaid with ringing. This likely stems from the signal conditioning circuit and can be ameliorated by improving its design and adding more filter stages. The suppression of axial fields is still not sufficient but could be improved with increased manufacturing accuracy. A printed circuit board (PCB)-based coil, as designed in [58] could be a suitable approach.

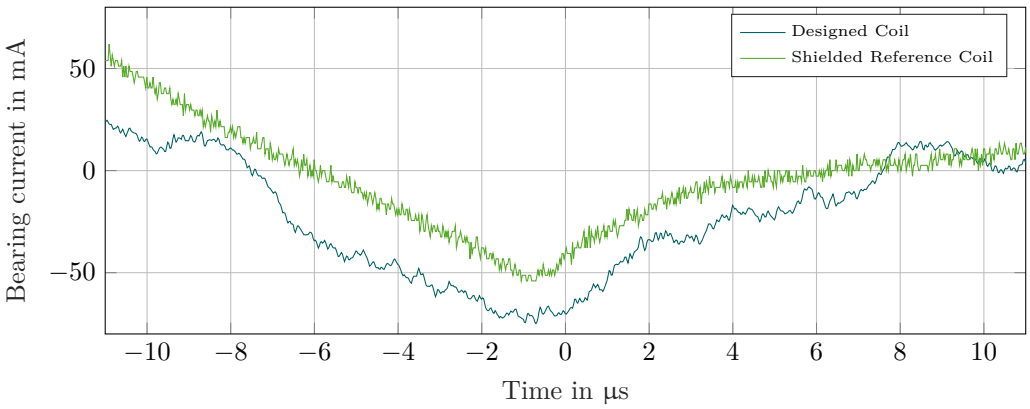

Figure 2.51: Comparison of the developed Rogowski coil and the shielded reference Rogowski coil

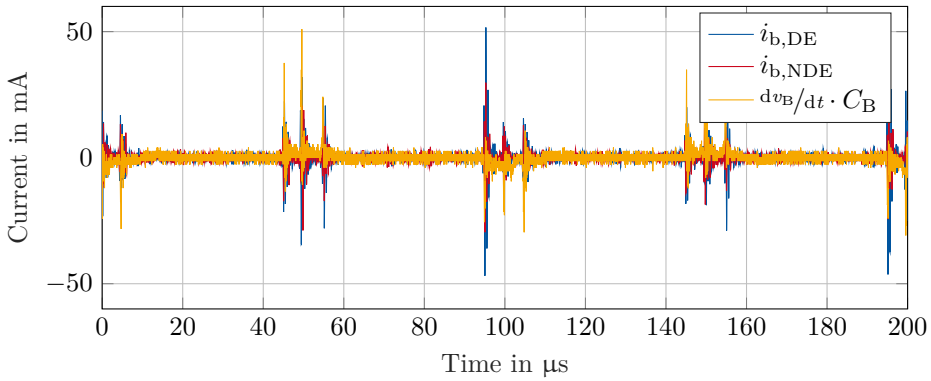

Figure 2.52: Bearing current measurement after high-pass filter

As a result of the evaluation conducted in this section, the shielded Rogowski coil is chosen for the measurements described in chapter 4. It offers the highest CM rejection and lowest base noise level while still mechanically fitting inside the machine. Both coils suffer from disturbances from axial stray flux. An improved design of the differential coil could, however, yield a higher immunity to these disturbances. To address the issue of disturbances from axial stray flux, a high-pass filter is applied to the bearing current measurements. When setting its cutoff frequency slightly below the switching frequency of 10 kHz, the low frequency disturbances are eliminated, as can be seen in Figure 2.52.

2.3.3 Bearing Voltage Measurement

In addition to the bearing current, the bearing voltage is also of interest. It mainly serves as an indicator for EDM currents, since they cannot be directly measured outside of the bearing. Since the shaft of an electric machine is made of steel, measuring the bearing voltage is relatively simple compared to measuring the bearing currents. Usually, a carbon brush is used to contact the shaft close to the bearing. Then, the voltage between the

brush and the stator of the machine is measured, preferably at a location close to the outer raceway of the bearing. This approach is used in this work. The brush is placed on the side of the shaft and the reference potential of the probe is connected directly to the stator using a short cable. Alternatively, a hollow cylinder can be placed over the shaft and the carbon brush can be placed on the front of the shaft as demonstrated in [64].

2.4 Summary

This chapter has given an overview on the fundamentals of parasitic capacitances, and leakage and bearing currents in electric machines. The effects have been incorporated into a high-frequency machine model in section 2.2. Different impedance measurement methods that can be used to acquire different model parameters have been presented in section 2.2.7. In section 2.2.8, a measurement method for the extraction of the distributed parasitic capacitance in rolling element bearings has been presented. Finally, section 2.3 has described how to measure the leakage current, the bearing current and the bearing voltage in electric machines, demonstrating how to design a Rogowski coil for bearing current measurement.

3 Faults in Electric Machines

This chapter introduces the different fault types that can occur in electric machines and their impacts on the behavior of the machines. The next section gives a brief overview over different fault types, their root causes and effects. Since this work focuses on squirrel cage induction machines, faults that only occur in other machine types, such as demagnetization in permanent magnet machines, are omitted.

Afterward, three widely used fault detection techniques, namely motor current signature analysis (MSCA), motor square current signature analysis (MSCSA) and principal component analysis (PCA), are evaluated under different operating conditions, showing some shortcomings. Then, these techniques are combined with machine learning methods to overcome their shortcomings. Finally, an algorithm for the automatic detection and evaluation of electric discharge machining (EDM) events and partial breakdowns in electric machines based on shaft voltage measurements is presented.

3.1 Fault Types and Effects

A comprehensive review of faults in electric machines and their detection is given in [65], [66]. Faults in electric machines can be classified into many different categories. One of the most popular classifications is the distinction between electric and mechanical faults. Since electric machines are electromechanical energy converters and operate both in the electrical and the mechanical domain, this type of classification works well for most faults. Still, there are some faults that can fall into both categories. Other possibilities of classification are the fault location, e.g., rotor, stator or other parts of the machine, or the impact that the faults have on the behavior of the machine. Figure 3.1 shows the fault distribution in induction machines from a study conducted on 940 industrial induction machines in [67]. The classification into electrical and mechanical faults is illustrated by the colors. Mechanical faults are marked in red and electrical faults are marked in blue.

Bearing faults are the most prominent fault type in electric machines. They are caused by many different factors. The main root cause for bearing faults in general is insufficient, unsuitable, depleted, or contaminated lubrication, as shown in Figure 3.2 [68]. All lubrication-related failures are colored in green and sum up to 80 %. The statistical data shown in this figure is however not confined to bearings in electric machines but applies

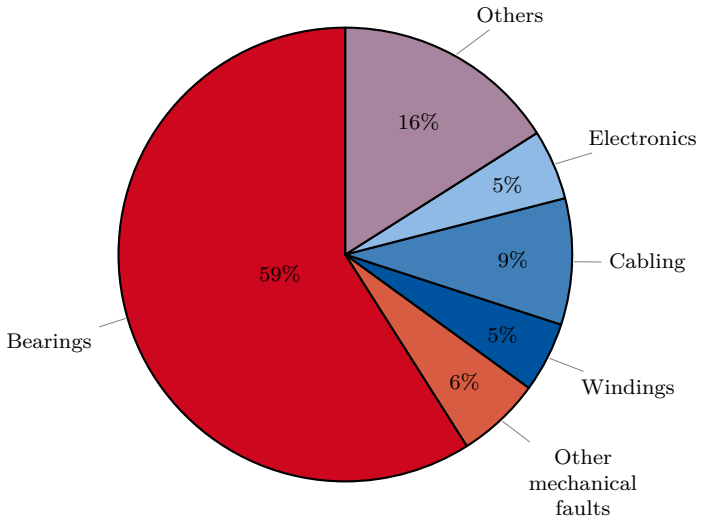

Figure 3.1: Fault distribution in induction machines [67]

to all bearings. In electric machines, more failures are caused by electrical current, but exact incidence could not be found. Nevertheless, lubrication problems are likely the main cause for bearing faults in electric machines as well. The key reason for failure in this study, lubricant contamination, can be counted as ambient stress. The bearing currents described in section 2.1.4 can also damage the bearing depending on their amplitude and frequency of occurrence. Bearing faults have various effects on the operation of an electric machine, but they are usually not immediately fatal. Point defects or increased roughness of the bearing balls and raceways lead to increased vibrations of the rotor and more friction in the bearing. Deteriorated lubricant can increase the friction of the bearing and thus its temperature but will barely be noticeable in torque. When point defects become too large, the bearing can no longer hold the rotor in place, leading to contact between rotor and stator in the worst case.

The most critical electrical faults in electric machines are winding faults. They can be caused by different factors that are mostly related to the aging of the winding insulation. The root causes for winding faults, similar to most other electric machine faults, are the so-called TEAM stresses, i.e., thermal, electrical, ambient, and mechanical stress [69]. High winding temperatures and cyclic thermal stress lead to a rapid deterioration of the winding insulation. These effects are covered in the most widely used models for the lifetime estimation of electric machines [70]. Further, electrical stress, on the one hand from high overvoltages on the phase windings due to, e.g., long motor cables, and on the other hand from steep voltage slopes, can severely damage the winding insulation. Especially when the machine is driven by an inverter with wide-bandgap (WBG) semiconductors, these effects have to be considered in the design stage of the drive [71]. Ambient stress is not a problem in most industrial applications. But when the machine is used in an environment with high humidity, corrosive substances or overall high pollution, its lifetime can be severely reduced [72]. Mechanical stress in the windings mainly occurs during the assembly of the machine. It can be caused by incorrect or careless handling of the

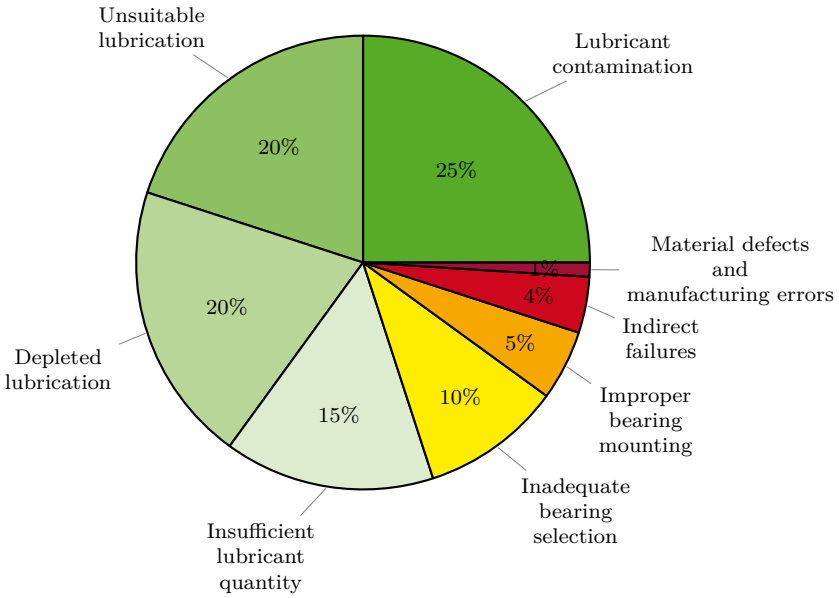

Figure 3.2: Root causes for bearing faults [68]

windings. During the operation of the machine, the windings are protected relatively well inside the housing of the machine. Mechanical damage can however occur when foreign objects enter the machine, or when the rotor hits the stator or due to vibrations or strong current surges [73]. Winding faults usually start as small short circuits between adjacent windings or a winding and the stator [74]. The excessively high current flowing through the short circuit can quickly increase the local winding temperature and cause a rapid fault progression. Winding faults lead to unbalanced phase inductances and thus asymmetrical currents and unbalanced magnetic pull inside the machine. When a phase winding is short-circuited to the stator, the machine has to be shut down immediately to protect the inverter.

In the rotor of a squirrel-cage induction machine (SCIM), mainly two different fault types can occur in the rotor, lamination short circuits and broken rotor bars (BRBs). The rotor bars can break due to repeated thermal stress, unbalanced electromagnetic force, vibrations, dynamic stress from shaft torque or centrifugal force, contamination, bearing failure, or manufacturing problems [65]. Broken rotor bar faults aggravate slowly and do not immediately cause a machine standstill. However, they cause torque and speed oscillations, damaging other drive-train components. Thus, it is imperative to detect incipient BRB faults early and start appropriate maintenance procedures.

3.2 Evaluation of Classical Fault Detection Methods

A comprehensive overview of different fault detection methods is given in [75]. This section evaluates three of them, namely motor current signature analysis, motor square current signature analysis and principal component analysis. After a brief introduction of these methods, the effect that bearing faults and broken rotor bars have on the fault indicators F are described and analyzed under different operating conditions. Significant details of this section and section 3.3 were published by the author within the scope of this work in [76]–[78].

3.2.1 Fault Detection Methods

MSCA and MSCSA are commonly used fault detection methods [79]. They are often successfully applied in grid-connected machines with quasi-static operating points [80]. These two methods function similarly. In MSCA, the frequency spectrum of the phase current is investigated [81]. Since the current signals are measured as real-valued discrete time sequences, the discrete Fourier transformation is used to acquire the spectrum. In applications where fast fault detection is required, the fast Fourier transformation can increase the efficiency of the calculation of the spectrum.

Different faults can cause additional frequency components $I(f_{\text{fault}})$ in the phase current of an electric machine, which do not occur or have a lower amplitude in a healthy machine. Fault indicators, i.e., numerical values that allow to estimate if a fault has occurred and ideally how severe it is, are usually calculated by dividing the amplitude of one of the fault-related frequency components by the amplitude of the fundamental component $I(f_{\text{s}})$.

$$F_{\text{MCSA}} = \frac{|I(f_{\text{fault}})|}{|I(f_{\text{s}})|} \tag{3.1}$$

When the exact frequency components that are required for the fault indicator are known, instead of the full spectrum, only the specific fault frequency components are calculated, increasing the computational efficiency.

In MSCSA, the same type of analysis is conducted on the spectrum of the square of the phase current. When the drive experiences low-frequency load torque oscillations, additional frequency components occur in the phase current [82]. These frequency components may overlap with fault-related frequency components and inhibit fault detection. The spectrum of the squared phase current exhibits strong similarities to the instantaneous power spectrum presented in [83] and thus gives more information than the phase current spectrum. Moreover, it only requires the measurement of the phase current [82].

$$F_{\mathrm{MSCSA}} = \frac{I^2(f_{\mathrm{fault}})}{I^2(f_{\mathrm{s}})} \tag{3.2}$$

Nowadays, more and more machines are driven by inverters due to the demand for high dynamics and efficiency. These machines operate over a wider range of operating points compared to directly grid-connected machines. Especially in mobile applications, where highly integrated e-axles are often used, electric machines will be driven by inverters and will be subject to a broad range of operating points.

PCA is often used for dimensionality reduction [84]. It extracts a set of orthogonal vectors called principal components. In fault detection for SCIM, it can be used as a pattern recognition method based on the Clarke transformation to obtain current patterns. For further explanations on the Clarke transformation, c.f. [85]. In a healthy machine supplied with perfectly sinusoidal currents, the α and β components of the phase current form a circle centered around the origin. When a fault occurs, the amplitude of i_α and i_β is modulated by the characteristic fault frequencies [84]. First, the correlation matrix E of the current vector S is calculated as

$$E = S^T \cdot S. \tag{3.3}$$

Then, the corresponding Eigenvectors v and Eigenvalues λ are calculated with

$$E \cdot v = v \cdot \lambda. \tag{3.4}$$

The first two Eigenvalues λ_1 and λ_2 are constant and equal for a healthy SCIM. When fault frequency components occur, they lead to a variation of the Eigenvalues over time. In [84], this is used for broken rotor bar fault detection in a SCIM and [86] applies PCA for bearing fault detection. Different properties of the Eigenvalues are analyzed depending on the type of fault that is to be detected.

3.2.2 Bearing Faults

Bearing faults in electric machines come in different variations. The types of bearing faults that are of most interest for fault detection are point defects and increased roughness of the raceways and the bearing balls. While increased roughness leads to an overall increase in vibrations, point defects excite very specific vibration frequencies that also translate to the phase current [87]. The mechanical frequency with which a bearing ball passes over the fault location can be calculated similarly to the cage speed of the bearing as

$$f_{\mathrm{m,BFo}} = \frac{N_{\mathrm{B}}}{2} f_{\mathrm{mech}} (1 - \frac{D_{\mathrm{b}}}{D_{\mathrm{p}}} \cos\beta) \tag{3.5}$$

for a fault on the outer raceway. For a fault on the inner raceway, the equation changes as follows:

$$f_{\mathrm{m,BFi}} = \frac{N_{\mathrm{B}}}{2} f_{\mathrm{mech}} (1 + \frac{D_{\mathrm{b}}}{D_{\mathrm{p}}} \cos \beta). \tag{3.6}$$

When a fault occurs on one of the bearing balls, the frequency of occurrence is equal to twice the spin frequency and can be expressed as

$$f_{\mathrm{m,BFb}} = \frac{D_{\mathrm{p}}}{D_{\mathrm{b}}} f_{\mathrm{mech}} (1 - \frac{D_{\mathrm{b}}}{D_{\mathrm{p}}} \cos \beta). \tag{3.7}$$

N_{B} is the number of balls, f_{mech} is the rotor frequency, D_{b} is the bearing ball diameter, D_{p} is the ball pitch diameter and β is the contact angle. These parameters are illustrated in Figure 3.3. Every time a bearing ball passes over the fault location, a vibration is excited. These incidents are also visible in the stator currents. The mechanical fault frequency $f_{\mathrm{m,BF}}$, therefore, translates to a frequency f_{BF} in the current spectrum:

$$f_{\mathrm{BF}} = |f_{\mathrm{s}} \pm k \cdot f_{\mathrm{m,BF}}|, \tag{3.8}$$

where f_{s} is the fundamental frequency and $k = 1,2,3...$ is the harmonic index [87]. Note that this is not the frequency of the vibration itself, which strongly depends on the mechanical properties of the whole machine, but only the frequency of the occurrence of these incidents, i.e., the frequency with which the vibration is excited.

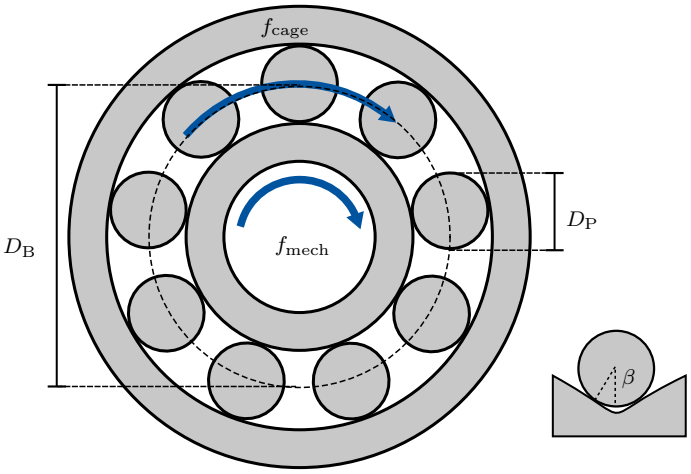

Figure 3.3: Illustration of geometrical bearing parameters from equations (3.5) to (3.7)

These frequency components are used in MSCA and MSCSA to detect the presence of bearing faults. In contrast, PCA is usually applied to the vibration signals instead of current signals, requiring additional sensors [88].

3.2.3 Broken Rotor Bars

Broken rotor bars give rise to additional frequency components in the phase current of a SCIM. These frequency components are caused by the unsymmetrical rotor inductance and by the resulting torque oscillations. They are described by the following equation:

$$f_{\mathrm{BRB}} = f_{\mathrm{s}}(\frac{k}{p} \cdot (1 - s) \pm s), \tag{3.9}$$

where f_{s} is the fundamental frequency, s is the slip, p is the number of pole pairs and k = 1,2,3... is the harmonic index [80]. These frequency components can be directly used in MSCA and MSCSA. For PCA, the relative peak-to-peak magnitude of the oscillation of the first Eigenvector can be used for fault detection.

$$F_{\mathrm{PCA}} = \frac{\lambda_{j\,\max} - \lambda_{j\,\min}}{\lambda_{j\,\max}} \tag{3.10}$$

where $\lambda_{j\,\max}$ and $\lambda_{j\,\min}$ are the maximum and minimum eigenvalues during the considered time period. In [78], the value is around 0.04 for a healthy machine and around 0.08 for a machine with one broken rotor bar. Accurate detection is possible after approximately 16 fundamental periods in one operating point, i.e., 1.6 s in the study conducted in [78]. Both the classification limit for the fault indicator F_{PCA} and the time required to reliably estimate the state-of-health strongly vary with the operating point and the investigated machine.

In the next section, the influence of the operating point and of the fault severity on BRB fault detection is investigated. Figure 3.4 shows the configurations of broken rotor bars that are investigated. They were chosen to emulate a fault progression starting from a healthy machine. The half and three-quarter broken rotor bars in Figure 3.4a and Figure 3.4b are incipient faults. For the emulation of fully broken rotor bars, the number of broken bars is increased from one (c.f. Figure 3.4c) to four bars (c.f. Figure 3.4e) . Finally, the influence of the arrangement of the broken bars is analyzed by placing the four broken bars in groups of two bars located on opposite sides of the rotor (c.f. Figure 3.4f). The faults were created by drilling holes into or through one or more rotor bars.

3.2.4 Test Bench

The fault detection methods presented in the previous sections are evaluated on a test bench with a 5.5 kW SCIM driven by an adapted version of the two-level SiC inverter developed in [89], [90] and connected to a speed-controlled load machine. The inverter of the load machine is connected to the inverter of the device under test (DUT) via a dc-dc-converter, thus allowing to circulate the energy needed for the operating point of

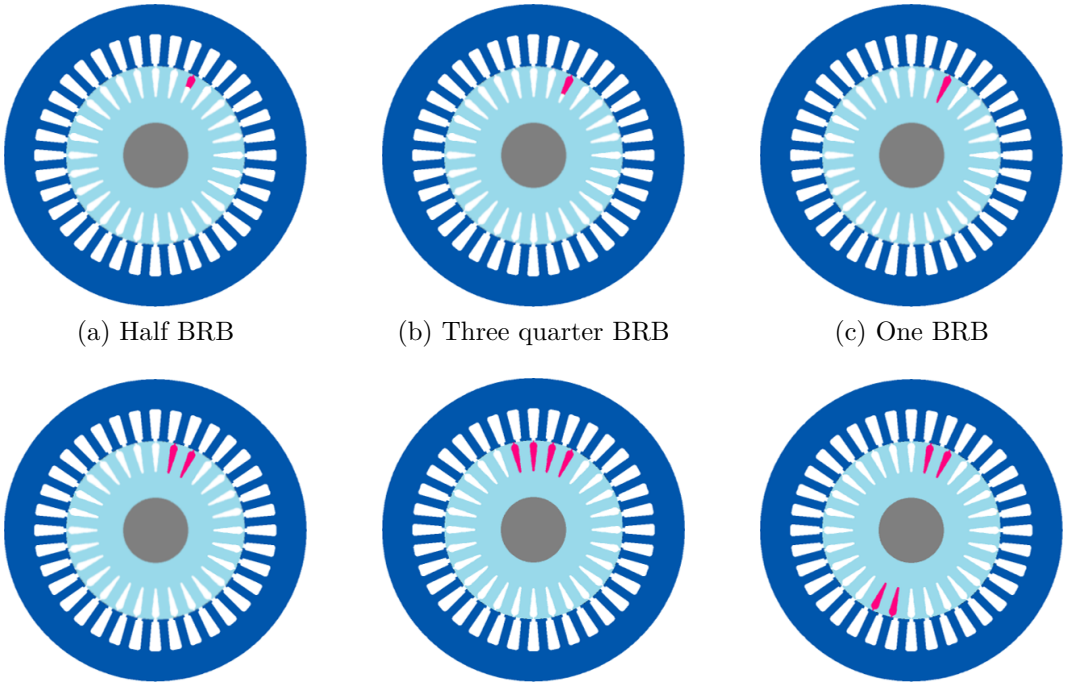

(a) Half BRB (b) Three quarter BRB (c) One BRB

(d) Two BRB (e) Four BRB (f) Two by two BRB

Figure 3.4: SCIM cross section with investigated BRB configurations

the machine and only drawing the losses from the grid. The nameplate data of the DUT is given in Table 2.1.

3.2.5 Influence of the Operating Point

As shown in [76], MSCA fault detection accuracy for broken rotor bars strongly depends on the operating point. The frequency spectrum of the phase current of a SCIM with one broken rotor bar under varying slip with a constant phase voltage is shown in Figure 3.6. Figure 3.6a shows the full spectrum. The variation of the slip frequency from $-0.5\,\mathrm{Hz}$ to $0.5\,\mathrm{Hz}$ shifts some speed-dependent frequency components while the fundamental electrical frequency and its harmonics naturally remain at the same frequency point. Figure 3.6b shows the fundamental frequency and the peaks in the spectrum that are caused by the BRB. With lower absolute slip, the amplitude of these peaks decreases. Furthermore, the baseline of the spectrum increases near the fundamental frequency. These two effects combined lead to a reduction in the difference of the fault indicator F_{MCSA} between a healthy and a faulty machine for smaller slip values. For the healthy machine, F_{MCSA} increases for small absolute slip values. For the machine with a broken rotor bar, it decreases. Thus, broken rotor bar fault detection becomes less and less accurate with decreasing load and is nearly impossible with MSCA for very small loads or in no-load operation.

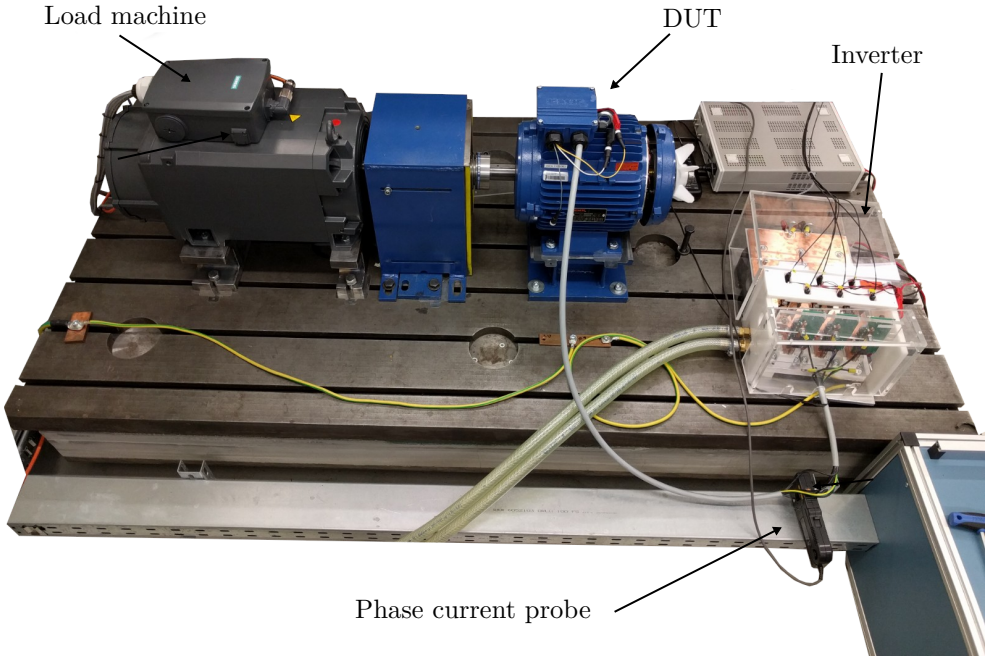

Figure 3.5: Test bench setup for the evaluation of fault detection algorithms

When looking at the fifth and seventh harmonics in Figure 3.6c and Figure 3.6d, there are also BRB-related sidebands that can be used for fault detection. They are much less affected by low slip values, and the baseline of the frequency spectrum is also much more constant around the harmonics than it is around the fundamental frequency. However, BRB fault detection around the fifth and seventh harmonics still suffers from poor performance at very low load. Further investigations have shown a substantial variation of these fault indicators depending on the phase current amplitude. Thus, they are not well suited for fault detection under varying load conditions.

The strong variation of the fault indicator depending on the operating point is also an issue with MSCSA and PCA, as shown in Figure 3.7. Here, the phase current and the fault severity are varied. The measurements have been conducted at a constant speed of 285 rpm and a fundamental frequency of 10 Hz, i.e., a slip of 0.05. An ideal fault indicator would be constant over the phase current and would increase with increasing fault severity. A possible fault indicator limit, above which a machine would be classified as faulty, is marked with a black dashed line. A large difference between the healthy case fault indicators marked in green and the fault indicators for the different fault severities facilitates fault detection and classification. With the right choice of fault indicator, both MSCA and MSCSA allow the detection of incipient faults starting from a 1/2 broken rotor bar, depending on the phase current. Fault severity estimation is however difficult since the case with one broken rotor bar has led to the highest fault indicator values.

PCA, on the other hand, gives no clear indication of fault severity. The fault indicator strongly varies with the phase current amplitude. For low phase currents, fault detec-

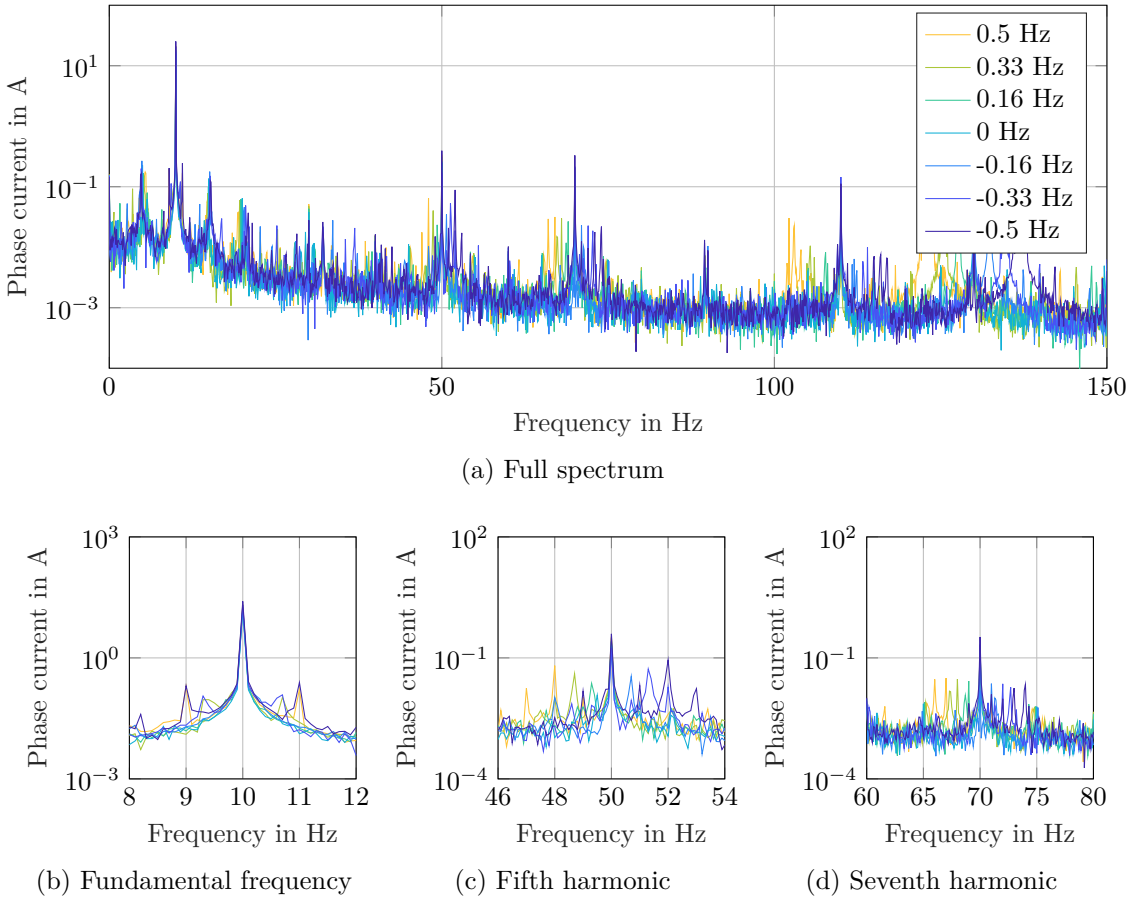

(a) Full spectrum

(b) Fundamental frequency

(c) Fifth harmonic

(d) Seventh harmonic

Figure 3.6: Phase current spectrum of a SCIM with one broken rotor bar

tion and classification are not possible. For higher phase current values, a suitable fault indicator limit can be found to at least detect a fully broken bar and more severe faults.

To investigate the influence of the slip, the measurements are repeated at a constant speed of 295 rpm and a fundamental frequency of 10 Hz, i.e., a slip of 0.017. Here, the picture looks very different. Incipient faults can no longer be reliably detected. Fault indicators for different states-of-health overlap, making an unambiguous fault classification impossible. While all three fault indicators exhibit a trend of increasing with increasing fault severity, reliable fault detection is only possible with MSCA and MSCSA and for fully broken bars. For PCA, no clear limit for a fault indicator can be set that reliably separates healthy and faulty machines.

Thus, classical fault detection methods are unsuitable for applications with a wide range of operating points. Whether the problem of unreliable fault detection in low-load operating points is actually a problem strongly depends on the operating strategy. As already discussed in section 3.1, broken rotor bars usually take some time to develop and worsen. Thus, it might be sufficient to only apply the fault detection algorithm in high load operating points or to shift the electrical operating point of the machine to higher

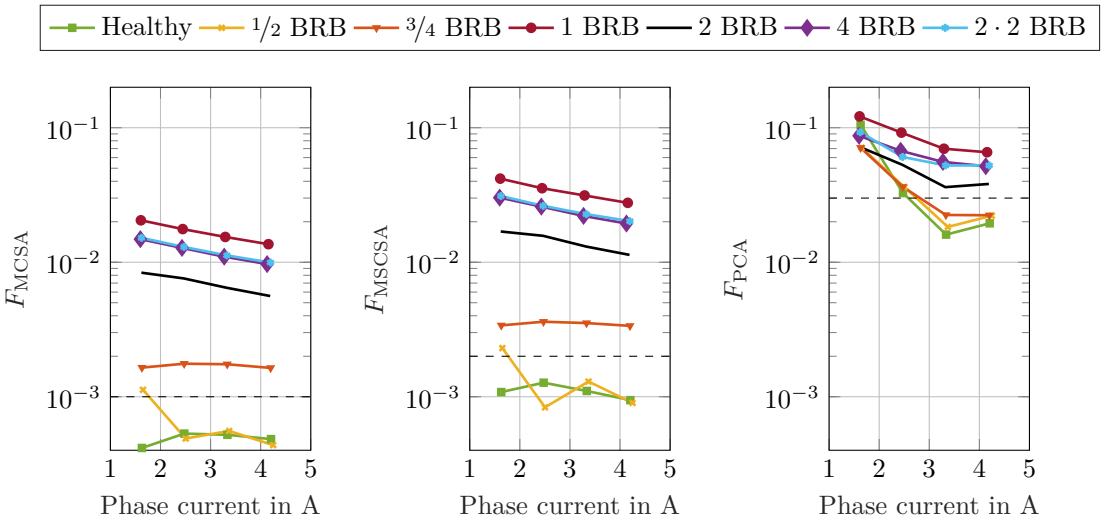

Figure 3.7: MSCA, MSCSA and PCA fault indicators under varying phase voltage and state-of-health at 285 rpm and 10 Hz

slip by reducing the flux for short periods, e.g. for 1 s every 10 min. Still, for reliable fault detection, relatively long current samples are required to achieve the necessary frequency resolution. If the operating point varies too much during the acquisition time, the spectrum will blot out, and fault detection will be inhibited as well [79].

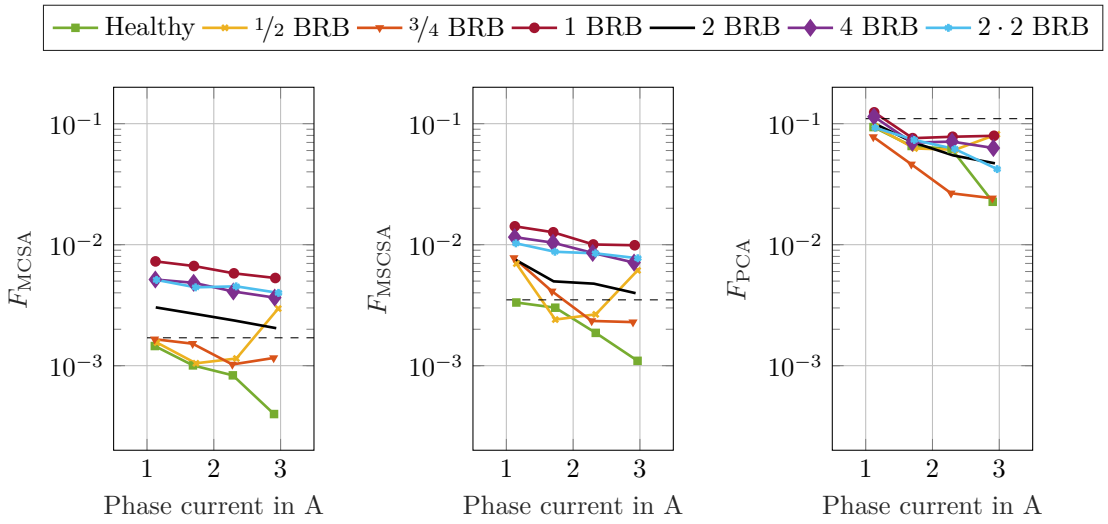

Figure 3.8: MSCA, MSCSA and PCA fault indicators under varying phase voltage and state-of-health at 295 rpm and 10 Hz

3.3 Combination of Classical Fault Detection Methods and AI-based Methods

To overcome the limitations of classical fault detection methods, the fault detection thresholds have to be adapted depending on the operating point. One way to achieve this is to use machine learning methods. Machine learning methods excel at classification tasks and are thus well suited for fault detection and even fault severity estimation. The literature shows that classifiers based on a k-nearest neighbor (k-NN) algorithm or an artificial neural network (ANN) can accurately classify BRB faults in induction machines [91]. Several studies have also achieved promising results using a support vector machine (SVM), which is a supervised learning model suited for non-linear classification [92]–[96]. However, interpreting the diagnosis results obtained by ANNs is not easy when dealing with complex problems such as fault detection in electrical drives [91]. Besides, training ANNs usually takes considerable time.

Table 3.1: Features used for k-NN-classification

Method	Features
MCSA	$I_{\mathrm{s,MCSA}}$, $I_{\mathrm{lsb,MCSA}}$, $I_{\mathrm{rsb,MCSA}}$, $SF_{\mathrm{lsb,MCSA}}$, $SF_{\mathrm{rsb,MCSA}}$,s
MSCSA	$I_{\mathrm{s,MSCSA}}$, $I_{\mathrm{lsb,MSCSA}}$, $I_{\mathrm{rsb,MSCSA}}$, $SF_{\mathrm{lsb,MSCSA}}$, $SF_{\mathrm{rsb,MSCSA}}$,s

Therefore, this thesis proposes to combine MSCA and MSCSA fault indicators with a k-NN algorithm to estimate broken rotor bar fault severity in an induction machine in the whole operating range. The features that are used for fault detection are listed in Table 3.1. $I_{\mathrm{s,MCSA/MSCSA}}$, $I_{\mathrm{lsb,MCSA/MSCSA}}$, $I_{\mathrm{rsb,MCSA/MSCSA}}$ are the magnitudes of the fundamental component, the first left and the first right sideband components in the

current spectrum and the squared current spectrum, respectively. $SF_{\mathrm{lsb,MCSA/MSCSA}}$ and $SF_{\mathrm{rsb,MCSA/MSCSA}}$ are the ratio of I_{s} to I_{rsb} and I_{lsb}, respectively, similar to the fault indicators from equations (3.1) and (3.2). These features were selected due to their successful application in earlier studies on BRB detection in inverter-fed induction machines [97], [98]. They are applied to measurement data from an induction machine with the different manifestations of broken rotor bars shown in Figure 3.4 in combination with three different classification algorithms.

The features were extracted from a data set of 840 measurements with one healthy machine and the six broken rotor bar conditions illustrated in Figure 3.4. The measurements were conducted at four different supply voltages (20 V, 30 V, 40 V, and 50 V) and three different slip values (0.0167, 0.0333, and 0.05) at a fundamental frequency of 10 Hz. Taking all three phase currents into consideration, this leads to 360 data points per state-of-health. For the training of the different algorithms, a random selection of 48 data points per state-of-health is used as test data. The remaining 312 data points are used for training and validation in the MATLAB® classification toolbox. Five-fold cross-validation is used to evaluate the performance of different classifiers. In every training and testing iteration, multiple classifier models are trained with the same four randomly chosen subsets, and then validated with the remaining subset.

Table 3.2: Performance evaluation of the investigated classifiers under various feature selection schemes

Feature selection schemes	**Average accuracy in %**		
	Fine Gaussian SVM	Weighted k-NN	**Subspace** k-NN
MSCA features	76.5	80.1	92.3
MSCSA features	62.8	65.6	87.4
MSCA + MSCSA features	70.7	71.3	96.4
MSCA + MSCSA features + slip	73.2	74.6	97.4
MSCA + MSCSA features + slip (with dimensionality reduction using PCA)	71.8	81.7	96.2

Table 3.2 shows the classification performance for different combinations of features and classification algorithms. The SVM approach only leads to poor classification accuracy when compared to k-NN, regardless of the choice of input parameters. In subspace k-NN, the training data are divided into random subsets to reduce correlation and increase the fault classification accuracy. A subspace k-NN algorithm with $k = 30$ and six subspaces, combined with MSCA and MSCSA fault indicators, fundamental current amplitude, and information on the slip leads to the highest classification accuracy of 97.4 %. When using PCA for dimensionality reduction and reducing the number of inputs from eleven to five, the average classification accuracy is reduced to 96.2 %. When looking at the overall fault detection accuracy, i.e., how many faulty machines are classified as faulty, the average accuracy increases to 98.2 %. The confusion matrix shown in Table 3.3 shows that mostly

incipient faults like a 3/4 broken rotor bar are falsely classified as healthy, while more severe faults are classified accurately.

Table 3.3: Confusion Matrix for the developed classification algorithm

		Classification result							Correct	Wrong
		0	1/2	3/4	1	2	4	2 · 2		
True class	0	93 %	1 %	5 %		1 %			93 %	7 %
	1/2	1 %	98 %	1 %					98 %	2 %
	3/4	4 %		96 %					96 %	4 %
	1				99 %	1 %			99 %	1 %
	2	1 %			1 %	98 %			98 %	2 %
	4						99 %	1 %	99 %	1 %
	2 · 2						1 %	99 %	99 %	1 %

The training time of the different evaluated algorithms depends on the classifier type and the number of selected features and data points for training and validation. Overall, the training of the SVM and weighted k-NN-based classifiers took less than 20 s, while the training of the subspace k-NN classifier took approximately 50 s on a standard computer. The subspace k-NN provides an efficient and precise diagnosis and reduces misinterpretation of fault indicators as shown in section 3.2.5.

3.4 Bearing Diagnosis from Shaft Voltage

This section focuses on the detection of EDM events in electric machines. The fundamentals of EDM currents are presented in section 2.1.4. EDM events in rolling element bearings can be detected in the shaft voltage [49]. When a full bearing breakdown occurs, the shaft voltage is reduced to zero. Since the shaft voltage is coupled to the common-mode (CM) voltage via the bearing voltage ratio (BVR) (c.f. equation (2.8)), it is usually not zero in a machine driven by a two-level inverter. Furthermore, the shaft voltage should only change when the CM voltage changes, since the two voltages are capacitively coupled. The measurements in section 2.2.9 show that the shaft voltage cannot be calculated only from the CM voltage but is actually composed of the CM voltage and the neutral point voltage. However, the BVR can be used as a first guess and the CM voltage is often more easily accessible than the neutral point voltage. Note that the BVR is no longer

valid after a breakdown event. The voltage at the instant of the breakdown $v_{\mathrm{B}}(t_{\mathrm{EDM}})$ is subtracted from the shaft voltage and acts as an offset from the BVR. Equation (2.8) thus has to be adapted as follows:

$$v_{\mathrm{B}}(t) = v_{\mathrm{CM}}(t) \cdot \frac{C_{\mathrm{WR}}}{C_{\mathrm{WR}} + C_{\mathrm{RS}} + 2C_{\mathrm{B}}} - \sum_i v_{\mathrm{B}}(t_{\mathrm{EDM},i}). \tag{3.11}$$

In order to facilitate the detection of breakdown events in the bearing voltage, the voltage waveform is segmented into time periods between switching events in any of the three phases. The switching events are detected from the CM voltage and are marked in Figure 3.9. The dashed lines mark the switching events and the numbers correlate to the segments. In segment one, a partial breakdown and a full breakdown occur. In the second and third segment, the lubricant film withstands the applied voltage. In the fourth segment, there is another partial breakdown followed by a full breakdown. In the fifth segment, the lubricant film again withstands the voltage. In the sixth and seventh segments, the lubricant film breaks down immediately during the switching event and the voltage stays at zero volts.

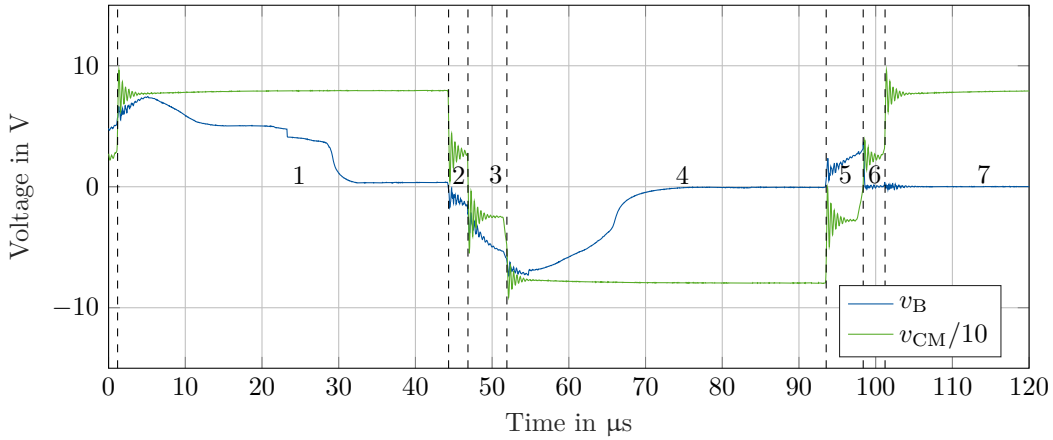

Figure 3.9: CM voltage and shaft voltage with marked switching events and segments

The algorithm for the breakdown detection is illustrated in Figure 3.10. First, a bearing voltage waveform is read. Then, the switching events are detected and are used to segment the waveform into the seven previously introduced switching periods. Since the amplitude of the shaft voltage can only increase during a switching event and is zero after a full breakdown, only one full breakdown can occur in each segment. The following steps are conducted for each segment of the voltage. When the average voltage in the switching period is below a certain threshold, in this case 0.2 V, a breakdown has occurred at the beginning of the segment. If the voltage is above the threshold, the mean voltage of the last 20 samples is calculated. If it is below the threshold of 0.2 V, a breakdown has occurred somewhere in this segment. The algorithm then moves the sampling window backward until the short-time average is again over 0.2 V. This is the approximate instant where the lubricant film has broken down. Then, the algorithm searches the maximum $\mathrm{d}v_{\mathrm{B}}/\mathrm{d}t$ in

the surrounding 100 samples. This point is defined as t_{EDM}, the exact instant where the lubricant film has broken down. If the mean voltage over the last 20 samples is above the threshold, no breakdown has occurred in this segment.

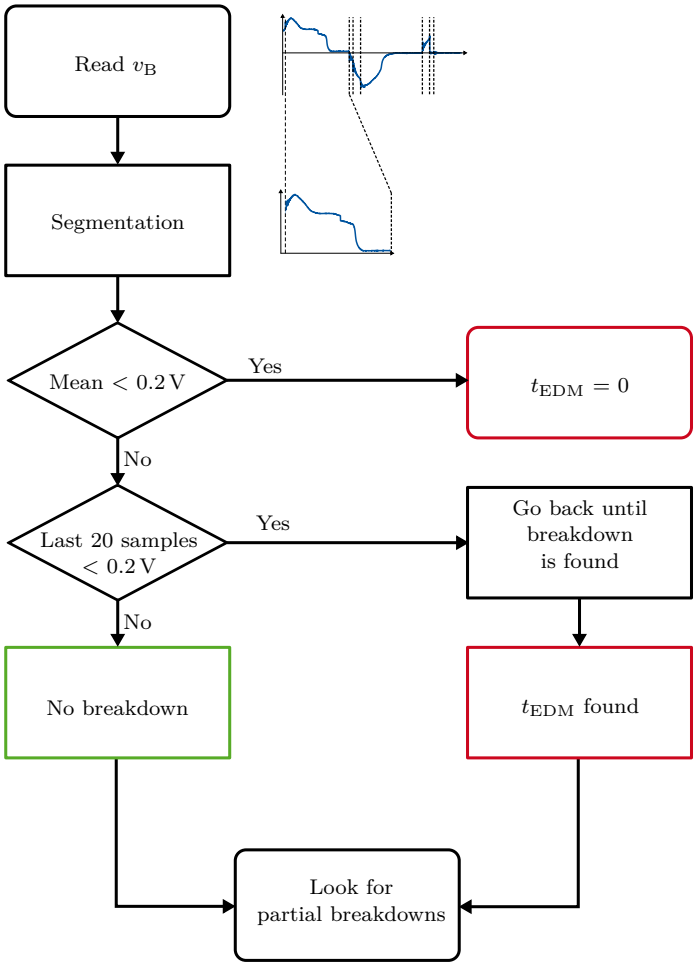

Figure 3.10: Algorithm for breakdown detection

While only one full breakdown can occur in one segment, multiple partial bearing voltage breakdowns may occur. Thus, when either no full breakdown has occurred in one segment, or the breakdown has not occurred directly at the beginning of the segment, the segment is scanned for additional partial breakdowns. Figure 3.11 shows the derivative of the bearing voltage $^{\mathrm{d}v_{\mathrm{B}}}/_{\mathrm{d}t}$ and the limits that are used for partial breakdown detection. The limits are the sum of the standard deviation of $^{\mathrm{d}v_{\mathrm{B}}}/_{\mathrm{d}t}$ and 10 % of the derivative of the CM voltage $^{\mathrm{d}v_{\mathrm{CM}}}/_{\mathrm{d}t}$ and 10 % of the derivative of the neutral point voltage $^{\mathrm{d}v_{\mathrm{N}}}/_{\mathrm{d}t}$. $^{\mathrm{d}v_{\mathrm{CM}}}/_{\mathrm{d}t}$ and $^{\mathrm{d}v_{\mathrm{N}}}/_{\mathrm{d}t}$ are included to avoid false positives near the switching instants. When a full breakdown has occurred within a segment, but not at the beginning, as is the case in segment one of the waveform shown in Figure 3.9, the algorithm searches for partial breakdowns between the beginning of the segment and the instant of the full breakdown t_{EDM}. Otherwise, it checks the full segment. At approximately 23 µs, $^{\mathrm{d}v_{\mathrm{B}}}/_{\mathrm{d}t}$ crosses the limits and a partial bearing breakdown is detected. The second crossing of the limit at 29 µs is the full breakdown. Both these events can also be seen in Figure 3.9.

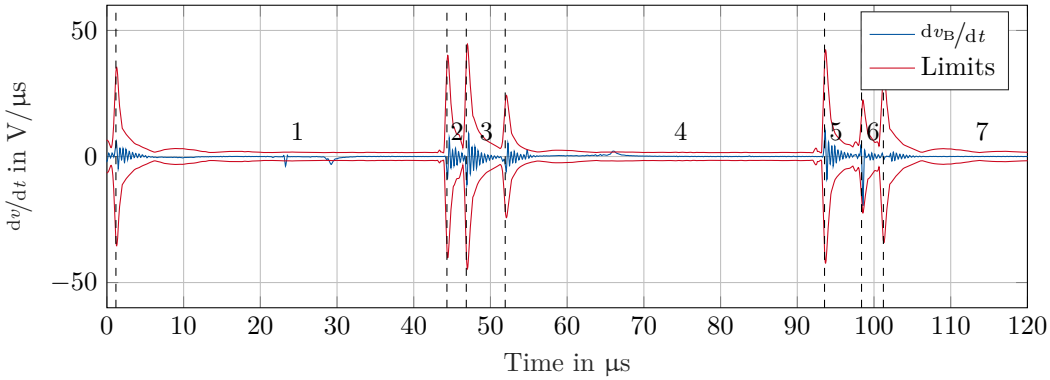

Figure 3.11: Shaft voltage derivative and limits for partial breakdown detection

The algorithm checks, if at any points in between the beginning of the segment and either the full breakdown or the end of the segment, $\mathrm{d}v_\mathrm{B}/\mathrm{d}t$ crosses the limits. When that is the case, the algorithm checks if the voltage amplitude is lower after the breakdown to remove false positives. When this condition is met as well, the algorithm has found a partial breakdown. Finally, it loops through all partial breakdown events and returns markers at the highest $\mathrm{d}v/\mathrm{d}t$ in their close proximity, thus returning the exact time instants of the partial breakdowns.

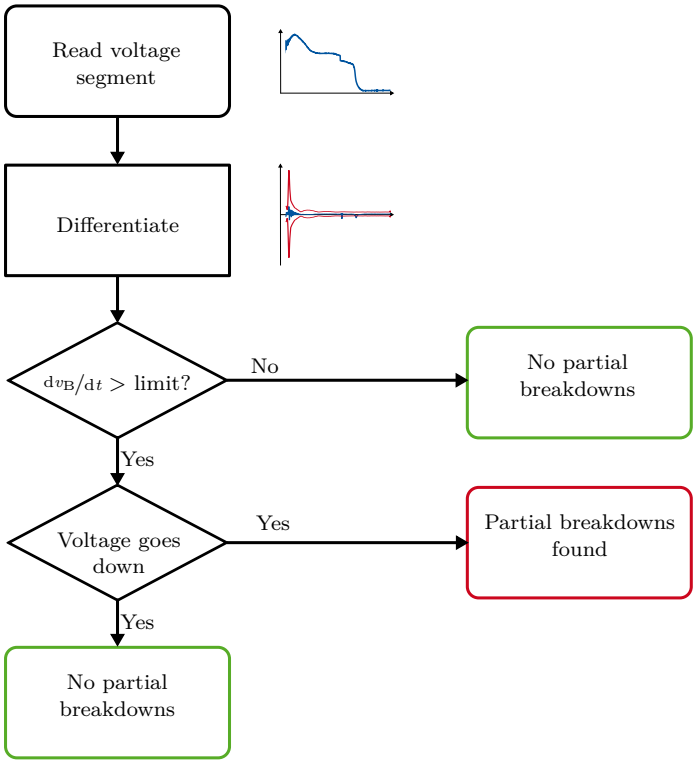

Figure 3.12: Algorithm for breakdown detection

3.5 Fault Detection from Axial Flux

Axial stray flux strongly disturbs the bearing current measurements conducted in this thesis. As already discussed in section 2.3, these disturbances can be suppressed using a high-pass filter. However, as demonstrated in [57], the axial flux can also be used for condition monitoring of a SCIM. Only the low-frequency part of the spectrum up to 2 kHz is needed for this. With the bearing current samples collected for the measurements in chapter 4 on the test bench presented in section 4.1, a frequency resolution of 5 Hz is achieved. While this resolution is far from optimal, it still allows the detection of some fault frequency components. Table 3.4 shows the expected fault frequencies for a bearing fault and a broken rotor bar calculated from equation (3.8) and equation (3.9) rounded to 5 Hz.

Table 3.4: Frequency components for an outer raceway fault and a BRB, rounded to 5 Hz

Fault Type	Frequency				
k	1	2	3	4	5
Outer raceway fault	130 Hz	210 Hz	290 Hz	370 Hz	450 Hz
BRB	25 Hz	50 Hz	75 Hz	100 Hz	125 Hz

Figure 3.13 shows the spectrum of the measured bearing current, i.e., the disturbances from axial stray flux. The spectrum from the healthy machine clearly shows the fundamental component at $f = 50\,\text{Hz}$ and the rotor slot harmonics at $f = 640\,\text{Hz}$. The spectrum from the machine with the bearing fault does not show any of the expected fault frequency components. In this measurement, the bearing fault can thus not be detected from the axial stray flux. The spectrum from the machine with the broken rotor bar, however, exhibits prominent peaks at the expected frequency components, proving that the disturbances from axial flux in the bearing current measurement can be used for fault detection.

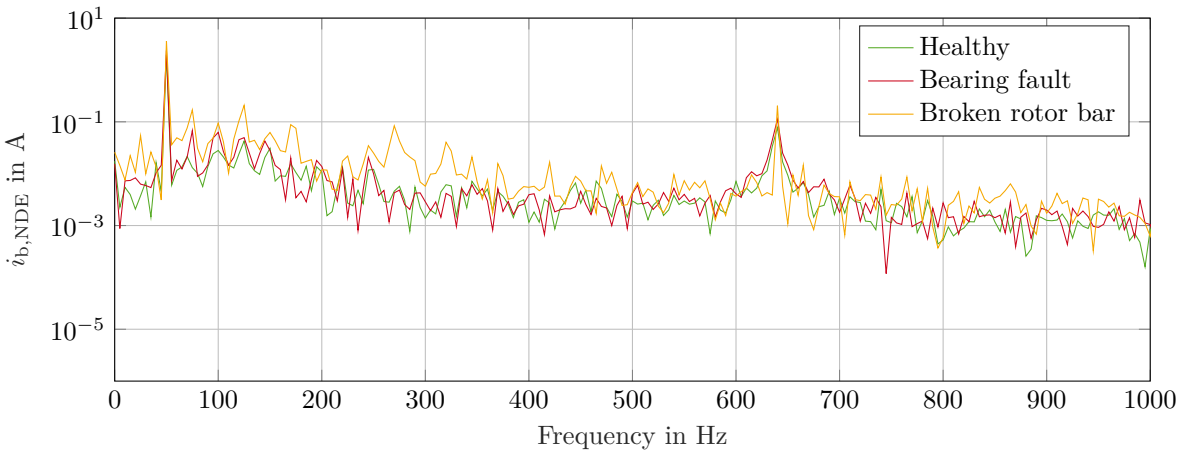

Figure 3.13: Low-frequency spectrum of the measured bearing current

3.6 Summary

This chapter has given an overview of the most common fault types in SCIMs. Then, three fault detection methods, namely MSCA, MSCSA and PCA have been introduced and their suitability for application in machines with varying operating points has been assessed. Especially at low load, their fault detection capability is lacking. To overcome these shortcomings, they have been combined with a k-NN algorithm and additional information about the operating point. Thus, a fault detection accuracy of 98.2 % and a fault classification accuracy of 97.4 % could be reached. Then, an algorithm for the automatic detection of EDM events and partial bearing voltage breakdowns from the bearing voltage was presented. Finally, it was shown that the axial stray flux that disturbs the bearing current measurements conducted in chapter 4 can be used for the detection of broken rotor bar faults.

4 Evaluation

In this chapter, parasitic effects in an electric machine are measured and evaluated. First, the measurement setup and the measurement conditions are presented. Then, an evaluation of the bearing voltage ratio (BVR), of electric discharge machining (EDM) events and of partial bearing breakdowns is conducted on a healthy machine. Finally, the same evaluation is conducted on two faulty machines, one with a bearing fault and one with a broken rotor bar, assessing the influence of these faults on the parasitic effects in an electric machine.

4.1 Measurement Setup

This section describes the main measurement setup used to validate the models, effects and fault detection methods described in the previous chapters. The setup consists of an inverter, a voltage source and an electric machine that is referred to as device under test (DUT) in this work. For this evaluation, no external load machine is connected to the DUT, i.e., it is operated under no-load condition. This way, it is guaranteed, that the shaft voltage and bearing current in the electric machine, are caused by the connected inverter and do not stem, e.g., from the inverter of a connected load machine.

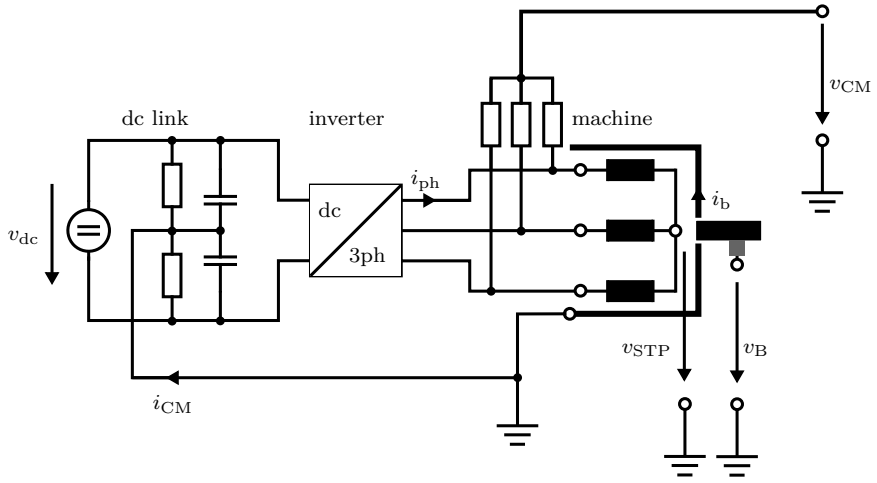

Figure 4.1: Equivalent of the setup for bearing voltage and current measurement

The measurement setup is shown in Figure 4.1, where the voltage source v_{dc} is located on the left. The dc link of the inverter is split and balanced passively with resistors. The

midpoint of the dc link is used as a reference potential for all measurements and is directly connected to the stator. A PWM generator that generates the switching pulses based on sine-triangle modulation controls the inverter. The current in one phase i_{ph} is measured with a Keysight N2783B current probe [99]. The common-mode (CM) current i_{CM}, the driven end (DE) bearing current $i_{\mathrm{b,DE}}$ and the non-driven end (NDE) bearing current $i_{\mathrm{b,NDE}}$ are measured with PMK UltraMiniHF Rogowski coils [61]. The shaft voltage is measured using a voltage probe with a carbon brush from Electro Static Technology [34]. A photo of the test bench is shown in Figure 4.2.

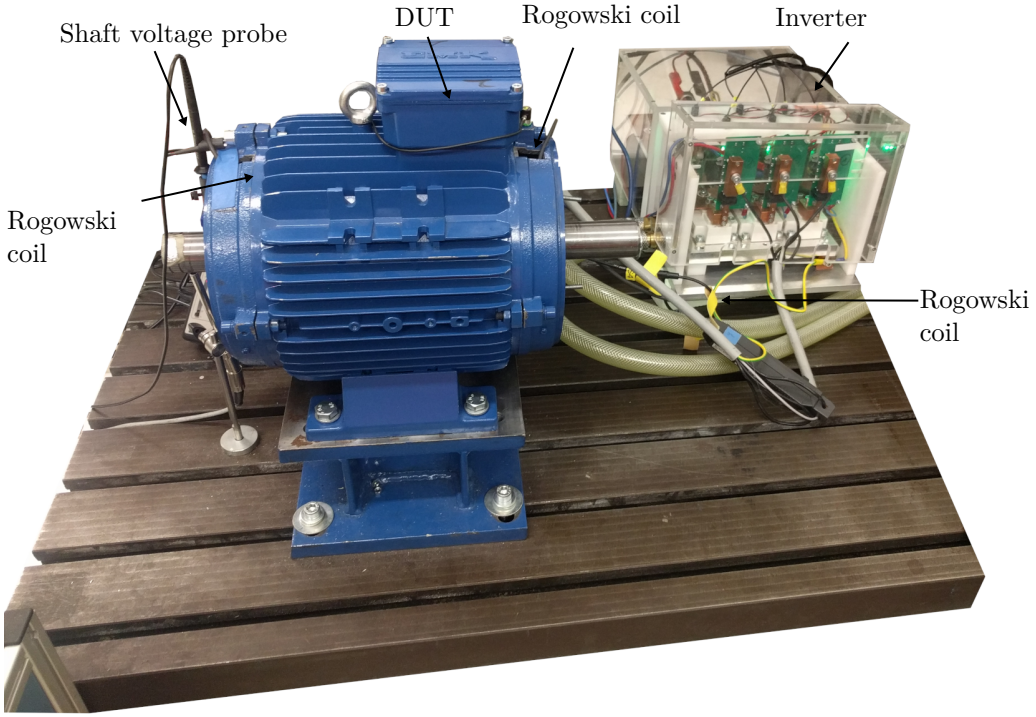

Figure 4.2: Test bench setup for the evaluation

Three different states-of-health are investigated: a healthy machine, a machine with a bearing fault and a machine with a broken rotor bar. Since the bearings are attached to the rotor, only the rotor of the machine is swapped while the stator remains the same. This is done to reduce the influence of parameter variations in the stator and to reduce errors caused by disconnecting and reconnecting the measurement devices. The only measurement devices that have to be reattached after exchanging the rotor are the Rogowski coils inside the machine and the shaft voltage measurement.

For each operating point and state-of-health, 35 consecutive measurements are conducted. Three of them have a duration of 200 ms, allowing to investigate long-term effects in the bearing currents and voltages and to analyze the spectra of i_{b}, i_{CM} and i_{ph} with a frequency resolution of 5 Hz. The other 32 measurements are short time measurements with a duration of 1 ms that allow investigating high-frequency effects more efficiently. As already discussed in section 2.3, the bearing current is subject to low-frequency disturbances that

likely stem from axial stray flux in the machine. To remove these disturbances, the bearing current is high-pass filtered with a corner frequency of 9 kHz. The filtered current is used for all analyses and waveforms shown in this chapter.

4.1.1 Measurement Conditions

The measurements in this chapter are conducted under a specific set of operating parameters in order to ensure comparability. The dc-link voltage is varied from 100 V to 400 V and the fundamental frequency of the voltage applied to the machine is varied from 5 Hz to 50 Hz, resulting in a no-load speed from 131 rpm to 1475 rpm. The switching frequency is constant at 10 kHz and the modulation index is varied so that the amplitude of the current flowing in the machine is similar for all investigated operating points. The modulation indices for the different operating points are given in Table 4.1.

Table 4.1: Modulation indices at the investigated operating points

Frequency	Speed	100 V	200 V	300 V	400 V
5 Hz	131 rpm	9 %	4.5 %	3 %	2.25 %
10 Hz	281 rpm	18 %	9 %	6 %	4.5 %
20 Hz	581 rpm	36 %	18 %	12 %	9 %
30 Hz	880 rpm	54 %	27 %	18 %	13.5 %
40 Hz	1173 rpm	72 %	36 %	24 %	18 %
50 Hz	1475 rpm	90 %	45 %	30 %	22.5 %

4.2 Investigations on a Healthy Machine

This section describes the investigations that are conducted on the healthy DUT. First, the bearing voltage ratio is calculated and analyzed in detail. Then, the occurrence EDM events and of partial bearing breakdowns is analyzed with respect to the operating point.

4.2.1 Bearing Voltage Ratio

In this section, BVR, i.e., the ratio of the CM voltage to the shaft voltage, is analyzed for the different investigated operating points of the healthy machine. It is calculated analogously to the approach shown in section 3.4 by dividing the voltage waveforms into segments between the switching events. When no breakdown has occurred in a segment, it is eligible for BVR calculation. Due to the capacitive coupling between CM voltage and

shaft voltage, the voltage of the previous segment has to be taken into account as well. The average BVR for segment i with the duration T_i is then calculated as follows:

$$\overline{\mathrm{BVR}}(i) = \frac{1}{T_i} \int \frac{v_\mathrm{B}(t) - \overline{v_\mathrm{B}}(i-1)}{v_\mathrm{CM}(t) - \overline{v_\mathrm{CM}}(i-1)} \mathrm{d}t \tag{4.1}$$

Quantities with a line over them are average quantities. The average BVR for one measurement is then calculated by weighting the average BVR for each segment with the segment length. As an example, the waveforms of the bearing voltage v_B and the CM voltage v_CM and the star point voltage v_STP scaled with the average BVR over all measurements are shown in Figure 4.3. Most of the time, the BVR is a good fit, but it is not suited for an exact calculation of the shaft voltage waveform. When multiplying the BVR with the neutral point voltage instead of the CM voltage, the waveform matches well and especially the steepness and the peak values are reproduced much better than when multiplying it with the CM voltage, as is usually done. An even more precise calculation of the bearing voltage can be achieved by multiplying the CM voltage and the star point voltage both with the BVR and a weighting factor. However, the exact distribution between v_CM and v_STP strongly depends on the winding configuration of the machine, therefore using the star point voltage as an estimate is a reasonable alternative requiring much less knowledge about the machine.

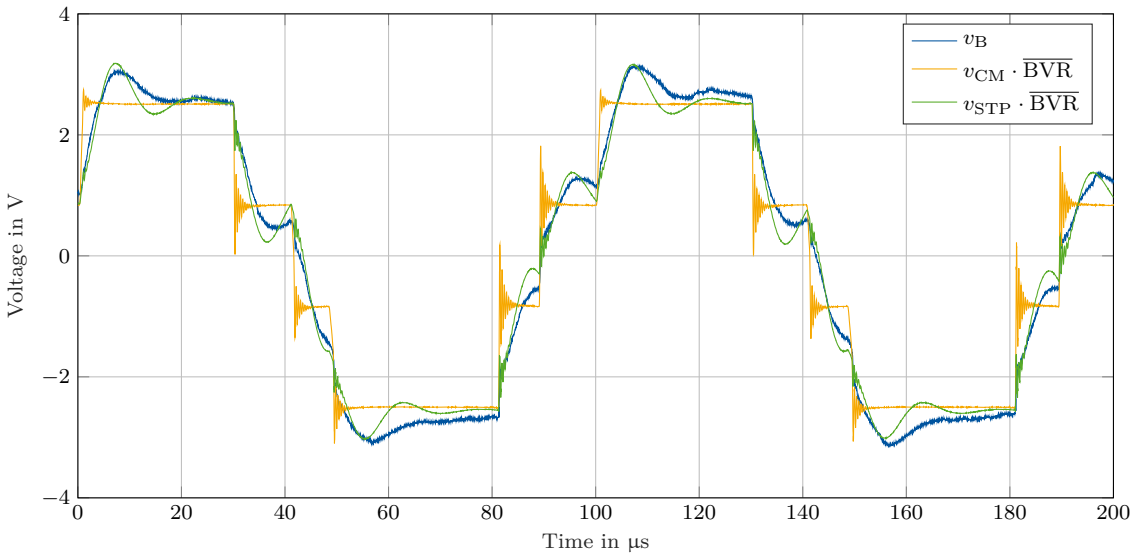

Figure 4.3: Shaft voltage and scaled CM voltage at 200 V and 1475 rpm

Figure 4.4 shows the average BVR for different rotor speeds and dc-link voltages. The average BVR for the healthy machine is 2.54 %. This value is also used in Figure 4.3. The reduced BVR at $V_\mathrm{DC} = 400\,\mathrm{V}$ over the whole speed range and at $\omega = 130\,\mathrm{rpm}$ over the whole dc-link voltage range is due to the high number of EDM events in these operating points.

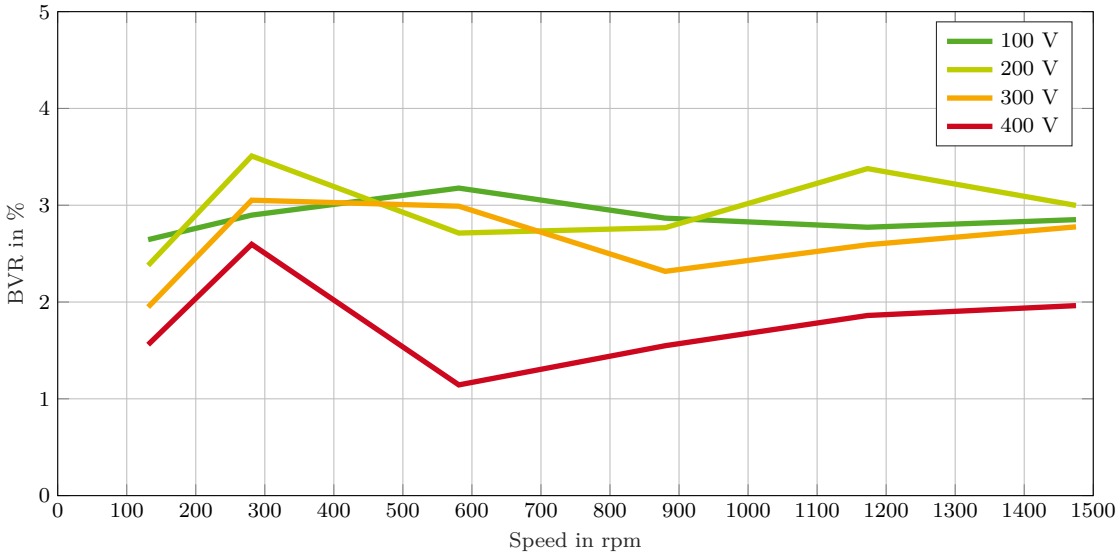

Figure 4.4: Average bearing voltage ratio for different speeds and voltages

Finally, Figure 4.5 shows the maximum bearing voltage for each investigated operating point of the healthy machine. The values that can be calculated by multiplying the maximum star point voltage with the average BVR of 2.54 % are marked with the dashed lines, where the colors correspond to the respective dc-link voltage. Note that it cannot necessarily be calculated directly from the BVR, since when a breakdowns occurs, an offset is added to the BVR (cf. equation (3.11)). This can lead to a lower ratio between maximum bearing voltage and maximum CM voltage, when breakdowns occur so early that the bearing voltage cannot fully build up. Alternatively, it can lead to a higher maximum voltage, e.g., when a breakdown occurs and v_B is negative and no breakdown occurs in the following segments where v_B and v_CM become positive. The dashed line in Figure 4.5 correspond to the maximum bearing voltage when no breakdowns occur. Due to the breakdowns in the bearing, the bearing voltage reaches values that are up to twice as high as can be expected from the BVR.

4.2.2 Electric Discharge Machining Events

EDM bearing currents can deteriorate the surface of a bearings raceway and rolling elements [100]. This section analyzes EDM events, i.e., full breakdown events in the bearings. Figure 4.6 shows voltage and current waveforms during an EDM event. At $t = 51.5\,\mu\mathrm{s}$, the bearing lubricant film breaks down and the bearing voltage v_B drops to nearly zero volts, as illustrated in Figure 4.6a. The DE and NDE bearing currents are shown in Figure 4.6b. The peak in $i_\mathrm{b,DE}$ is much higher than in $i_\mathrm{b,NDE}$, indicating that the EDM event occurred in the DE bearing. During the EDM event, a peak current of more than 200 mA flows. Together with the breakdown voltage of approximately 6.5 V, a bearing apparent power (BAP) of 1.3 VA is calculated. According to the investigations conducted in [20],

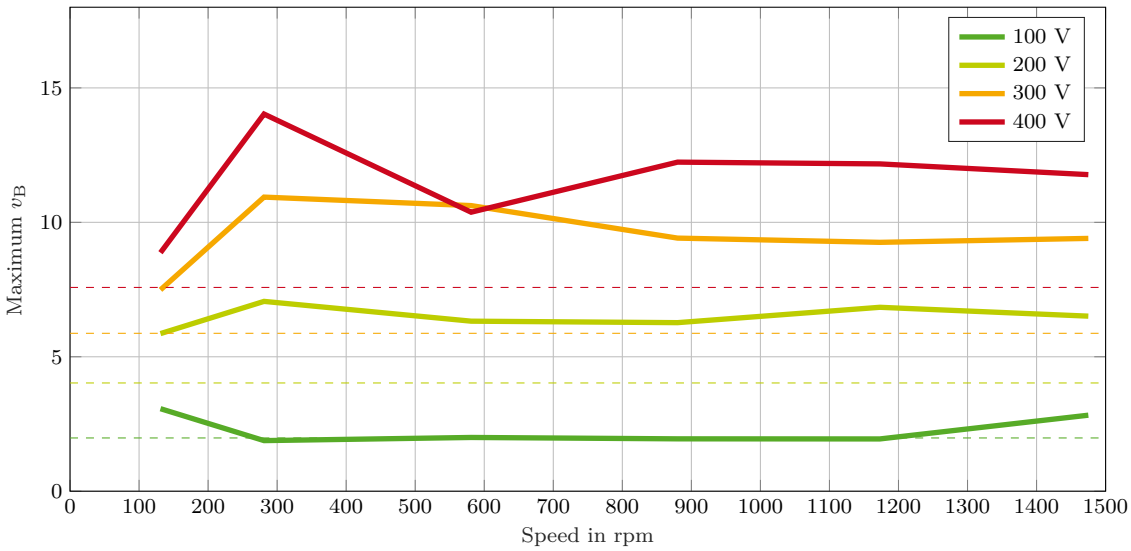

Figure 4.5: Maximum measured bearing voltage and expected value from the BVR

this is far from harmful for the bearing. Note that the waveforms shown in Figure 4.6 are recorded at the maximum dc-link voltage of 400 V, so the bearing voltage, and thus the BAP, is already higher than what can be expected for lower dc-link voltages.

In order to assess, whether EDM events inside a bearing can also be detected in the CM current, Figure 4.6c shows the CM current during the EDM event. The timescale is different from the previous waveforms to focus on the breakdown event itself and omit the switching events that can also be seen in Figure 4.6a and Figure 4.6b. This is necessary due to the high amplitude of the CM current during the switching events of up to 5 A. Nevertheless, there is no recognizable peak at the instant of the breakdown, which is marked with black dashed boxes in Figure 4.6. The CM current is also analyzed during other breakdown events but no recognizable current peaks can be found. One reason could be that the sensitivity of the Rogowski coil used to measure i_{CM} is too low. The silicon carbide (SiC) metal-oxide semiconductor field-effect transistors (MOSFETs) in the inverter achieve high voltage slopes up to 40 $^{\mathrm{V}}/_{\mathrm{ns}}$. Since the amplitude of the CM current is proportional to $^{\mathrm{d}v_{\mathrm{CM}}}/_{\mathrm{d}t}$ during switching, and the voltage slope is much steeper than in silicon (Si)-based inverters, i_{CM} is much higher here than in other publications using Si-based inverters [101]. The amplitude of the bearing current and the CM current during an EDM event, however, only depends on the machine characteristics and the bearing voltage. Thus, the signal-to-noise ratio might not be sufficient to capture both the peaks of the CM current and current peaks during breakdown events.

Figure 4.7 shows the number of EDM events per ms under different rotor speeds and dc-link voltages. The mean over three consecutive measurements, with a duration of 200 ms, each is shown. The distribution of the number of EDM events over the 32 shorter measurements is shown in the appendix in Figure A.8. The number of EDM events is relatively low at low dc-link voltages and only increases at a dc-link voltage of 400 V. The

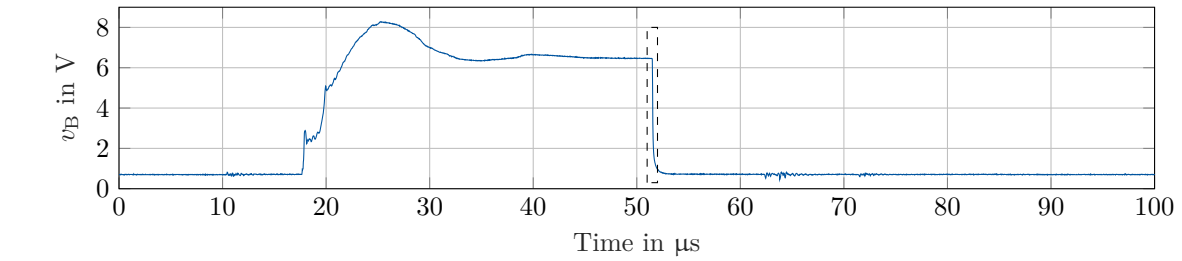

(a) Bearing voltage

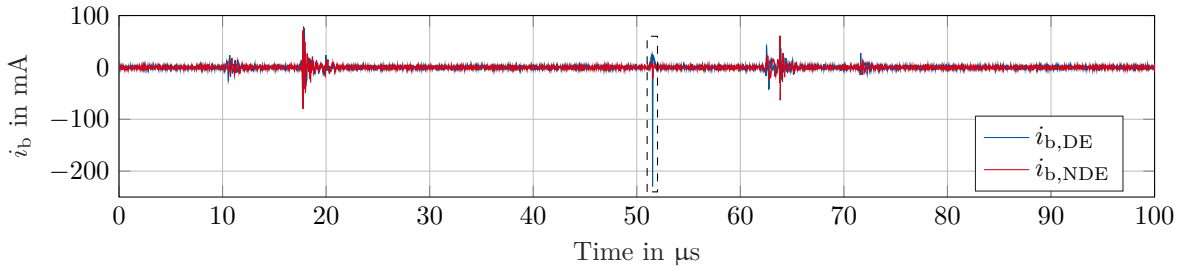

(b) Bearing current

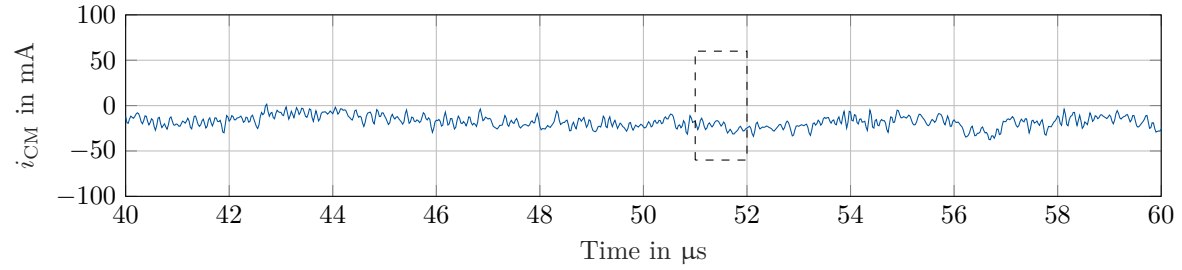

(c) CM current

Figure 4.6: Voltage and current waveforms during an EDM event

rated voltage of the machine is 400 V, but it is not specifically designed for operation with an inverter. At low rotor speed, the number of EDM events is high and above 600 rpm, it decreases below 10 $^1/_{ms}$. This is due to the low lubricant film thickness at low speed, as shown in Figure 2.4.

When looking at the amount of time spent in breakdown, shown in Figure 4.8, it is visible that with increasing speed, the time spent in breakdown is reduced. This correlates with the lubricant film thickness shown in Figure 2.4. At low speed, the lubricant film is thin and the maximum voltage it can withstand is thus low. At higher speed, it can withstand higher voltage, since its thickness increases. From 100 V to 300 V dc-link voltage, no clear increase in breakdowns is visible. At 400 V dc-link voltage however, the amount of time spent in breakdown is increased. This means that the bearing breaks down more often or earlier in the switching period.

Figure 4.9a shows the distribution of the breakdown voltage over all recorded EDM events. Note that EDM events that occur at the beginning of a switching segment and where

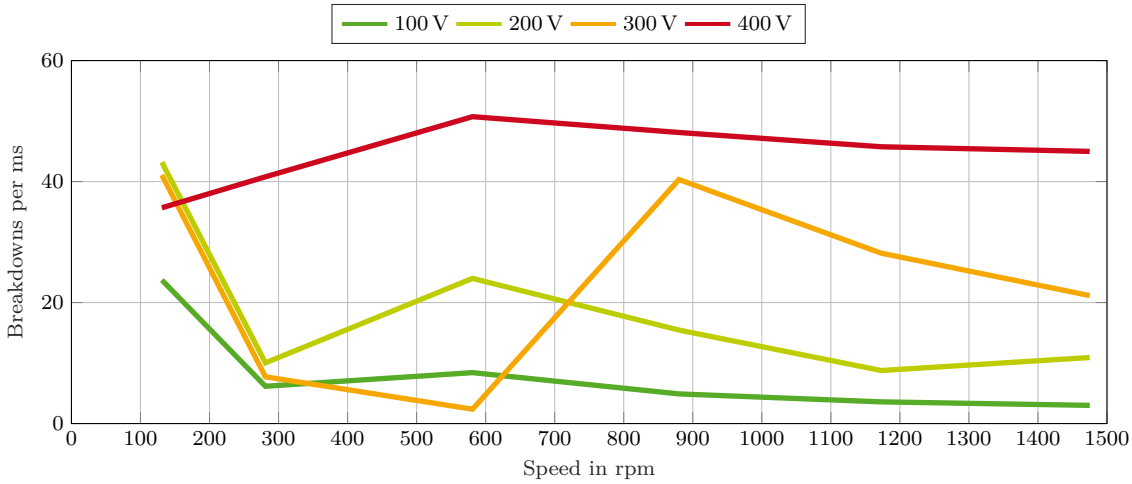

Figure 4.7: Number of EDM events per ms for different dc-link voltages and speeds

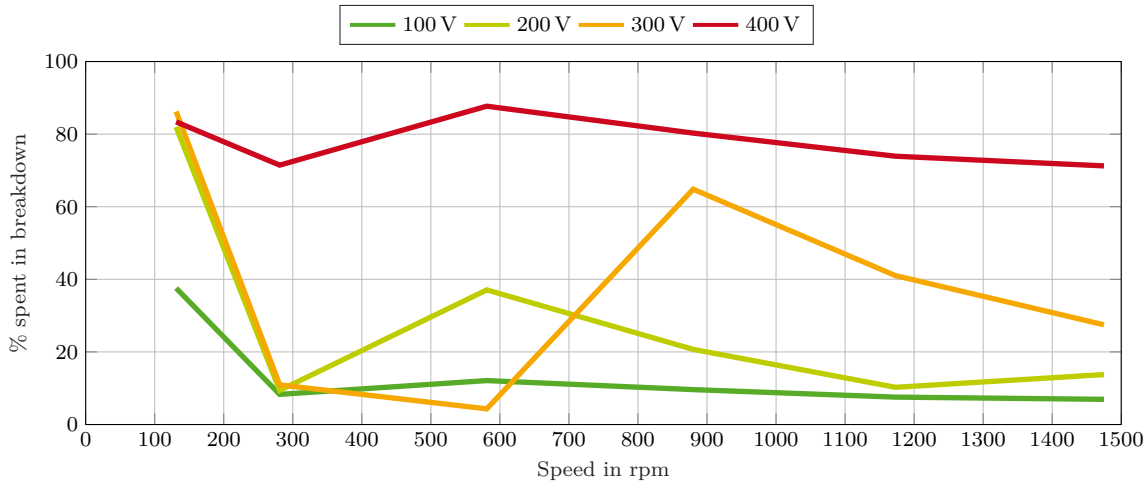

Figure 4.8: Percentage of time spent in breakdown for different dc-link voltages and speeds

a breakdown has already occurred in the previous segment are excluded here. Since this applies to more than 80 % of all EDM events and the breakdown voltage is zero in that case, including these EDM events would inhibit the clarity of Figure 4.9a. The highest recorded breakdown voltage is 11.4 V, but most breakdowns occur at a much lower voltage.

The BAP is introduced in [20] as a simple indicator on how harmful an EDM event (or any current passing through a bearing) is for the bearing. Figure 4.9b shows the distribution of the BAP over all EDM events. Most breakdown events are below a BAP of 0.2 VA and even the most severe EDM that occurs over the course of all measurements in the healthy machine do not surpass 5.8 VA. Since the limit, above which EDM events reduce the lifetime of a bearing is 20 VA, it can be concluded that even though many EDM events occur, they do not harm the bearing and are not detrimental to the lifetime of the DUT.

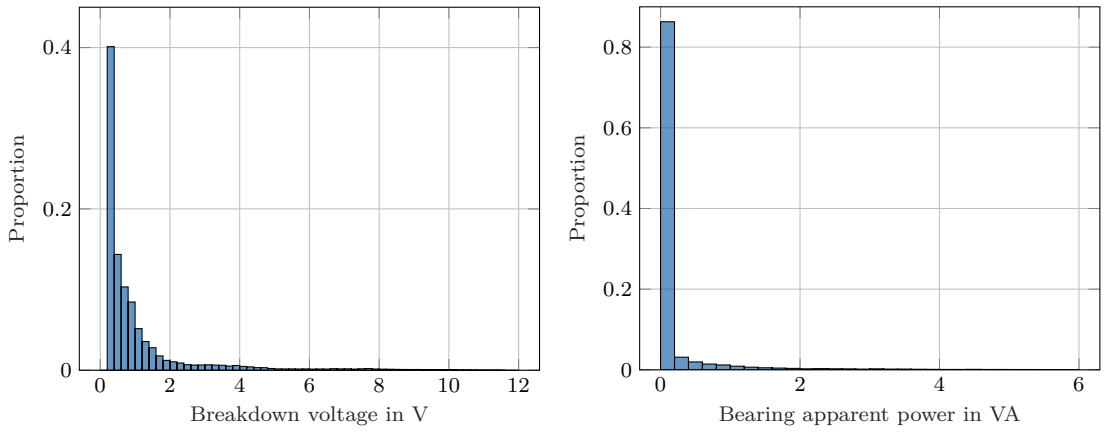

(a) Breakdown voltage (b) BAP

Figure 4.9: Distribution of breakdown voltage and BAP over all recorded EDM events

The BAP [20], similar to the apparent bearing current density [6], are both strongly influenced by the peak value of the bearing current. As already discussed in section 2.1.4, the total energy that is dissipated in the bearing in the case of an EDM event mostly depends on the bearing voltage. Assuming that the electrical time constant of the bearing discharge is much smaller than the thermal time constant of the bearing, the breakdown energy directly correlates with the temperature that the material reaches at the instant of the EDM event. Since the bearing capacitance can vary by more than 50 %, as shown in section 2.2.8, depending on the ratio between the rotor-to-stator capacitance C_{RS} an the bearing capacitance C_{B}, the amount of energy dissipated in an EDM event can also vary significantly. Especially in small machines with a larger air gap, such as the DUT, the ratio between C_{RS} and C_{B} can be small. In integrated e-axles, however, interior permanent magnet machines are often used. Since they require a small air gap to achieve high reluctance torque, C_{RS} will be relatively high when compared to C_{B}. The variation of C_{B} will thus have little influence on the bearing voltage and on the BAP.

4.2.3 Partial Bearing Breakdowns

As already shown in Figure 3.9, besides the full breakdowns that occur in the measurements and that have been investigated in several publications (among others [13], [100]), partial breakdowns can occur. In a partial breakdown, the voltage does not fully break down to zero but is only reduced. Figure 4.10 shows such a partial breakdown event.

In Figure 4.10, both a partial breakdown and an EDM event, meaning a full breakdown, occur. At $t_{\mathrm{PB}} = 24.1\,\mu\mathrm{s}$, the bearing voltage shown in Figure 4.10a drops from 7.6 V to 6.5 V, before dropping to nearly zero at $t_{\mathrm{EDM}} = 27.3\,\mu\mathrm{s}$. The bearing current is shown in Figure 4.10b. Both during the partial breakdown and during the full breakdown, a current peak can be observed. The current in the partial breakdown is much lower than

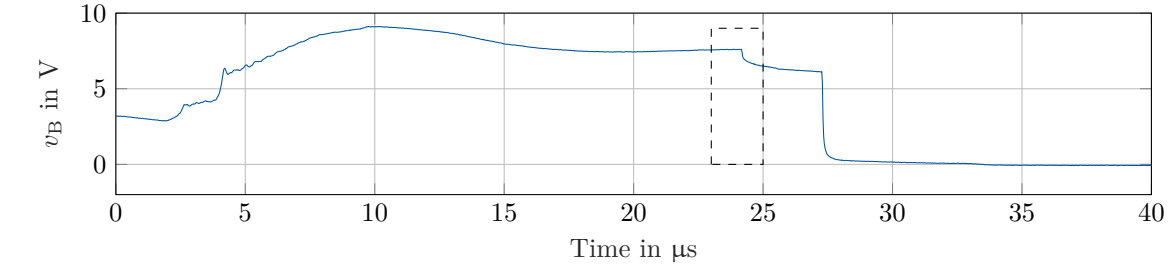

(a) Bearing voltage

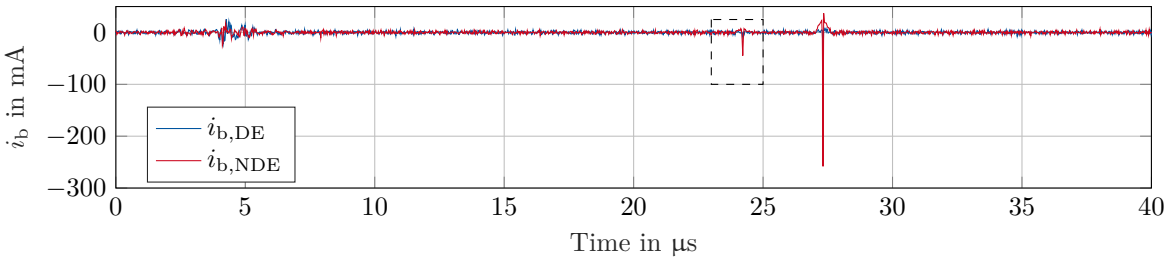

(b) Bearing current

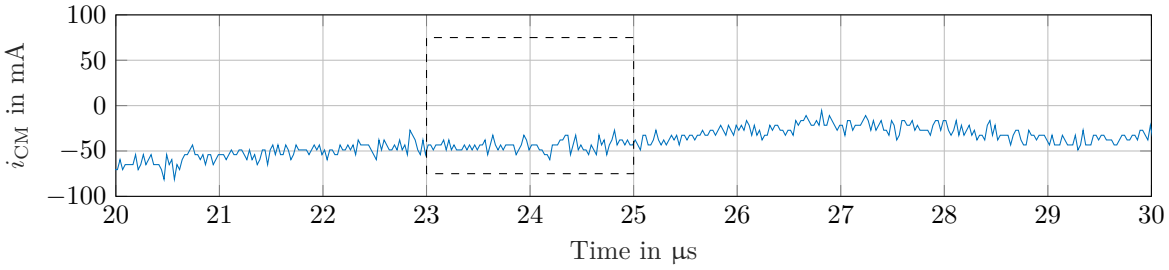

(c) CM current

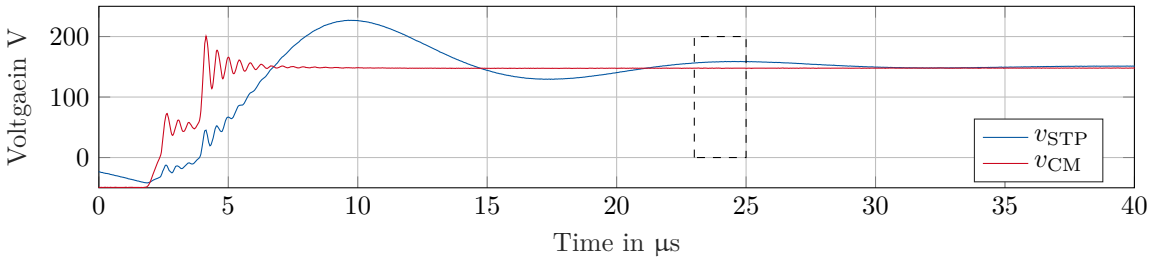

(d) CM and star point voltage

Figure 4.10: Voltage and current waveforms during a partial breakdown followed by a full breakdown

the current during the EDM event, but is still larger than the capacitive bearing current during switching at $t_{sw} = 4\,\mu s$. Figure 4.10c shows the CM current. The time scale is again adapted, so that the focus is on the partial breakdown and the EDM event and the switching event is omitted. Similarly to Figure 4.6c, no impact of the partial breakdown or the EDM event can be seen. Finally, Figure 4.10d shows the star point and the CM voltage. Here, no voltage drop can be observed at t_{PB}, proving that the measured partial

breakdown is not simply a voltage drop in v_{CM} or v_{STP} that is capacitively coupled to v_{B}.

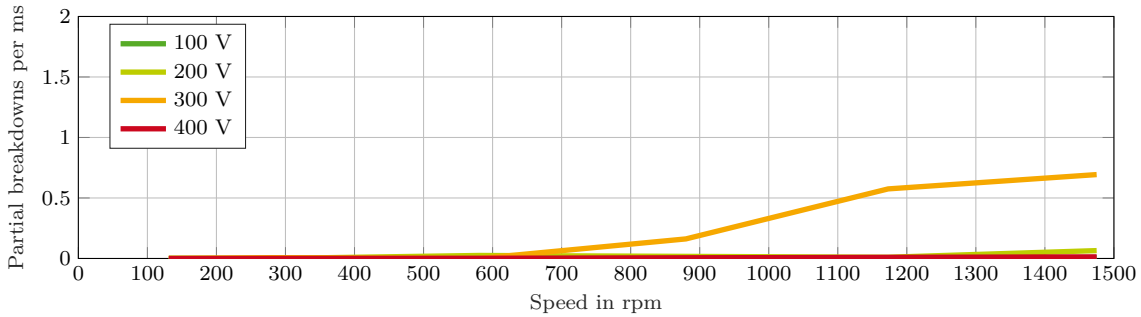

Figure 4.11: Number of partial breakdowns per ms for different dc-link voltages

Next, the influence of the dc-link voltage and the rotor speed on the occurrence of partial breakdowns is investigated. Figure 4.11 shows the number of partial breakdowns per ms. When compared to Figure 4.7, it can be seen that partial bearing breakdowns are much rarer than full breakdowns. In the conducted measurements, they occur most often at a dc-link voltage of 300 V and at higher rotor speeds.

Figure 4.12a shows the distribution of the voltage drop over all recorded partial breakdown events. Most partial breakdowns lead to a voltage drop between 0.6 V and 0.8 V. The lower number of recorded partial breakdowns with a lower voltage drop can be due to the fact that their detection is more difficult since a lower voltage drop usually goes hand in hand with a lower $\mathrm{d}v_{\mathrm{B}}/\mathrm{d}t$ (cf. section 3.4).

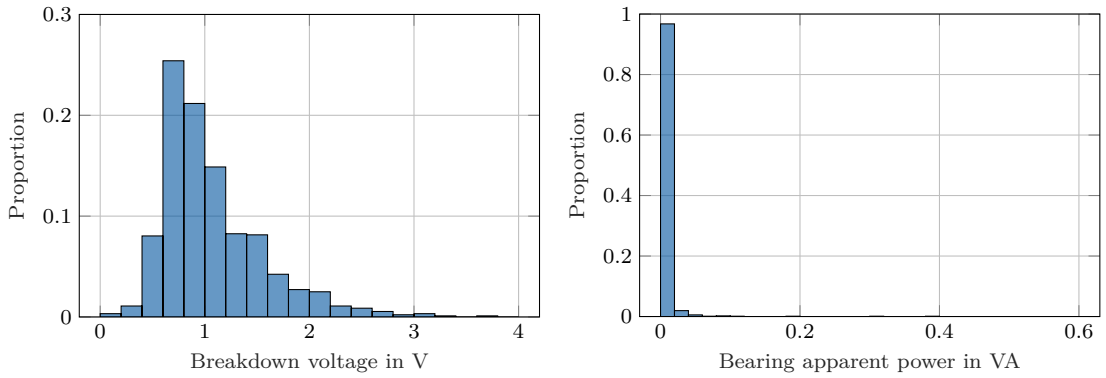

(a) Breakdown voltage

(b) BAP

Figure 4.12: Distribution of breakdown voltage and BAP over all recorded partial bearing breakdowns

Finally, Figure 4.12b shows the distribution of the BAP over all recorded partial breakdown events. As already expected from the BAP of the EDM events, the BAP of the partial bearing breakdowns is far below the limit of 20 VA and, thus, not harmful for the bearing.

One possible explanation for the partial breakdown event could be that the carbon brush that is used to measure the shaft voltage is not always perfectly connected to the shaft. When a switching event occurs, the probe voltage and the bearing voltage would then drift apart. However, since the probe capacitance would form a capacitive voltage divider with the coupling capacitance between shaft and probe, as illustrated in Figure 4.13, the measured voltage would have to be lower than the actual shaft voltage. When contact is restored the absolute value of the measured voltage would thus increase to match the actual bearing voltage. Thus, an unstable contact between probe and shaft could only explain a voltage step that increases the amplitude and not a partial breakdown event as illustrated in Figure 4.10.

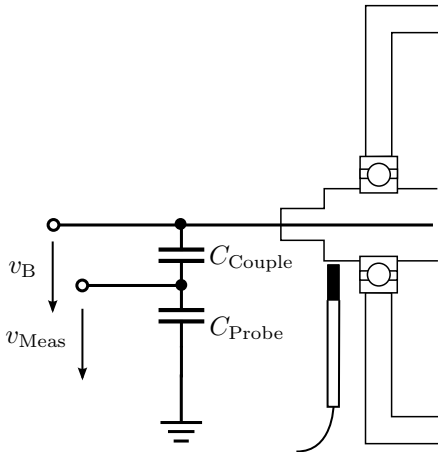

Figure 4.13: Capacitive coupling of an unconnected probe

A second possible explanation stems from the distributed bearing model shown in Figure 2.13. When only the lubricant film between one of the raceways and a bearing ball breaks down (e.g. the capacitance between a bearing ball and the inner raceway $C_{\mathrm{B,I}}$) and the voltage over the other parasitic capacitance (in this case the capacitance between the bearing ball and the outer raceway $C_{\mathrm{B,O}}$) is not large enough for it to break down, only a part of the bearing capacitance is discharged. The voltage drop can be estimated from the dissipated energy. It strongly depends not only on the capacitance that has broken down, but also on the surrounding capacitances (namely the rotor-to-stator capacitance C_{RS} and the winding-to-rotor capacitance C_{WR}). Usually, C_{RS} is larger than the bearing capacitance C_{B} and therefore also much larger than $C_{\mathrm{B,I}}$. Assuming $C_{\mathrm{B,I}} = C_{\mathrm{B,O}}$, the energy that is dissipated in the partial breakdown is equal to

$$E_{\mathrm{PB}} = \frac{1}{2} \cdot (\frac{v_{\mathrm{B}}}{2})^2 \cdot C_{\mathrm{B,I}}. \tag{4.2}$$

The energy stored in the surrounding capacitances is equal to

$$E_{\mathrm{total}} = \frac{1}{2}\Big({v_{\mathrm{B}}}^2 \cdot (2C_{\mathrm{B}} + C_{\mathrm{RS}}) + (v_{\mathrm{CM}} - v_{\mathrm{B}})^2 C_{\mathrm{WR}}\Big). \tag{4.3}$$

Substituting v_{CM} from equation (2.8) leads to

$$
\begin{aligned}
E_{\text{total}} &= \frac{1}{2}\left({v_{\text{B}}}^2 \cdot (2C_{\text{B}} + C_{\text{RS}}) + \left(\frac{2C_{\text{B}} + C_{\text{RS}} + C_{\text{WR}}}{C_{\text{WR}}} v_{\text{B}} - v_{\text{B}} \right)^2 C_{\text{WR}} \right) \\
&= \frac{{v_{\text{B}}}^2}{2}\left(2C_{\text{B}} + C_{\text{RS}} + C_{\text{WR}} \cdot \left(\frac{2C_{\text{B}} + C_{\text{RS}} + C_{\text{WR}} - C_{\text{WR}}}{C_{\text{WR}}} \right) \right) \\
&= {v_{\text{B}}}^2 \left(2C_{\text{B}} + C_{\text{RS}}\right). \qquad (4.4)
\end{aligned}
$$

To estimate the range of the voltage drop due to the partial breakdown, two scenarios are compared. A bearing with eight rolling elements is analyzed. It is assumed that the bearing capacitance only consists of the ball-to-raceway capacitances. In scenario one that is unfavorable for a high voltage drop, the ball-to-raceway capacitances are distributed evenly, i.e., $C_{\text{B,I}i} = C_{\text{B,O}i} = {C_{\text{B}}}/{4}$. Furthermore, C_{RS} is assumed to be ten times larger than C_{B} [6]. The relative difference between the bearing voltage before the partial breakdown and after the partial breakdown $\Delta_{\text{Rel}} v_{\text{B}}$ can be calculated from the difference in energy stored in the parasitic capacitances as

$$
\begin{aligned}
\Delta_{\text{Rel}} v_{\text{B}} &= 1 - \sqrt{\frac{E_{\text{total}} - E_{\text{PB}}}{E_{\text{total}}}} = 1 - \sqrt{\frac{2C_{\text{B}} + C_{\text{RS}} - {C_{\text{B,I}}}/{4}}{2C_{\text{B}} + C_{\text{RS}}}} \\
&= 1 - \sqrt{\frac{2C_{\text{B}} + 10C_{\text{B}} - {C_{\text{B}}}/{16}}{2C_{\text{B}} + 10C_{\text{B}}}} = 0.26\,\%. \qquad (4.5)
\end{aligned}
$$

Under these unfavorable conditions, the voltage drop is below 36 mV, assuming that the partial breakdown occurs at the maximum recorded bearing voltage of 14 V. In scenario two that is favorable for a high voltage drop, it is assumed that the ball-to-raceway capacitances are distributed unevenly. The capacitance, in which the breakdown occurs, is seven times as high as the other ball-to-raceway capacitances. The relation between C_{B} and $C_{\text{B,I}}$ can then be calculated as

$$
C_{\text{B}} = \frac{7C_{\text{B,I}}}{2} + \frac{C_{\text{B,I,max}}}{2} = C_{\text{B,I,max}}. \qquad (4.6)
$$

Additionally, C_{RS} is assumed equal to C_B. The relative voltage difference is then calculated as

$$\begin{aligned}\Delta_{Rel} v_B &= 1 - \sqrt{\frac{E_{total} - E_{PB}}{E_{total}}} = 1 - \sqrt{\frac{2C_B + C_{RS} - {}^{C_{B,I}}/_{4}}{2C_B + C_{RS}}} \\ &= 1 - \sqrt{\frac{2C_B + C_B - {}^{C_B}/_{4}}{2C_B + C_B}} = 4.3\,\%. \end{aligned} \tag{4.7}$$

Even though the conditions are chosen favorably for a large bearing voltage drop in scenario two, with large, very unevenly distributed bearing capacitances and a small C_{RS}, the calculated voltage drop is still below 5 %. Even at the maximum recorded bearing voltage of 12.9 V, this leads to a bearing voltage drop of 0.6 V. However, Figure 4.12a shows that 65 % of partial breakdown events exhibit an even larger voltage drop. Even when assuming that all rolling elements in one bearing are electrically connected via the cage, the calculated maximum voltage drop only increases to approximately 1.1 V, still leaving approximately 30 % of partial breakdowns unaccounted for.

For a third possible explanation, the behavior of the partial breakdowns is analyzed in more detail. For this part, only the measurements at $\omega_m = 1475$ rpm are considered. The maximum ${}^{dv}/_{dt}$ of the EDM events analyzed in the previous section and of the partial breakdowns is plotted in Figure 4.14 over the initial voltage before the breakdown $v_B(t < t_{break})$, over the voltage level after the breakdown $v_B(t > t_{break})$ and over the voltage drop during the breakdown Δv_B, to assess with which of these variables it correlates the most.

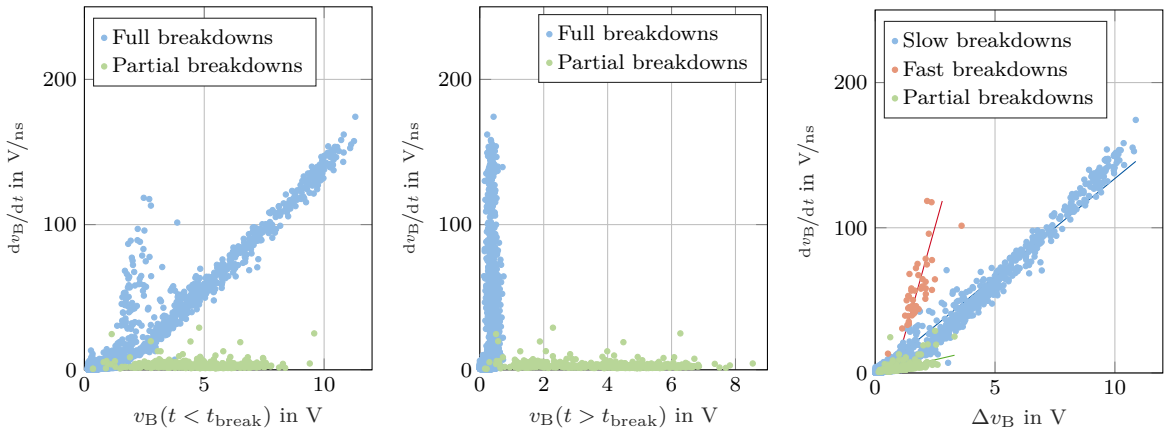

(a) Voltage before breakdown (b) Voltage after breakdown (c) Voltage difference

Figure 4.14: ${}^{dv_B}/_{dt}$ over voltage before breakdown, after breakdown and voltage difference

Figure 4.14a shows ${}^{dv_B}/_{dt}$ over the bearing voltage before the breakdown. The EDM events are marked in blue and the partial breakdowns are marked in green. Three overall trends

can be recognized. While partial breakdowns occur at nearly all voltage levels, they exhibit much lower maximum voltage slopes than full breakdowns. Furthermore, there seem to be two categories of full breakdowns. For the bulk of the breakdowns, $^{\mathrm{d}v_\mathrm{B}}/_{\mathrm{d}t}$ is proportional to the bearing voltage at the instant of the breakdown $v_\mathrm{B}(t < t_\mathrm{break})$. Additionally, high-$^{\mathrm{d}v}/_{\mathrm{d}t}$ breakdowns with low initial voltage appear in the left side of Figure 4.14a.

Figure 4.14b shows $^{\mathrm{d}v_\mathrm{B}}/_{\mathrm{d}t}$ over the bearing voltage after the breakdown. Naturally, all full breakdowns are located on the left side of Figure 4.14b, since the voltage after a full breakdown is low. Partial breakdowns are located again at the bottom of the figure, and no clear correlation between $^{\mathrm{d}v_\mathrm{B}}/_{\mathrm{d}t}$ and the voltage level, at which the partial breakdown settles, is recognizable.

Finally, Figure 4.14c shows $^{\mathrm{d}v_\mathrm{B}}/_{\mathrm{d}t}$ over the breakdown voltage drop, i.e., the difference between the voltage before and after the breakdown. For the full breakdowns, this is similar to Figure 4.14a, since the voltage after the breakdown is low and therefore $\Delta v_\mathrm{B} \approx v_\mathrm{B}(t < t_\mathrm{break})$. For partial breakdowns, however, now a clear correlation between voltage slope and voltage drop can be recognized. The least-square-fits show the average value in the respective parts of the scatter plot. The voltage slope during a partial breakdown thus correlates with the difference in voltage before and after the partial breakdown. Breakdowns that are located on one straight line from the origin have the same time constant τ when modeling the voltage waveform of the breakdown as

$$v_\mathrm{B}(t) = v_\mathrm{B}(t > t_\mathrm{break}) + \Delta v_\mathrm{B} \cdot e^{\frac{t}{\tau}} \tag{4.8}$$

Assuming that the bearing capacitance is the same for all measurements at one speed, this means that the breakdown resistance is lower for full breakdowns than it is for partial breakdowns. Furthermore, the strong correlation between Δv_B and $^{\mathrm{d}v_\mathrm{B}}/_{\mathrm{d}t}$ suggests that the voltage level, at which the breakdown settles is already fixed when the breakdown starts. Thus, partial breakdowns are not full breakdowns that are interrupted by, e.g., mechanical separation or a breakdown current that falls below a certain limit and extinguishes, e.g., due to the high pressure in the lubricant as suggested in [102] for transformer oil.

The average time constant of the breakdowns, i.e., the steepness of the balance lines in Figure 4.14c, is given in Table 4.2. The fast breakdowns colored in red occur during switching events, when the bearing was already in breakdown during the previous switching segment. They are always considerably faster than the slow breakdowns, which constitute the bulk of the breakdown events. Partial breakdown events, on the other hand, are around three to four times slower. Under the assumption that the bearing capacitance is the same for all breakdown events at one specific speed, this suggests that the breakdown resistance is three to four times larger in partial breakdowns than in full breakdowns.

The partial breakdown settling voltage, i.e., the voltage level after a partial breakdown, reaches values of up to 6 V. Until this point, no satisfactory explanation for this could be found. The correlation between Δv_B and $^{\mathrm{d}v_\mathrm{B}}/_{\mathrm{d}t}$ suggests that a partial discharge of the

Table 4.2: Average breakdown time constant for different rotor speeds ω_m

ω_m	Partial breakdowns	Slow breakdowns	Fast breakdowns
131 rpm	25.5 µs	14.5 µs	-
281 rpm	29.3 µs	16.4 µs	4.6 µs
581 rpm	37.3 µs	12.3 µs	2.7 µs
880 rpm	55.4 µs	13.6 µs	5.4 µs
1173 rpm	42.9 µs	13.9 µs	3.6 µs
1475 rpm	59.1 µs	13.5 µs	3.8 µs

bearing capacitances is the reason. Higher voltage drops could be caused by a connection of the bearing balls via the cage during a partial breakdown or subsequent partial breakdowns.

4.3 Influence of Bearing Faults in Electric Machines on Parasitic Effects

In this section, the influence a bearing fault on the parasitic effects investigated in section 4.2 is analyzed. To this end, the measurements from section 4.2 are repeated with a machine with a point defect in the outer raceway of the NDE bearing. To facilitate the comparison with the measurements from the healthy machine, the results from the healthy machine and the faulty machine are plotted next to each other. The BVR and the occurrence of EDM events and partial bearing breakdowns are analyzed for the DUT with a point defect in the outer raceway and compared to the results from the healthy machine.

4.3.1 Bearing Voltage Ratio

The average BVR for different dc-link voltages and rotor speeds is shown in Figure 4.15. The BVR is again calculated according to equation (4.1). At 131 rpm, the BVR cannot be calculated, since, due to the high number of breakdowns, no switching segment without breakdowns can be found for the BVR calculation. At higher speeds, the BVR increases and is close to the average value from the measurement conducted in section 4.2. The average BVR for 281 rpm and above is 2.35 %, which is slightly below the value for the healthy machine.

In Figure 4.16, the maximum bearing voltage for each investigated operating point of the machine with the bearing fault is shown. The expected maximum voltage values that

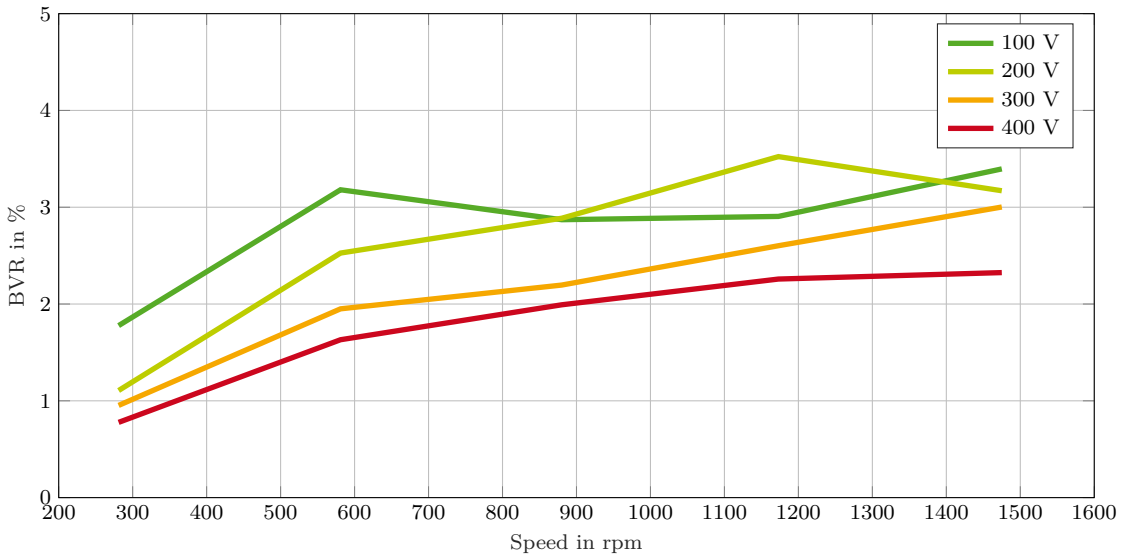

Figure 4.15: Average bearing voltage ratio for different speeds and voltages for the DUT with a bearing fault

can be calculated by multiplying the maximum star point voltage with the average BVR of 2.35 % are marked with the dashed lines, the colors correspond to the respective dc-link voltage. Similar to Figure 4.5, the difference between the actual maximum voltage and the expected value from the BVR is due to the voltage offset from the EDM events.

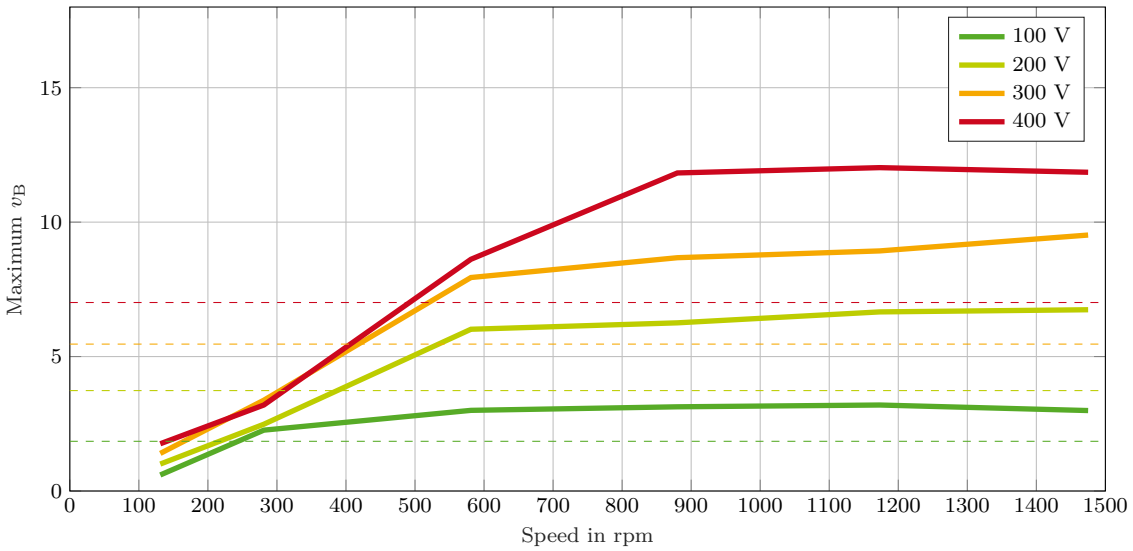

Figure 4.16: Maximum measured bearing voltage and expected value from the BVR

4.3.2 Electric Discharge Machining Events

Figure 4.17 shows the number of EDM events per ms under different speeds and dc-link voltages. In Figure 4.17a, the measurements with a healthy machine from section 4.2.2 are shown again for comparison. In Figure 4.17b, the same measurements are conducted with a machine with a point defect in the outer raceway of one bearing. The amount of breakdowns that occur is increased in most operating points. The difference is more notable at lower speeds for a dc-link voltage of 100 V and 200 V. For 300 V and 400 V, the amount of breakdowns is increased over the whole speed range. Two effects can explain this. On one hand, the point defect in the bearing leads to increased bearing losses, and thus, to an increase in bearing temperature. As shown in section 2.2.8, higher temperatures lead to a reduced lubricant film thickness, and thus, the voltage at which the lubricant film breaks down is reduced. On the other hand, when a ball passes the point defect, it will receive an impulse in radial direction, affecting the lubricant film thickness and maybe even leading to metallic contact between the inner and outer raceway. Since the bearing temperature is not measured, it cannot be determined with absolute certainty which of these effects is dominant. However, since the machine is not operated continuously for more than one minute, it can be assumed that the bearing temperature does not increase significantly. Therefore, it is assumed that the bearing balls experience more movement in radial direction in the faulty bearing, causing an increase in the number of breakdowns.

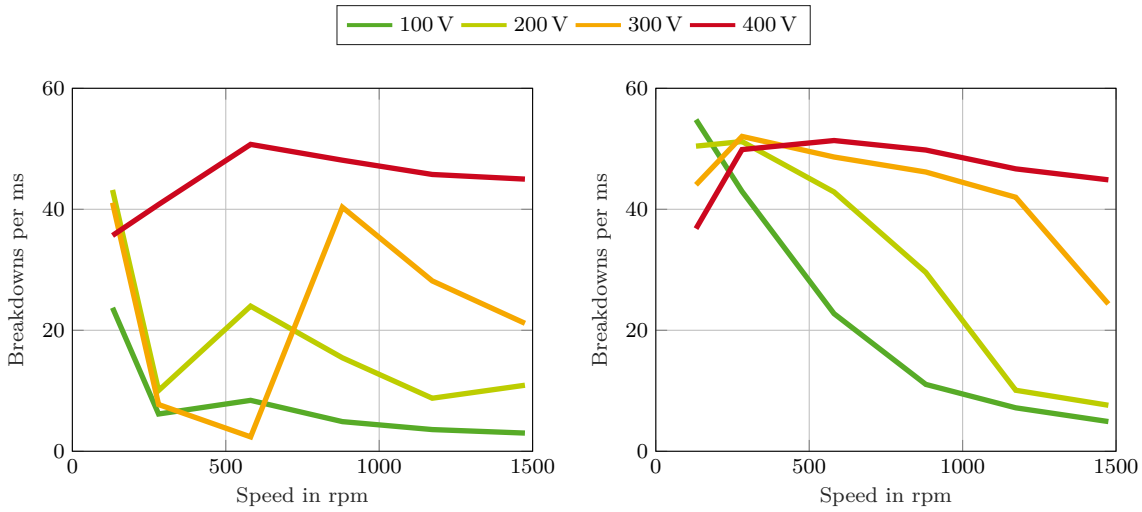

(a) Healthy bearing

(b) Faulty bearing

Figure 4.17: Number of EDM events per ms for different dc-link voltages and rotor speeds

The amount of time spent in breakdown shown in Figure 4.18 is increased comparison to the healthy case. At 131 rpm, the bearing is in breakdown most of the time. This explains why the BVR cannot be calculated for the low-speed operating points. Only at low dc-link voltages, i.e., 100 V and 200 V, and speeds above 900 rpm, the breakdown behavior is

similar for both the healthy and the broken machine. At a dc-link voltage of 300 V, the faulty bearing breaks down more often and earlier compared to the healthy bearing. At 400 V, the time spent in breakdown is slightly reduced. However, Figure 4.17b shows that more breakdowns occur, meaning that the EDM events occur on average slightly later in the switching period, which reduces the time spent in breakdown.

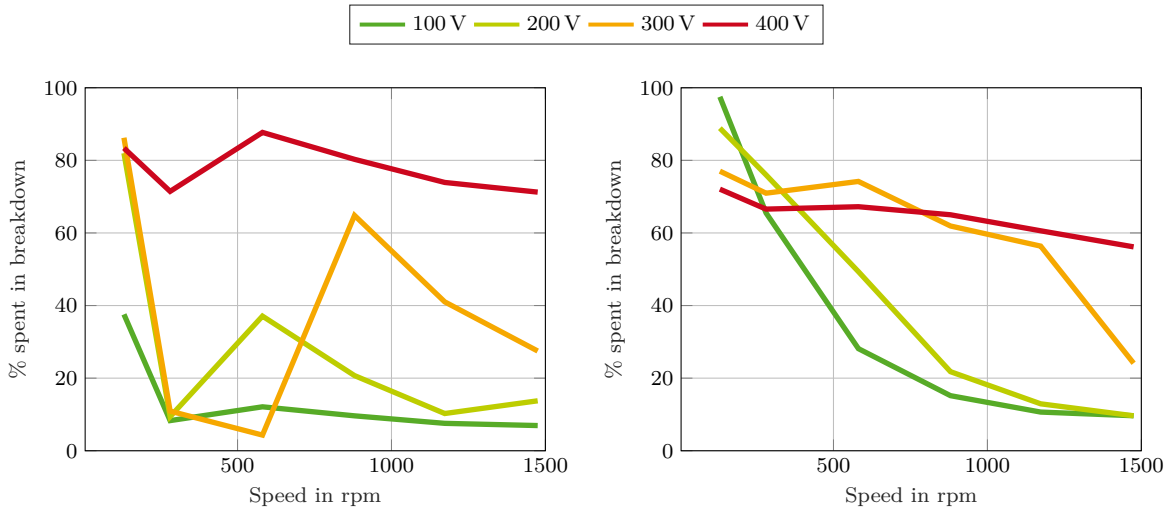

(a) Healthy bearing (b) Faulty bearing

Figure 4.18: Percentage of time spent in breakdown for different dc-link voltages rotor and speeds

Finally, Figure 4.19 shows, in which bearing the EDM events occur. In the healthy machine, they are distributed relatively evenly between the DE and NDE bearings. In the machine with the bearing fault, however, more EDM events occur in the faulty bearing (NDE) than in the healthy bearing (DE).

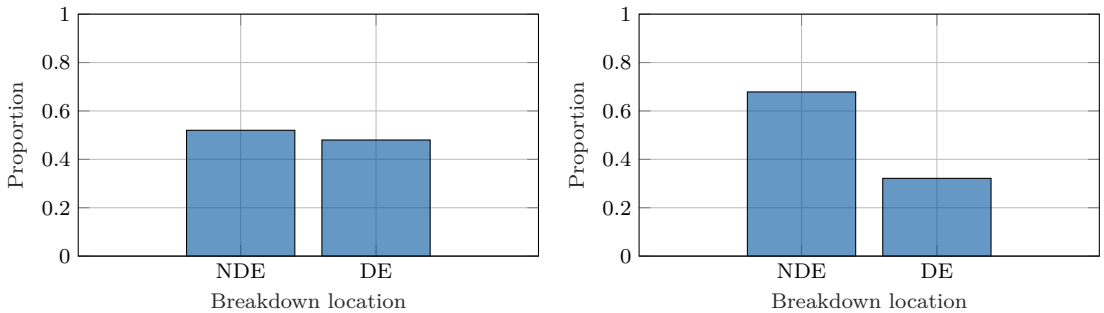

(a) Both bearings healthy (b) Faulty bearing in NDE

Figure 4.19: Breakdown location in a healthy and fault bearing

To summarize, this section has shown that in a machine with a bearing fault, EDM events occur more often compared to a healthy machine. Especially at low rotor speeds, where

the lubricant film it thin, the faulty bearing is in breakdown most of the time. While the EDM events are distributed evenly between both bearings in a healthy machine, in the faulty machine, more breakdowns occur in the faulty bearing. Since EDM events can also be one root cause of bearing faults, this shows a self-reinforcing effect, i.e., EDM events cause bearing faults, which in turn cause more EDM events, damaging the bearing even more.

4.3.3 Partial Bearing Breakdowns

Next, the occurrence of partial breakdowns in the healthy and the faulty machine is compared. Figure 4.20 shows the number of partial breakdowns per ms in the healthy and the faulty machine. In both machines, the partial breakdowns mostly occur at a dc-link voltage of 300 V and at high rotor speed. The differences are relatively small and

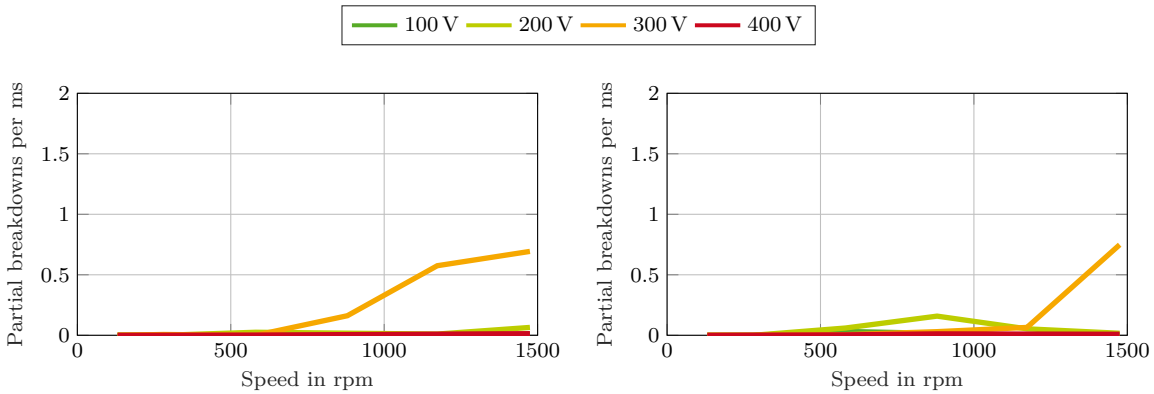

(a) Healthy bearing (b) Faulty bearing

Figure 4.20: Number of partial breakdowns per ms for different dc-link voltages

due to the low overall number of partial breakdowns, no statistically relevant assertion can be made here.

Figure 4.21b shows the distribution of the partial breakdown voltage, i.e., the difference in voltage before and after the breakdown, over all recorded partial breakdown events in the machine with the bearing fault. The distribution is slightly shifted towards higher breakdown voltages.

Next, Figure 4.22b shows the distribution of the bearing apparent power. As already expected from the measurements from the healthy machine, the values are far away from the critical thresholds and pose thus no danger to the bearings of the machine.

Finally, Figure 4.19 shows, in which bearing the partial breakdowns occur. In the healthy machine, they are distributed relatively evenly between the DE and NDE bearings. In

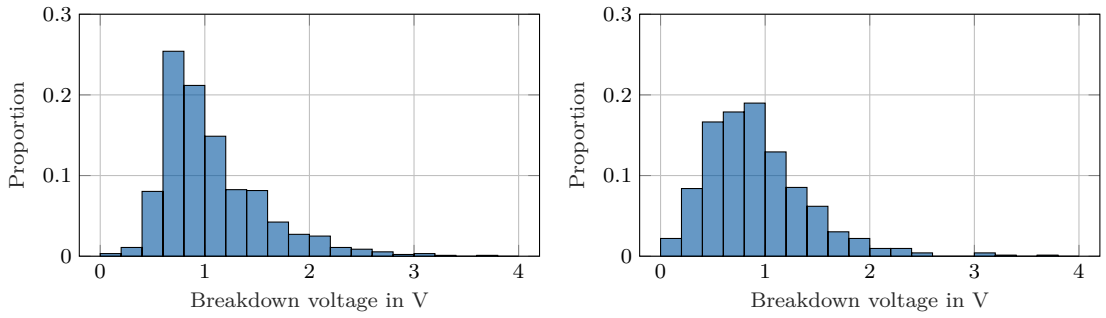

(a) Healthy bearing (b) Faulty bearing

Figure 4.21: Distribution of breakdown voltage over all recorded partial bearing breakdowns in the machine with the faulty bearing

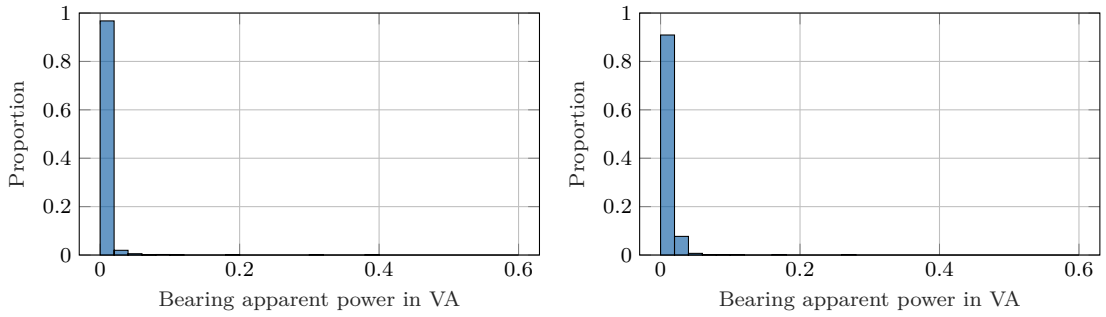

(a) Healthy bearing (b) Faulty bearing

Figure 4.22: Distribution of BAP over all recorded partial bearing breakdowns in the machine with the faulty bearing

the machine with the bearing fault, however, more partial breakdowns occur in the faulty bearing (NDE) than in the healthy bearing (DE).

The point defect in the bearing thus leads to a slight increase in EDM events, and thus, a slightly lower average BVR. The maximum bearing voltages are similar to those in the healthy machine. The number of EDM events increases especially in low-speed operating points, where the lubricant film is thin and metallic contact between the bearing balls and raceways is thus more likely. No increase in the number of partial breakdown events can be seen, but the distribution of both EDM events and partial breakdowns between the bearings shifts slightly towards the damaged bearing in the faulty machine.

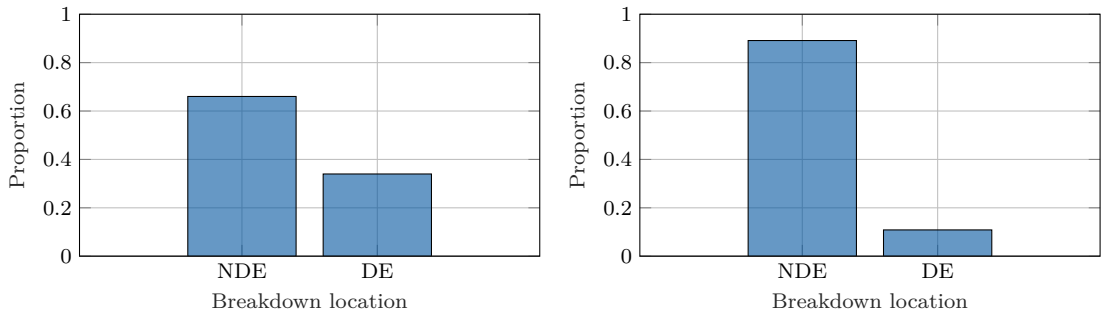

(a) Both bearings healthy

(b) Faulty bearing in NDE

Figure 4.23: Partial breakdown location in a healthy and fault bearing

4.4 Influence of Broken Rotor Bars in Electric Machines on Parasitic Effects

In this section, the influence a broken rotor bar on the parasitic effects investigated, in section 4.2, is analyzed. To this end, the measurements from section 4.2 and section 4.3 are repeated with a machine with a broken rotor bar. To facilitate the comparison with the measurements from the healthy machine, the results from the healthy machine and the faulty machine concerning EDM events and partial bearing breakdowns are again plotted next to each other.

4.4.1 Bearing Voltage Ratio

The average BVR for different dc-link voltages and rotor speeds in the machine with a bearing fault is shown in Figure 4.24.

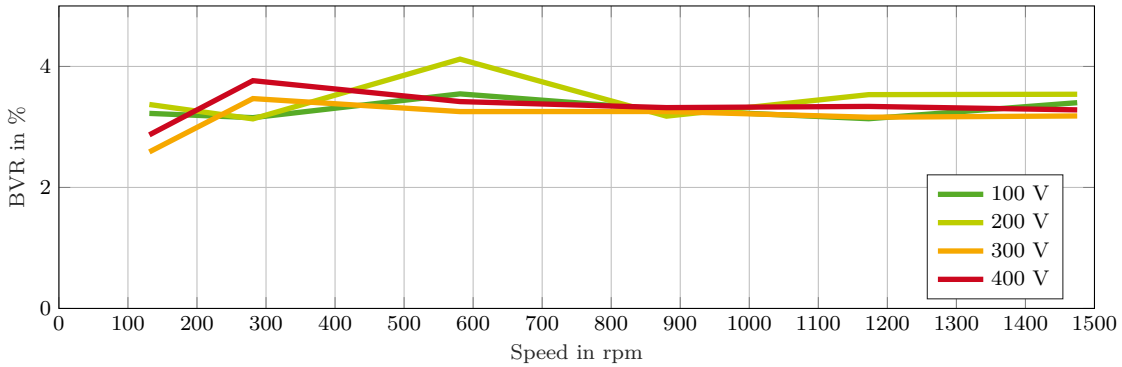

Figure 4.24: Average bearing voltage ratio for different speeds and voltages for the DUT with a broken rotor bar

The BVR is again calculated according to equation (4.1). The BVR is much more constant between the different operating points when compared to the measurements on the healthy machine in Figure 4.4 or the measurements on the machine with the faulty bearing in Figure 4.15. At higher speeds, the BVR increases and is close to the average value from the measurement conducted in section 4.2. The average BVR above is 3.31 %, which is much higher than the value for both the healthy machine and the machine with the bearing fault. Different effects can cause this. The winding-to-rotor capacitance C_{WR} has the largest influence on the BVR. Since the same stator was used for all measurements, one possible explanation could be that the broken rotor is slightly smaller than the rotor in the healthy machine, e.g., due to manufacturing inaccuracies. For the rotor-to-stator capacitance C_{RS}, an increase in air-gap length from 500 µm to 550 µm leads to a reduction in capacitance by 10 %. For the winding-to-rotor capacitance C_{WR}, this reduction can be assumed to be lower since the distance between the winding and the rotor is larger than the distance between rotor and stator. Assuming that C_{RS} is at least ten times larger than C_{WR} [6], [44], the BVR would thus increase. Another possible explanation is that the bearings that are used in the faulty machine either have a larger radial clearance or are lubricated with a different lubricant, leading to a larger lubricant film thickness and thus a reduced bearing capacitance.

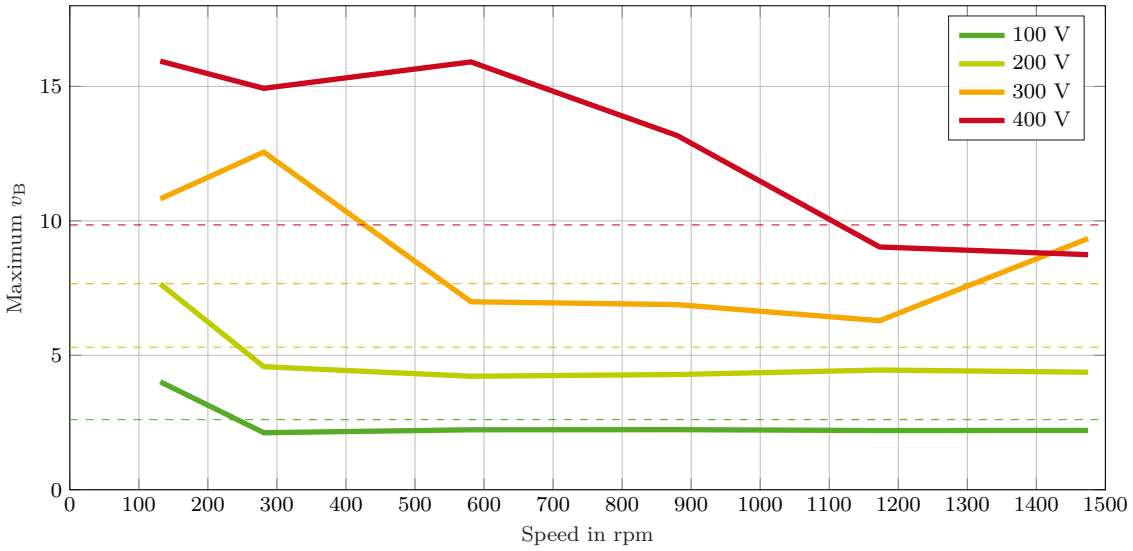

Figure 4.25: Maximum measured bearing voltage and expected value from the BVR in a machine with a broken rotor bar

In Figure 4.25, the maximum bearing voltage for each investigated operating point of the machine with the broken rotor bar is shown. The values that can be calculated by multiplying the maximum star point voltage with the average BVR of 3.31 % are marked with the dashed lines; the colors correspond to the respective dc-link voltage. The maximum bearing voltage is only significantly higher than expected at low speed and high dc-link voltage. This indicates that at high speeds, or low dc-link voltages, the number of EDM events is low and, thus, no large offsets are added to the bearing voltage.

4.4.2 Electric Discharge Machining Events

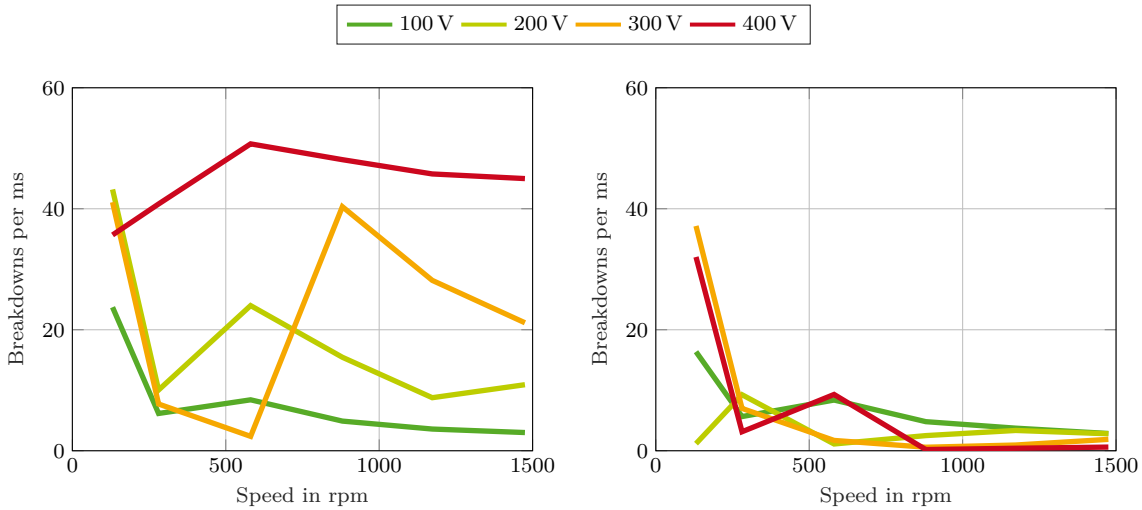

(a) Healthy rotor

(b) Broken rotor bar

Figure 4.26: Number of EDM events per ms for different dc-link voltages

Figure 4.26 shows the number of EDM events per ms under different speeds and dc-link voltages. In Figure 4.26a, the measurements with a healthy machine from section 4.2.2 are once more shown for comparison and in Figure 4.26b, the same measurements are conducted with a machine broken rotor bar. The amount of breakdowns that occur is reduced in almost all operating points. On average, in the faulty machine, the number of EDM events is more than 50 % lower than in the healthy machine. Together with the higher average BVR and the higher shaft voltage, this indicates that even though the bearings in the different machines should be of the same type, since they were purchased from the same manufacturer and have the same model number, different types of bearings have been used in the two machines.

The amount of time spent in breakdown shown in Figure 4.27b is also reduced in comparison to the healthy case. At 131 rpm, and high dc-link voltages, the bearing is still in breakdown most of the time. At speeds above 131 rpm or dc-link voltages below 300 V, the bearing is in breakdown less than 12 % of the time.

Finally, Figure 4.28 shows, in which bearing the EDM events occur. In the healthy machine, they are distributed relatively evenly between the DE and NDE bearings. In the machine with the broken rotor bar, however, more EDM events occur in the DE bearing than in the NDE bearing.

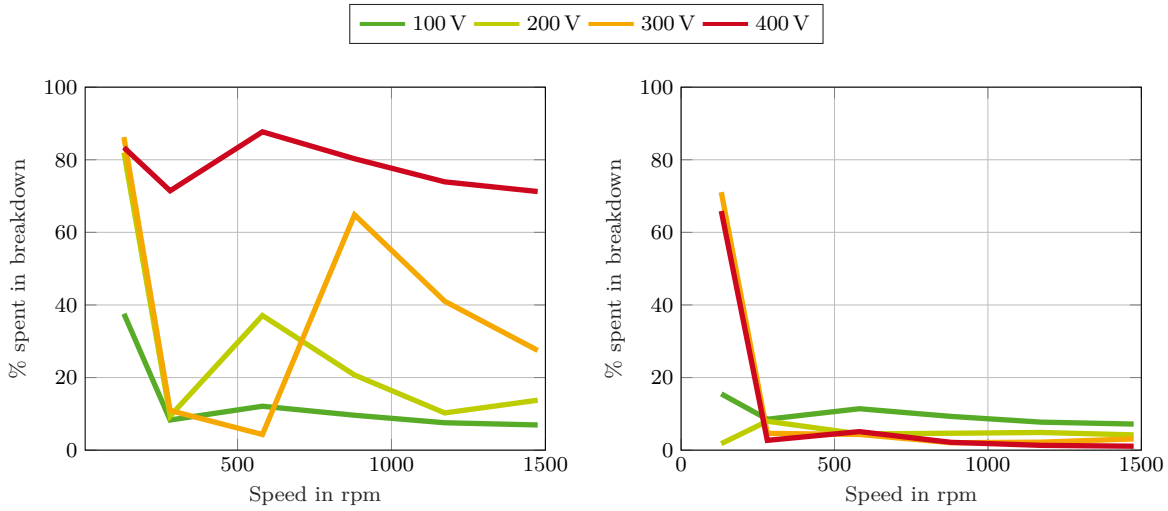

(a) Healthy rotor (b) Broken rotor bar

Figure 4.27: Percentage of time spent in breakdown for different dc-link voltages and speeds

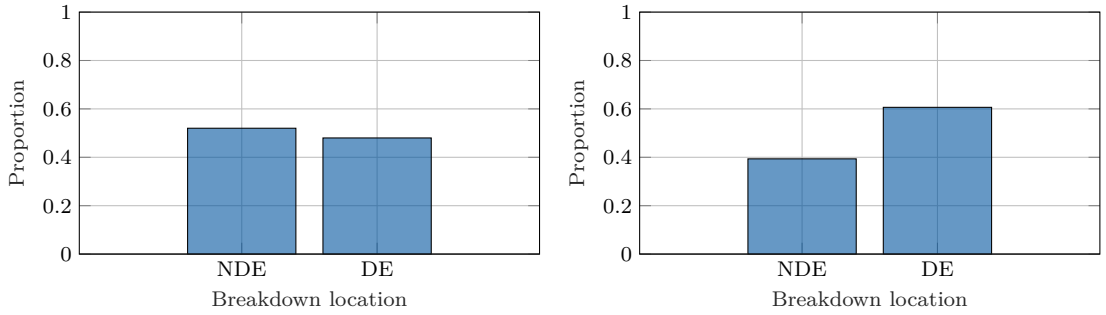

(a) Healthy machine (b) Broken rotor bar NDE

Figure 4.28: Breakdown location in a healthy and fault bearing

4.4.3 Partial Bearing Breakdowns

In the following, the occurrence of partial breakdowns in the healthy machine and in the machine with the broken rotor bar is compared. Figure 4.29 shows the number of partial breakdowns per ms in the healthy and the faulty machine. In the machine with the broken rotor bar, nearly no partial bearing breakdowns can be observed.

In Figure 4.30, the distribution of the partial breakdown voltage, i.e., the difference in voltage before and after the breakdown, in the healthy and the faulty machine is compared. The distribution is slightly shifted towards lower breakdown voltages. However, due to the low overall number of partial breakdown, a comparison is not reasonable.

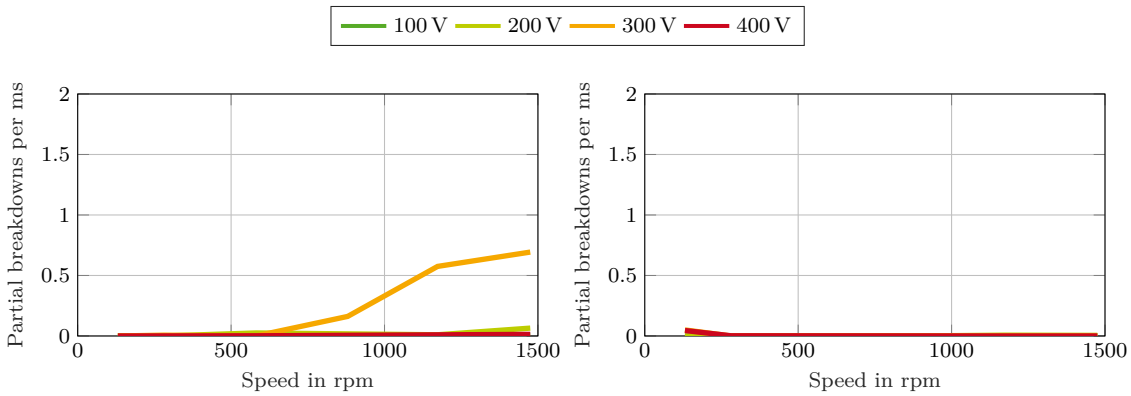

(a) Healthy rotor (b) Broken rotor bar

Figure 4.29: Number of partial breakdowns per ms for different dc-link voltages

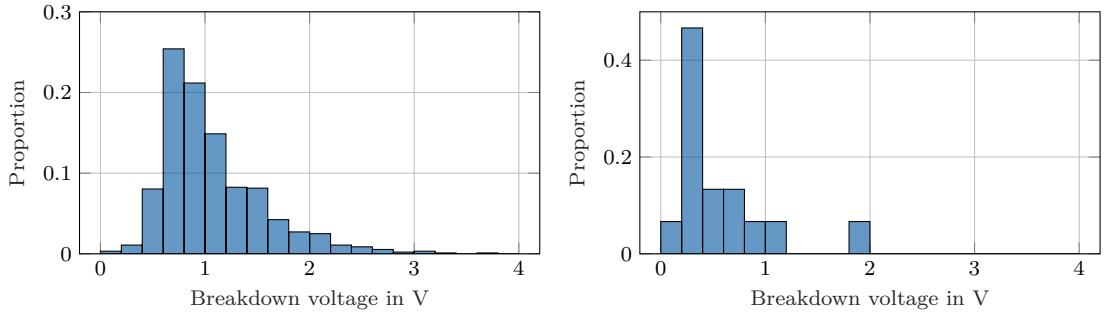

(a) Healthy rotor (b) Broken rotor bar

Figure 4.30: Distribution of breakdown voltage over all recorded partial bearing breakdowns in the machine with the broken rotor bar

Finally, in Figure 4.31b the distribution of the bearing apparent power is compared between the healthy machine and the machine with the broken rotor bar. Similar to the measurements with the healthy machine and the machine with the bearing fault, the values are significantly below the critical thresholds and pose thus no danger to the bearings of the machine.

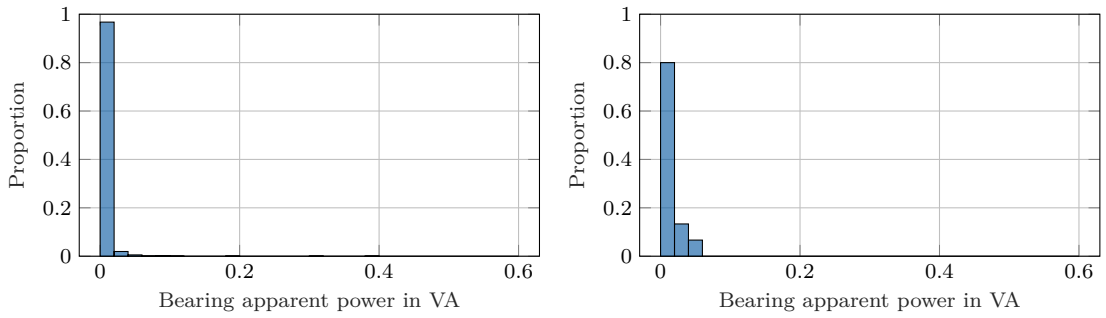

(a) Healthy rotor (b) Broken rotor bar

Figure 4.31: Distribution of BAP over all recorded partial bearing breakdowns in the machine with the broken rotor bar

4.5 Bearing Current Countermeasures

This section evaluates one of the bearing current countermeasures that are presented in section 2.2.4. The most effective bearing current countermeasure investigated in [30] is grounding the shaft to reduce the bearing voltage and create a low-impedance path for the bearing current. Therefore, a bearing voltage grounding ring from Electrostatic Technologies [34] is mounted on the DE side of the machine and the bearing voltage is measured on the NDE side.

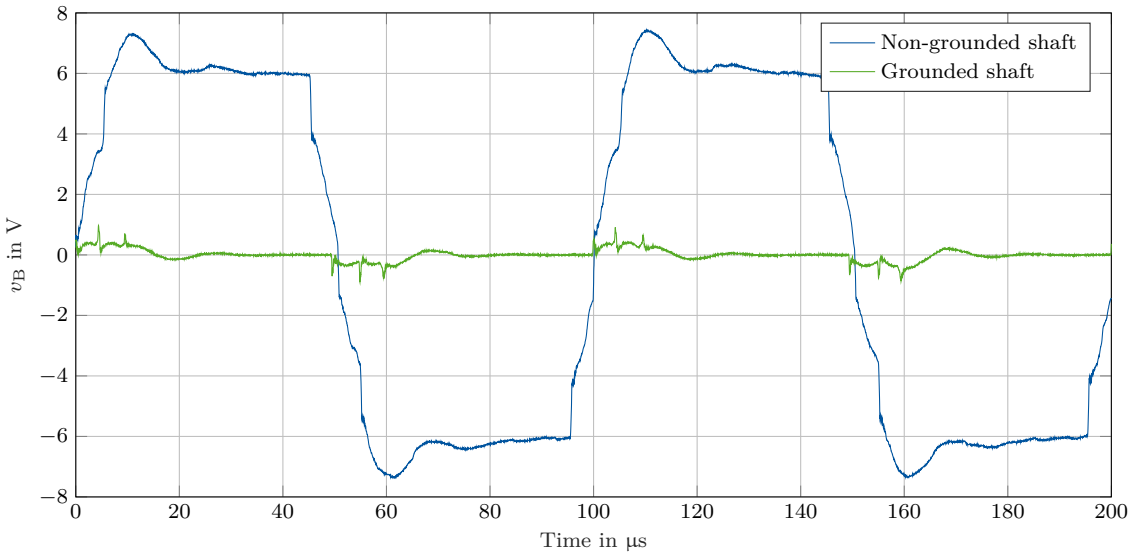

Figure 4.32: Bearing voltage with and without a shaft grounding ring

Figure 4.32 shows the bearing voltage with and without a shaft grounding ring. The maximum bearing voltage is reduced from 8 V to 1 V. The rms value is reduced even further to approximately 0.2 V. During the switching transients, the bearing voltage increases to up to 1 V, but quickly discharges again.

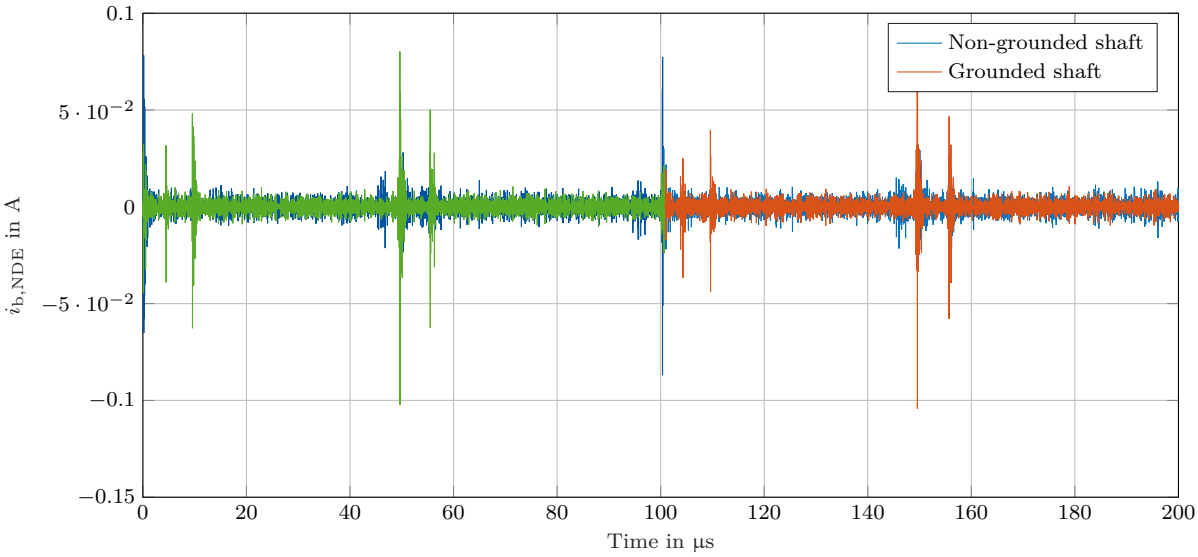

Figure 4.33: NDE bearing current with and without a shaft grounding ring at the DE

In the operating point at 400 V dc-link voltage and speed of 1475 rpm, the maximum bearing current decreases by 40 % in the DE side where the grounding ring is located. This current is assumed to flow completely through the grounding ring. The maximum bearing current at the NDE side, however, increases by 10 % compared to the NDE bearing current in the healthy machine, as can be seen in Figure 4.33. Note that in the investigated sample, no breakdowns occur in the bearings. Due to the very low shaft voltage, less breakdowns are expected to occur, especially at high rotor speed. If breakdowns occur, they would have a much lower BAP due to the reduced bearing voltage.

4.6 Summary

In this chapter, parasitic effects in electric machines have been investigated. First, the BVR was analyzed under the influence of EDM events. It was shown that, under the right conditions, the maximum bearing voltage can surpass the value that would be expected from the BVR by a factor of two. A bearing voltage estimation from the BVR is thus only valid when it can be ensured that no EDM events occur.

To assess the damage they can cause in the bearing, the EDM events themselves were analyzed. With increasing dc-link voltage and thus increasing bearing voltage, more EDM events occur. At very low speed, the number of EDM events is high as well. This is due to the low lubricant film thickness, causing a higher field strength at the same voltage levels and possibly leading to metallic contact between the bearing balls and the raceways. Even though many EDM events occur, the analysis of their BAP has shown that they are not harmful for this machine.

In EDM events, the bearing voltage fully breaks down. However, from the presented measurements, partial breakdowns, where the voltage settles at a level below the initial voltage before the breakdown, also occur. They are much rarer than full breakdown and often precede them. The correlation between the voltage drop during a partial breakdown and the voltage slope suggests that a partial discharge of parts of the distributed bearing capacitance is the most reasonable explanation.

The same investigations were repeated on a machine with a bearing fault and on a machine with a broken rotor bar. In the machine with the bearing fault, an increased number of EDM events were observed, and nearly 70 % of them occurred in the faulty bearing. The number of partial breakdowns was relatively similar compared to the healthy machine, but the voltage decrease that they incurred were slightly higher in comparison to the healthy machine. The results for the machine with the broken rotor bar are inconclusive. While the average BVR is around 30 % higher, the number of breakdowns is reduced on average by 50 %. Nearly no partial breakdowns occur. All this combined leads to the assumption that different bearings were used in the machine with the broken rotor bar.

Finally, a shaft voltage grounding ring is evaluated as means to reduce the shaft voltage. Even though the brush reduces the shaft voltage and creates a bypass path for the current in the DE bearing, the peak current in the NDE bearing increases by approximately 10 %.

5 Conclusions and Outlook

This thesis has investigated on the parasitic electrical behavior of electric machines and its relation to machine faults. It gives a comprehensive overview of these parasitic effects in electrical machines and presents a high-frequency model that enables an in-depth understanding of these effects. The presented minimally-invasive bearing current measurement technique allows to evaluate the model and to investigate the influence of faults on the electric behavior of bearings.

High-Frequency Modeling of Electric Machines

This work has proposed a detailed high-frequency model of an electric machine that can be used to model common mode currents, bearing currents and bearing voltages. A comprehensive model parameterization procedure has been presented, facilitating the adaptation of this model to other machine types and applications. By automating the fine-tuning with a particle-swarm algorithm, the effort for the parameterization of the model has been reduced significantly.

Moreover, the distributed bearing capacitance has been analyzed in detail, showing that in radially loaded bearings the capacitance is distributed unevenly. The bulk of the capacitance is shifted towards the bottom of the bearing, where most breakdowns are expected to occur. Thus, the current flow within the bearing during a breakdown has been analyzed, showing that the maximum current within the bearing is much higher than the current that can be measured from the outside.

Minimally-Invasive Bearing Current Measurement

Furthermore, a minimally-invasive method for bearing current measurement in electric machines has been presented. By placing Rogowski coils around the shaft of the machine, the bearing current can be measured without changing its path and thus influencing the impedance. Depending on the utilized Rogowski coil, the measurements can be disturbed by axial stray flux from the rotor of the machine. However, this study shows that bearing currents can be measured even with commercially available Rogowski coils with insufficient suppression of axial flux components. The frequency band, in which these disturbances

occur, is much lower than that of the bearing currents. Thus, it is possible to separate them with low- and high-pass filters.

AI-Based Fault Detection

The effectiveness of conventional fault detection methods such as motor current signature analysis (MSCA) and motor square current signature analysis (MSCSA) greatly varies depending on the operating point. Especially in low load operating points, incipient broken rotor bar faults cannot be detected reliably. However, by combining the fault frequency components from the aforementioned methods and additional information on the operating point with a k-nearest neighbor algorithm, a fault detection accuracy of 98.2 % has been achieved. The estimation of fault severity has reached an accuracy of 97.4 %.

Analysis of Bearing Voltage Breakdowns

The investigations conducted in this work have shown that bearing voltage breakdowns can lead to bearing voltages that are twice as high as the voltage that would be expected from the BVR. The occurrence of EDM events depending on the operating point was investigated in detail. It was shown that the time constant of the breakdown varies. Additionally, at high rotor speed and medium dc-link voltage, partial bearing voltage breakdowns occur. The bearing voltage is not fully discharged but settles at different voltage levels. The analysis of this effect suggests that in these cases, the breakdown resistance is higher, and that only a part of the bearing capacitances is discharged.

Influence of Faults on Bearing Voltage Breakdowns

Finally, the occurrence of bearing voltage breakdowns under different fault conditions was investigated. In a faulty bearing, at low speed, no significant bearing voltage amplitude could be observed. At low speed, the bearing was in constant breakdown due to repeating metallic contact between the rolling elements and the fault in the raceway. At higher speed, more EDM events occurred in the faulty bearing than in a healthy bearing. They can also damage the bearing further, suggesting a self-reinforcing relation between bearing faults and EDM events. For broken rotor bar (BRB)-faults, however, the results remain inconclusive.

Future Work

In future work, the bearing currents flowing inside a bearing during a breakdown should be investigated in more detail to verify the results from the distributed bearing model. A test bench could consist of a Rogowski coil placed around the steel ball in a hybrid bearing, where all balls except one are made of ceramic, similar to the test bearing used in this work. During EDM events, it can be analyzed, whether the currents flowing inside the bearing are higher than the current that can be measured on the outside, and if there is a proportionality between those two currents. This is facilitated by fixing the bearing cage to one position and rotating the inner and outer raceways of the bearing.

Further, the exact reason for partial bearing voltage breakdowns should be investigated. This requires an experimental setup, in which they can be reproduced reliably. With a reduced switching frequency, i.e., longer time between switching events, more partial breakdowns can occur and it can be determined whether they are always precursors of full breakdowns. The bearing voltage has to be applied via a capacitive voltage divider with capacitances that are similar to the parasitic capacitances in an electric machine to receive results that are transferable to an actual application.

The Rogowski coil developed in [48] should be improved in terms of signal-to-noise ratio and suppression of axial field components. This can be achieved by either increasing the manufacturing accuracy of the 3D-printed bobbin or using a printed circuit board (PCB)-based Rogowski coil. Additionally, the integrator circuit has to be improved to reduce the output noise.

The findings from the sensitivity analysis of the model suggest that the winding-to-rotor capacitance C_{WR} has a great influence on the shaft voltage. For an optimal machine design, it should be minimized, e.g. by reducing the size of the slot openings, by adding electrostatic shielding to the slot, or by changing the winding configuration.

A Appendix

A.1 Machine Impedance and Capacitance Measurements

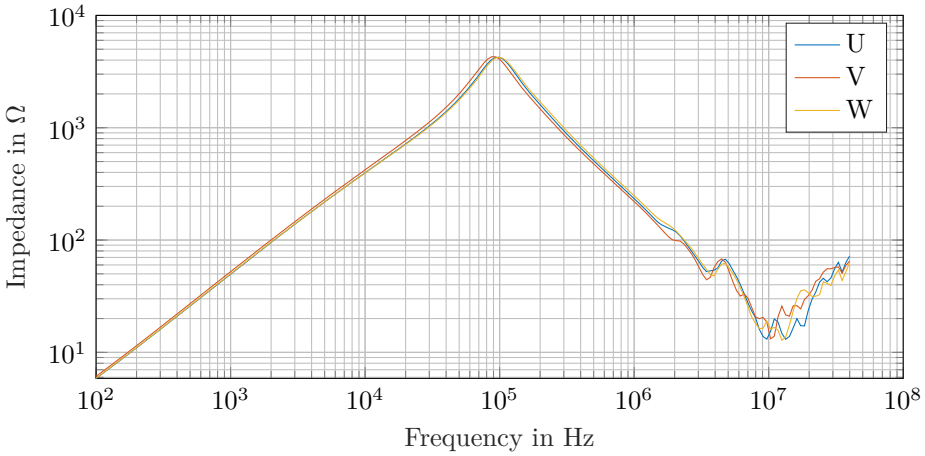

Figure A.1: Impedances measurements of all three phases

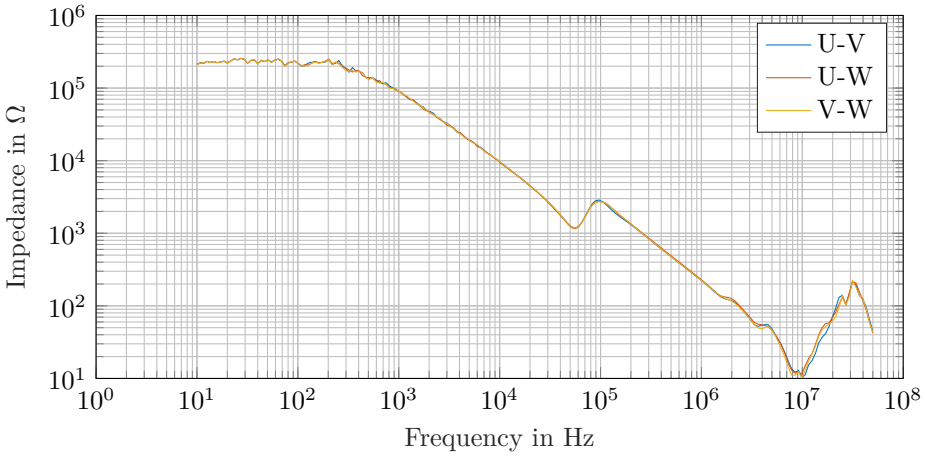

Figure A.2: Measured capacitive coupling between all three phases

A.2 Bearing Capacitance Measurements

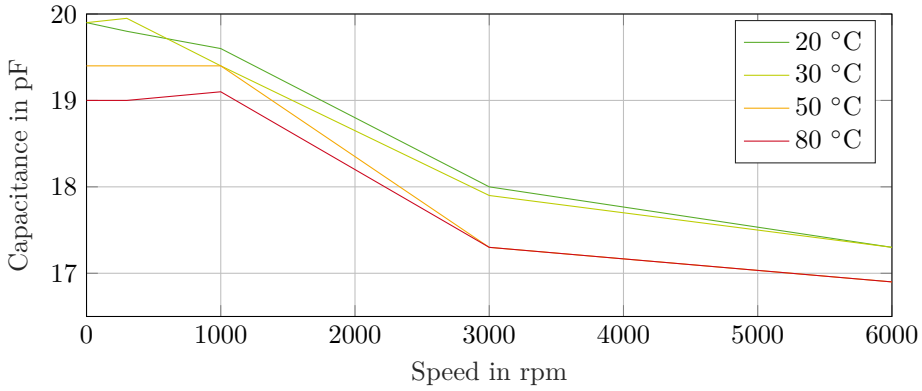

Figure A.3: Parasitic capacitance of a hybrid bearing with automatic transmission fluid (ATF) as lubricant

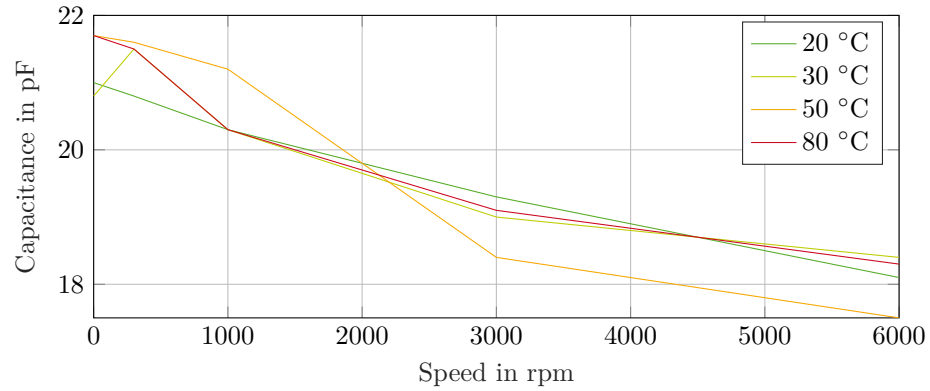

Figure A.4: Parasitic capacitance of a hybrid bearing with alkyldiphenylether (ADE) as lubricant

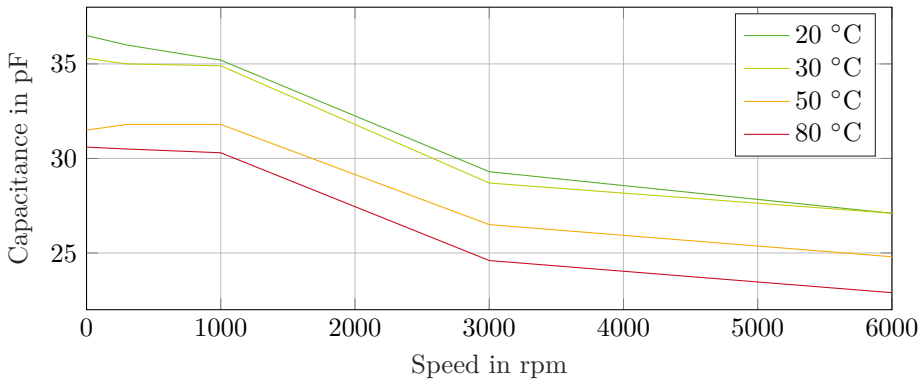

Figure A.5: Parasitic capacitance of a hybrid bearing with polyalphaolefin (PAO) as lubricant

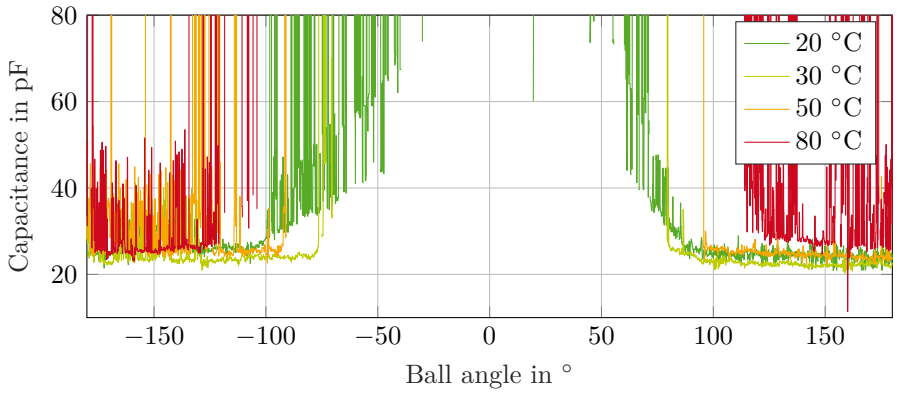

Figure A.6: Parasitic capacitance of a single bearing ball at 300 rpm with ATF as lubricant

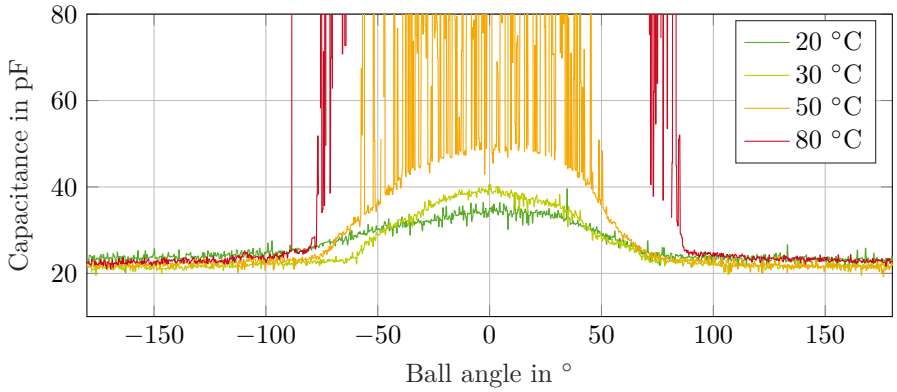

Figure A.7: Parasitic capacitance of a single bearing ball at 3000 rpm with ATF as lubricant

A.3 EDM Events

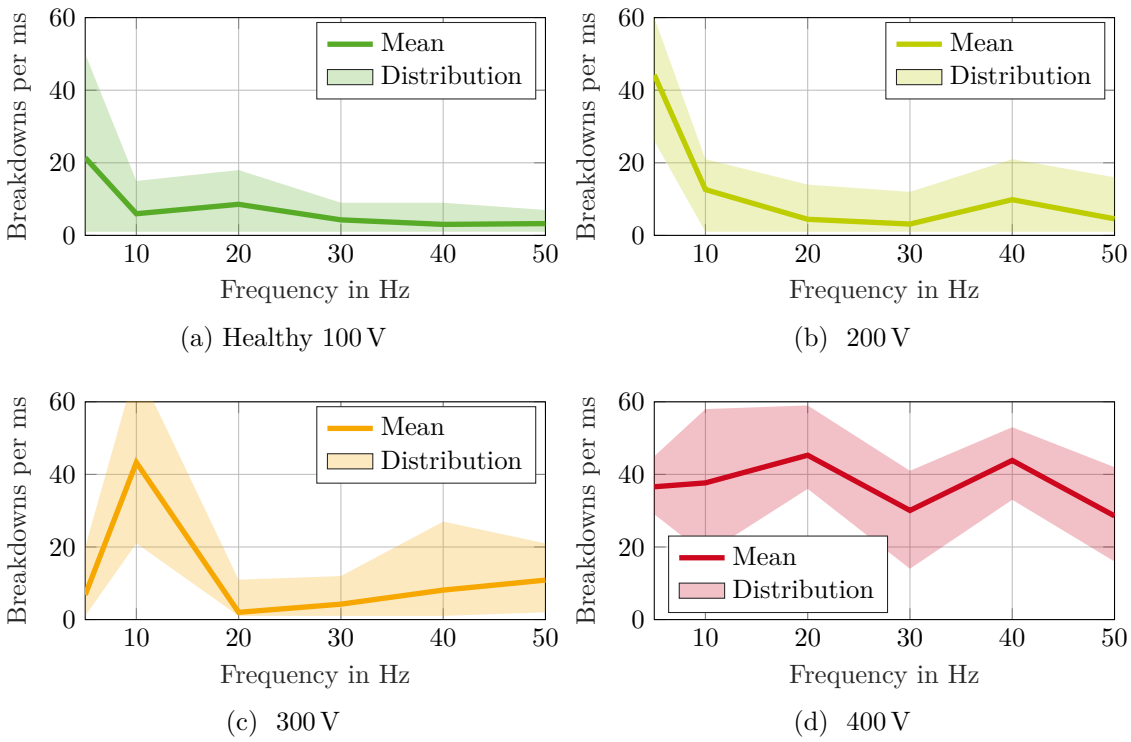

(a) Healthy 100 V (b) 200 V

(c) 300 V (d) 400 V

Figure A.8: Breakdowns per ms in a healthy machine at different dc-link voltages and speeds. 32 consecutive samples of 1 ms each

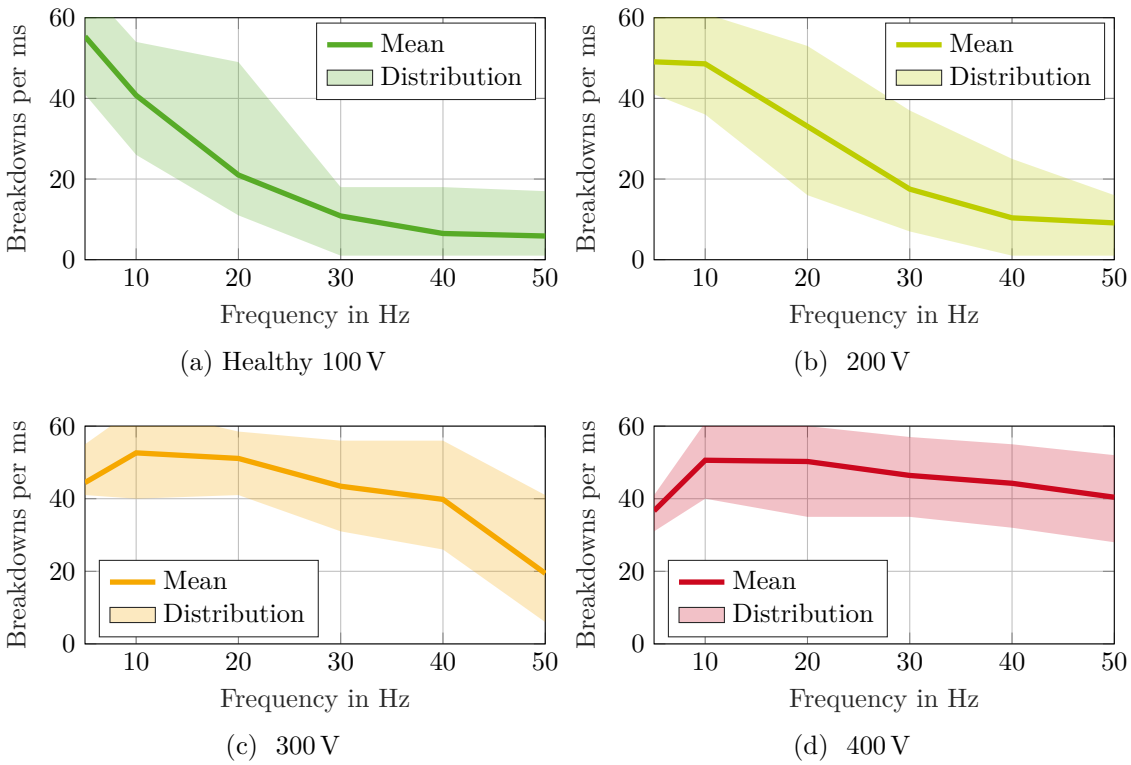

(a) Healthy 100 V (b) 200 V

(c) 300 V (d) 400 V

Figure A.9: Breakdowns per ms in a machine with a bearing fault at different dc-link voltages and speeds. 32 consecutive samples of 1 ms each

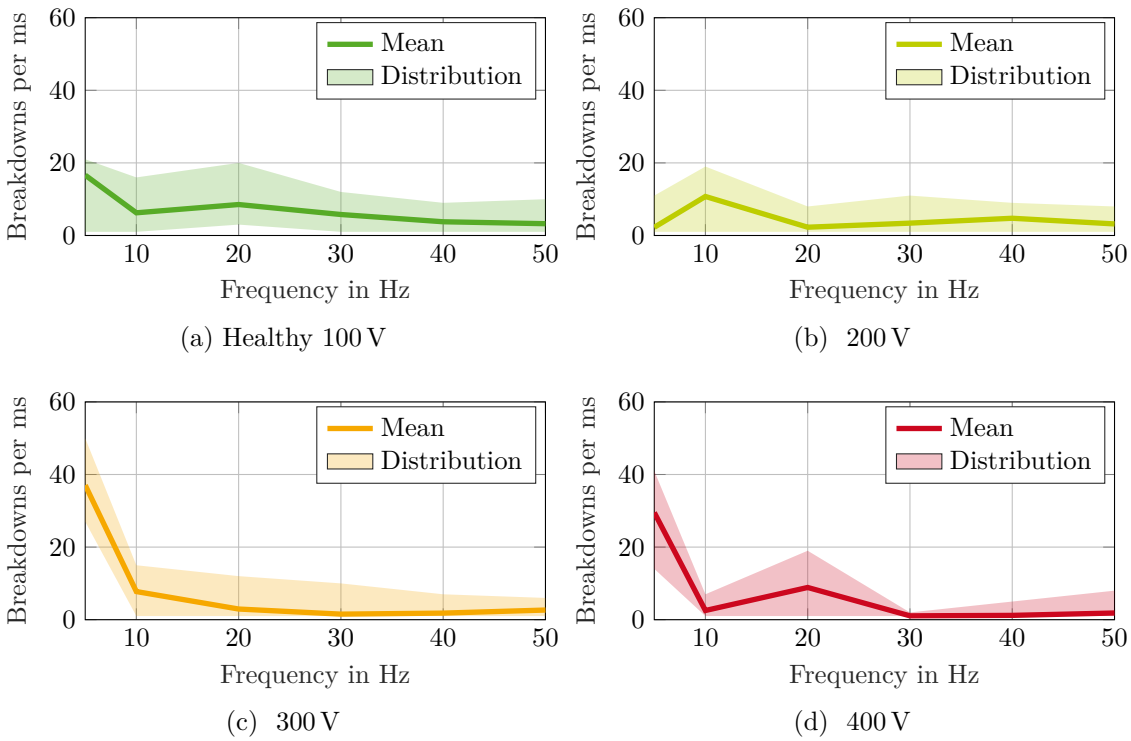

(a) Healthy 100 V (b) 200 V

(c) 300 V (d) 400 V

Figure A.10: Breakdowns per ms in a machine with a broken rotor bar at different dc-link voltages and speeds. 32 consecutive samples of 1 ms each

A.4 Partial Breakdowns

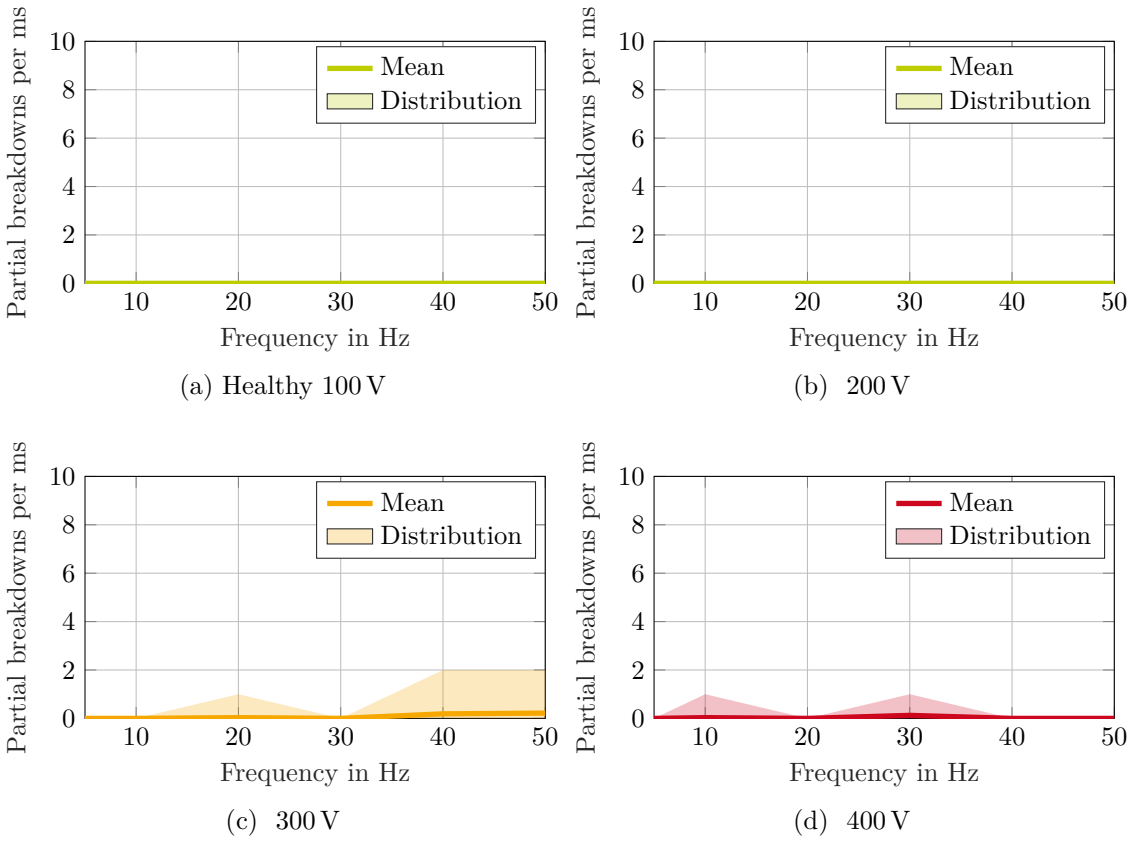

(a) Healthy 100 V (b) 200 V

(c) 300 V (d) 400 V

Figure A.11: Partial breakdowns per ms in a healthy machine at different dc-link voltages and speeds

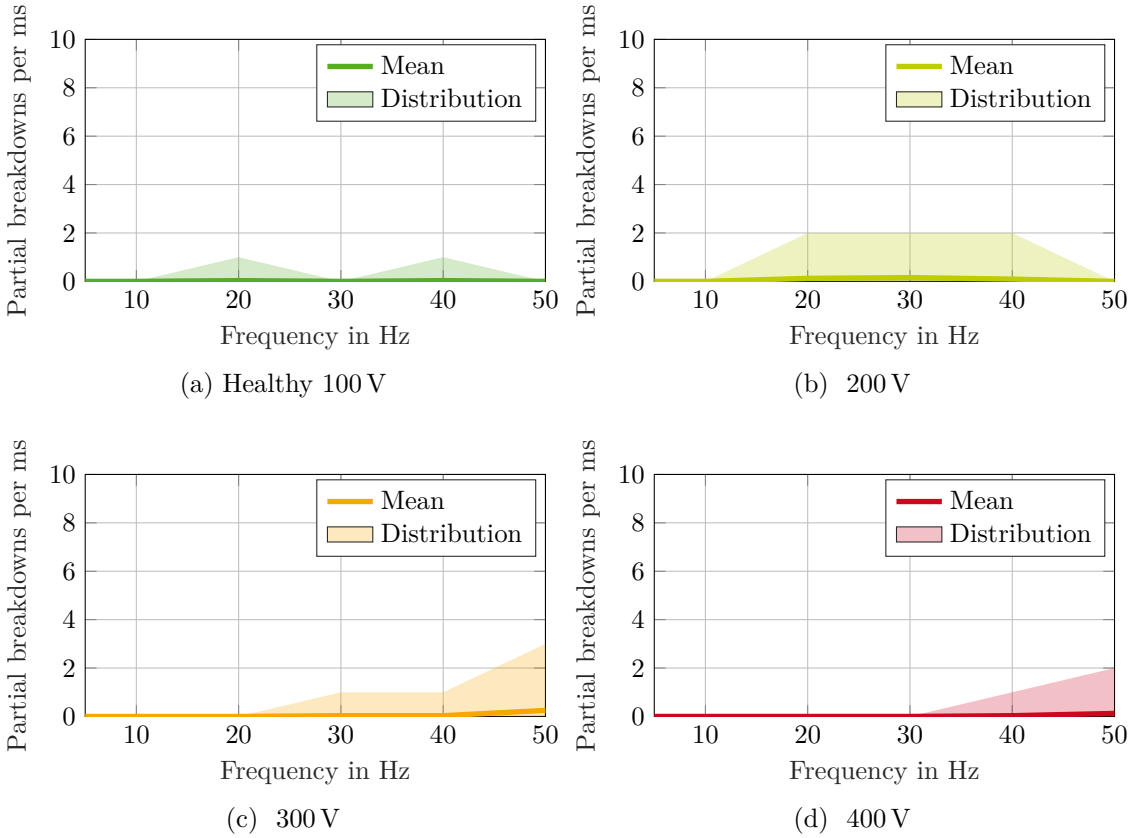

(a) Healthy 100 V (b) 200 V

(c) 300 V (d) 400 V

Figure A.12: Partial breakdowns per ms in a machine with a bearing fault at different dc-link voltages and speeds

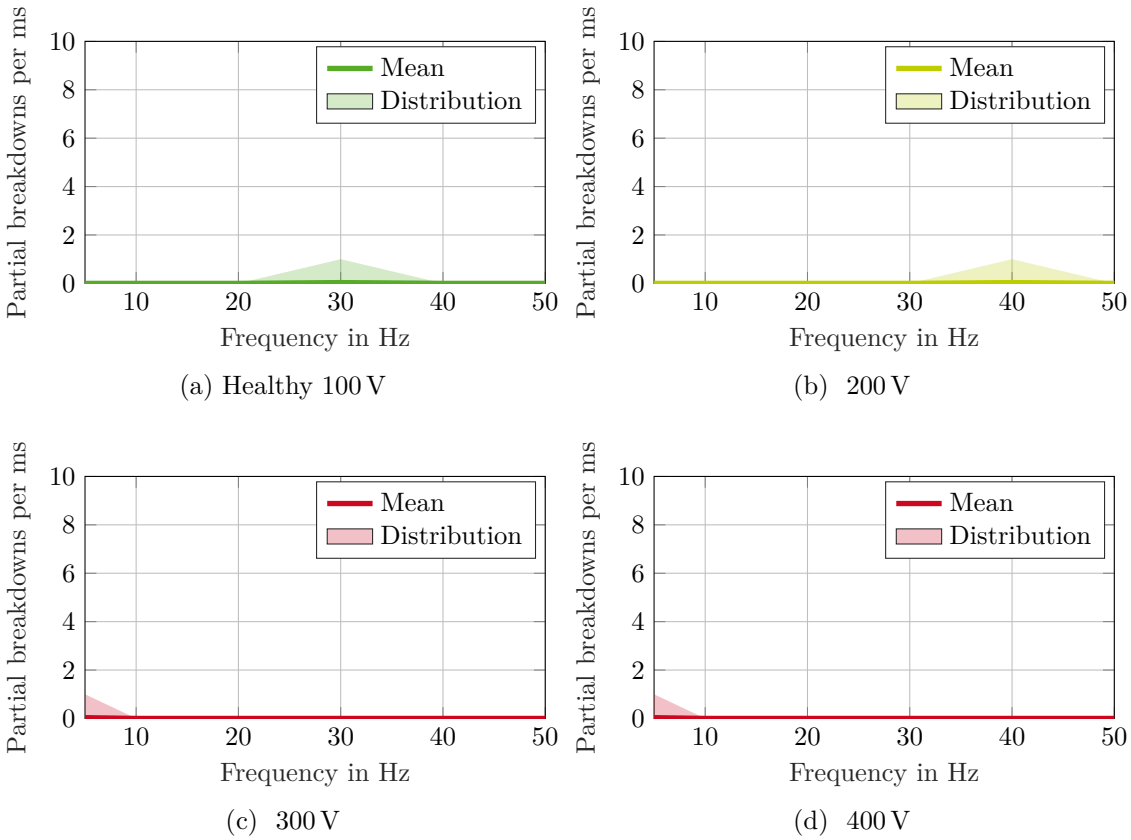

(a) Healthy 100 V (b) 200 V

(c) 300 V (d) 400 V

Figure A.13: Partial breakdowns per ms in a machine with a broken rotor bar at different dc-link voltages and speeds

List of Figures

List of Tables

Bibliography

[1] M. H. Jacobi, "Mémoire sur l'application de l'électro-magnétisme au mouvement des machines : Avec une planche," 1835.

[2] D. C. Griffith and R. M. Ulmer, "A semiconductor variable-speed a-c motor drive," *Electrical Engineering*, vol. 80, no. 5, pp. 350–353, 1961.

[3] B. Baliga, M. Adler, R. Love, P. Gray, and N. Zommer, "The insulated gate transistor: A new three-terminal mos-controlled bipolar power device," *IEEE Transactions on Electron Devices*, vol. 31, no. 6, pp. 821–828, 1984.

[4] C. Aniceto and M. Sutera, "Constant current quarter bridge dc motor drive using pwm technique with a himos transistor as a switch," in *Third International Conference on Power Electronics and Variable-Speed Drives*, 1988, pp. 407–409.

[5] J. Erdman, R. Kerkman, D. Schlegel, and G. Skibinski, "Effect of pwm inverters on ac motor bearing currents and shaft voltages," in *Proceedings of 1995 IEEE Applied Power Electronics Conference and Exposition - APEC'95*, vol. 1, 1995, 24–33 vol.1.

[6] A. Muetze, "Bearing currents in inverter-fed ac-motors," Ph.D. dissertation, Technische Universitaet Darmstadt, 2004.

[7] M. A. Vogelsberger, C. Zoeller, T. M. Wolbank, and H. Ertl, "Insulation health state monitoring of traction machines based on online switching transient exploitation," in *PCIM Europe 2017; International Exhibition and Conference for Power Electronics, Intelligent Motion, Renewable Energy and Energy Management*, 2017, pp. 1–6.

[8] T. A. Lipo, *Introduction to AC Machine Design*. John Wiley and Sons, Inc., Aug. 2017.

[9] A. Veltman, D. W. Pulle, and R. W. De Doncker, *Fundamentals of Electrical Drives*. Springer International Publishing, 2016.

[10] R. W. De Doncker, D. W. Pulle, and A. Veltman, *Advanced Electrical Drives*. Springer International Publishing, 2020.

[11] A. Bubert, J. Zhang, and R. W. De Doncker, "Modeling and measurement of capacitive and inductive bearing current in electrical machines," in *2017 Brazilian Power Electronics Conference (COBEP)*, IEEE, Nov. 2017.

[12] O. Magdun, Y. Gemeinder, and A. Binder, "Rotor impedance of the high frequency circulating bearing current path in inverter-fed ac machines," in *2013 IEEE Energy Conversion Congress and Exposition*, 2013, pp. 3512–3519.

[13] M. Weicker and A. Binder, "Characteristic parameters for electrical bearing damage," in *2022 International Symposium on Power Electronics, Electrical Drives, Automation and Motion (SPEEDAM)*, 2022, pp. 785–790.

[14] T. A. Harris and M. N. Kotzalas, *Rolling Bearing Analysis*. CRC Press, Nov. 2006.

[15] V. Schneider, C. Behrendt, P. Höltje, *et al.*, "Electrical bearing damage, a problem in the nano- and macro-range," *Lubricants*, vol. 10, no. 8, p. 194, Aug. 2022.

[16] M. Kriese, E. Wittek, S. Gattermann, H. Tischmacher, G. Poll, and B. Ponick, "Prediction of motor bearing currents for converter operation," in *The XIX International Conference on Electrical Machines - ICEM 2010*, 2010, pp. 1–6.

[17] O. Magdun, Y. Gemeinder, and A. Binder, "Investigation of influence of bearing load and bearing temperature on edm bearing currents," in *2010 IEEE Energy Conversion Congress and Exposition*, 2010, pp. 2733–2738.

[18] A. M. Bubert, *Optimization of electric vehicle drive trains with consideration of parasitic currents inside the electrical machine*, de. RWTH Aachen University, 2020.

[19] D. Busse, J. Erdman, R. Kerkman, D. Schlegel, and G. Skibinski, "Bearing currents and their relationship to PWM drives," *IEEE Transactions on Power Electronics*, vol. 12, no. 2, pp. 243–252, Mar. 1997.

[20] H. Tischmacher, "Bearing wear condition identification on converter-fed motors," in *2018 International Symposium on Power Electronics, Electrical Drives, Automation and Motion (SPEEDAM)*, 2018, pp. 19–25.

[21] A. Muetze and A. Binder, "Calculation of motor capacitances for prediction of discharge bearing currents in machines of inverter-based drive systems," in *IEEE International Conference on Electric Machines and Drives, 2005.*, 2005, pp. 264–270.

[22] E. Wittek, M. Kriese, H. Tischmacher, S. Gattermann, B. Ponick, and G. Poll, "Capacitances and lubricant film thicknesses of motor bearings under different operating conditions," in *The XIX International Conference on Electrical Machines - ICEM 2010*, 2010, pp. 1–6.

[23] E. Wittek, M. Kriese, H. Tischmacher, S. Gattermann, B. Ponick, and G. Poll, "Capacitance of bearings for electric motors at variable mechanical loads," in *2012 XXth International Conference on Electrical Machines*, 2012, pp. 1602–1607.

[24] P. Han, G. Heins, D. Patterson, M. Thiele, and D. M. Ionel, "Combined numerical and experimental determination of ball bearing capacitances for bearing current prediction," in *2020 IEEE Energy Conversion Congress and Exposition (ECCE)*, 2020, pp. 5590–5594.

[25] J. Ahola, A. Muetze, M. Niemelae, and A. Romanenko, "Normalization-based approach to electric motor bvr related capacitances computation," in *2018 IEEE Applied Power Electronics Conference and Exposition (APEC)*, 2018, pp. 2868–2874.

[26] M. Schuster and A. Binder, "Comparison of different inverter-fed ac motor types regarding common-mode bearing currents," in *2015 IEEE Energy Conversion Congress and Exposition (ECCE)*, 2015, pp. 2762–2768.

[27] T. Svimonishvili, F. Fan, K. Y. See, X. Liu, M. A. Zagrodnik, and A. K. Gupta, "High-frequency model and simulation for the investigation of bearing current in inverter-driven induction machines," in *2016 IEEE Region 10 Conference (TENCON)*, 2016, pp. 55–59.

[28] O. Magdun and A. Binder, "The high-frequency induction machine parameters and their influence on the common mode stator ground current," in *2012 XXth International Conference on Electrical Machines*, 2012, pp. 505–511.

[29] O. Magdun and A. Binder, "High-frequency induction machine modeling for common mode current and bearing voltage calculation," *IEEE Transactions on Industry Applications*, vol. 50, no. 3, pp. 1780–1790, 2014.

[30] S. Quabeck, V. Grau, and R. W. De Doncker, "Modeling and mitigation of bearing currents in electrical traction drives," in *2020 23rd International Conference on Electrical Machines and Systems (ICEMS)*, 2020, pp. 1101–1106.

[31] M. Schinkel, S. Weber, S. Guttowski, W. John, and H. Reichl, "Efficient hf modeling and model parameterization of induction machines for time and frequency domain simulations," in *Twenty-First Annual IEEE Applied Power Electronics Conference and Exposition, 2006. APEC '06.*, 2006.

[32] P. Han, G. Heins, D. Patterson, M. Thiele, and D. M. Ionel, "Evaluation of bearing voltage reduction in electric machines by using insulated shaft and bearings," in *2020 IEEE Energy Conversion Congress and Exposition (ECCE)*, 2020, pp. 5584–5589.

[33] T. Plazenet, T. Boileau, C. Caironi, and B. Nahid-Mobarakeh, "An overview of shaft voltages and bearing currents in rotating machines," in *2016 IEEE Industry Applications Society Annual Meeting*, 2016, pp. 1–8.

[34] (), [Online]. Available: https://www.est-aegis.com.

[35] B. Bai, Y. Wang, and X. Wang, "Suppression for discharging bearing current in variable-frequency motors based on electromagnetic shielding slot wedge," *IEEE Transactions on Magnetics*, vol. 51, no. 11, pp. 1–4, 2015.

[36] J.-S. Kim and K.-H. Nam, "A method of lowering bearing current with embedded circular comb-like coil," in *Conference Record of the 2000 IEEE Industry Applications Conference. Thirty-Fifth IAS Annual Meeting and World Conference on Industrial Applications of Electrical Energy (Cat. No.00CH37129)*, vol. 3, 2000, 1670–1674 vol.3.

[37] R. Liu, E. Yang, J. Chen, and S. Niu, "Novel bearing current suppression approach in doubly-fed induction generators," *IEEE Access*, vol. 7, pp. 171 525–171 532, 2019.

[38] J. Erdman, R. Kerkman, D. Schlegel, and G. Skibinski, "Effect of pwm inverters on ac motor bearing currents and shaft voltages," *IEEE Transactions on Industry Applications*, vol. 32, no. 2, pp. 250–259, 1996.

[39] P. Han, G. Heins, D. Patterson, M. Thiele, and D. M. Ionel, "Modeling of bearing voltage in electric machines based on electromagnetic fea and measured bearing capacitance," *IEEE Transactions on Industry Applications*, vol. 57, no. 5, pp. 4765–4775, 2021.

[40] A. Kempski, R. Strzelecki, R. Smolenski, and Z. Fedyczak, "Bearing current path and pulse rate in pwm-inverter-fed induction," in *2001 IEEE 32nd Annual Power Electronics Specialists Conference (IEEE Cat. No.01CH37230)*, vol. 4, 2001, 2025–2030 vol. 4.

[41] Y. Gemeinder, M. Schuster, B. Radnai, B. Sauer, and A. Binder, "Calculation and validation of a bearing impedance model for ball bearings and the influence on edm-currents," in *2014 International Conference on Electrical Machines (ICEM)*, 2014, pp. 1804–1810.

[42] O. Magdun, Y. Gemeinder, A. Binder, and K. Reis, "Calculation of bearing and common-mode voltages for the prediction of bearing failures caused by edm currents," in *8th IEEE Symposium on Diagnostics for Electrical Machines, Power Electronics and Drives*, 2011, pp. 462–467.

[43] S. Quabeck, D. C. Rodriguez, and R. W. De Doncker, "Modeling and measuring the bearing capacitance of radially loaded bearings," in *2022 24th European Conference on Power Electronics and Applications (EPE'22 ECCE Europe)*, 2022, pp. 1–10.

[44] J. O. Stockbruegger, "Analytische bestimmung parasitaerer kapazitaeten in elektrischen maschinen," de, Ph.D. dissertation, Leibniz University Hannover, 2021.

[45] A. Ganjavi, H. Rathnayake, F. Zare, *et al.*, "Common-mode current prediction and analysis in motor drive systems for the new frequency range of 2–150 khz," *IEEE Journal of Emerging and Selected Topics in Power Electronics*, vol. 10, no. 1, pp. 74–90, 2022.

[46] D. R. Quintero, W. Mejia, and J. A. Rosero, "Good practice for electric discharge machining (edm) bearing currents measurement in the induction motor and drives system," in *2013 International Electric Machines and Drives Conference*, 2013, pp. 1384–1390.

[47] W. Mejia and J. A. Rosero, "Measurement of common mode currents in induction motors fed by a motor drive," in *2013 International Electric Machines and Drives Conference*, 2013, pp. 106–110.

[48] S. Quabeck, L. Braun, N. Fritz, S. Klever, and R. W. De Doncker, "A machine integrated rogowski coil for bearing current measurement," in *2021 IEEE 13th International Symposium on Diagnostics for Electrical Machines, Power Electronics and Drives (SDEMPED)*, vol. 1, 2021, pp. 17–23.

[49] A. Muetze, V. Niskanen, and J. Ahola, "On radio-frequency-based detection of high-frequency circulating bearing current flow," *IEEE Transactions on Industry Applications*, vol. 50, no. 4, pp. 2592–2601, 2014.

[50] B. Muralidhara, A. Ramachandran, R. Srinivasan, and M. C. Reddy, "Experimental investigation and measurement of the bearing current in a multilevel inverter-fed induction motor drive," in *2011 3rd International Conference on Electronics Computer Technology*, vol. 4, 2011, pp. 444–448.

[51] X. Shancheng and W. Zhengguo, "Characteristic research of bearing currents in inverter-motor drive systems," in *2006 CES/IEEE 5th International Power Electronics and Motion Control Conference*, vol. 2, 2006, pp. 1–4.

[52] H. Tischmacher, S. Gattermann, M. Kriese, and E. Wittek, "Bearing wear caused by converter-induced bearing currents," in *IECON 2010 - 36th Annual Conference on IEEE Industrial Electronics Society*, 2010, pp. 784–791.

[53] R. Ong, J. Dymond, and R. Findlay, "Comparison of techniques for measurement of shaft currents in rotating machines," *IEEE Transactions on Energy Conversion*, vol. 12, no. 4, pp. 363–367, 1997.

[54] R. Ong, J. Dymond, R. Findlay, and B. Szabados, "Shaft current in ac induction machine. an online monitoring system and prediction rules," *IEEE Transactions on Industry Applications*, vol. 37, no. 4, pp. 1189–1196, 2001.

[55] D. Heide, B. Knebusch, A. Ebrahimi, and B. Ponick, "Measurement of parasitic high-frequency currents in inverter-fed low-speed electrical machines using rogowski current sensors," in *2021 23rd European Conference on Power Electronics and Applications (EPE'21 ECCE Europe)*, 2021, P.1–P.9.

[56] N. Ville, P. Antti, and A. Jero, "Hf near-field probe for magnitude measurements of edm bearing currents," in *2014 16th European Conference on Power Electronics and Applications*, 2014, pp. 1–11.

[57] V. Kokko, "Condition monitoring of squirrel-cage motors by axial magnetic flux measurements," de, Ph.D. dissertation, University of Oulu, 2003.

[58] N. Fritz, C. Neeb, and R. W. De Doncker, "A PCB integrated differential rogowski coil for non-intrusive current measurement featuring high bandwidth and dv/dt immunity," in *Power and Energy Student Summit (PESS)*, Jan. 2015.

[59] W. Ray and R. Davis, *High frequency improvements in wide bandwith rogowski current transducers*, 8th European Conference on Power Electronics and Applications, Lausanne, 1999.

[60] J. Pettinga and J. Siersema, "A polyphase 500 kA current measuring system with rogowski coils," *IEE Proceedings B Electric Power Applications*, vol. 130, no. 5, p. 360, 1983.

[61] *Cwt mini*, Power Electronic Measurements Ltd., Feb. 2020. eprint: `http://www.pemuk.com/Userfiles/CWTmini/CWT_Mini_DS_Feb_2020.pdf`.

[62] *Cwt ultra-mini*, Power Electronic Measurements Ltd., Feb. 2020. eprint: `http://www.pemuk.com/Userfiles/CWTum/CWTUM_DS_Feb_2020.pdf`.

[63] *Ksz 100 d*, Power Electronic Measurements Ltd., 2022.

[64] A. Muetze and A. Binder, "Techniques for measurement of parameters related to inverter-induced bearing currents," *IEEE Transactions on Industry Applications*, vol. 43, no. 5, pp. 1274–1283, 2007.

[65] S. Nandi, H. Toliyat, and X. Li, "Condition monitoring and fault diagnosis of electrical motors—a review," *IEEE Transactions on Energy Conversion*, vol. 20, no. 4, pp. 719–729, 2005.

[66] Y. Gritli, A. Bellini, C. Rossi, D. Casadei, F. Filippetti, and G.-A. Capolino, "Condition monitoring of mechanical faults in induction machines from electrical signatures: Review of different techniques," in *2017 IEEE 11th International Symposium on Diagnostics for Electrical Machines, Power Electronics and Drives (SDEMPED)*, 2017, pp. 77–84.

[67] J. Kammermann, I. Bolvashenkov, S. Schwimmbeck, and H.-G. Herzog, "Reliability of induction machines: Statistics, tendencies, and perspectives," in *2017 IEEE 26th International Symposium on Industrial Electronics (ISIE)*, 2017, pp. 1843–1847.

[68] Y. Gemeinder and M. Weicker, *Application guide bearing currents*, en. Darmstadt, 2021, 84 Seiten.

[69] M. Cash, T. Habetler, and G. Kliman, "Insulation failure prediction in induction machines using line-neutral voltages," in *IAS '97. Conference Record of the 1997 IEEE Industry Applications Conference Thirty-Second IAS Annual Meeting*, vol. 1, 1997, 208–212 vol.1.

[70] F. Salameh, A. Picot, M. Chabert, and P. Maussion, "Parametric and nonparametric models for lifespan modeling of insulation systems in electrical machines," *IEEE Transactions on Industry Applications*, vol. 53, no. 3, pp. 3119–3128, 2017.

[71] V. C. Grau, "Development of a test bench to investigate the impact of steep voltage slopes on the lifetime of insulation systems for coil windings," en, Ph.D. dissertation, RWTH Aachen University, 2021, p. 2021.

[72] O. Imoru, A. A. Jimoh, and Y. Hamam, "Origin and manifestation of electrical machine faults-a review," in *The 2nd IEEE Conference on Power Engineering and Renewable Energy (ICPERE) 2014*, 2014, pp. 189–194.

[73] A. Gandhi, T. Corrigan, and L. Parsa, "Recent advances in modeling and online detection of stator interturn faults in electrical motors," *IEEE Transactions on Industrial Electronics*, vol. 58, no. 5, pp. 1564–1575, 2011.

[74] G. Kliman, W. Premerlani, R. Koegl, and D. Hoeweler, "A new approach to on-line turn fault detection in ac motors," in *IAS '96. Conference Record of the 1996 IEEE Industry Applications Conference Thirty-First IAS Annual Meeting*, vol. 1, 1996, 687–693 vol.1.

[75] D. Basak, A. Tiwari, and S. P. Das, "Fault diagnosis and condition monitoring of electrical machines - a review," in *2006 IEEE International Conference on Industrial Technology*, Dec. 2006, pp. 3061–3066.

[76] S. Quabeck, D. Scharfenstein, and R. W. De Doncker, "Speed dependency of the induction machine phase current spectrum under fault conditions," in *2019 22nd International Conference on Electrical Machines and Systems (ICEMS)*, IEEE, Aug. 2019.

[77] S. Quabeck, W. Shangguan, D. Scharfenstein, and R. W. De Doncker, "Detection of broken rotor bars in induction machines using machine learning methods," in *2020 23rd International Conference on Electrical Machines and Systems (ICEMS)*, Nov. 2020, pp. 620–625.

[78] S. Quabeck, W. Shangguan, D. Scharfenstein, and R. W. De Doncker, "Detection of broken rotor bars in induction machines using machine learning methods," *IEEJ Journal of Industry Applications*, vol. 10, no. 6, pp. 688–693, Nov. 1, 2021.

[79] M. Riera-Guasp, J. A. Antonino-Daviu, and G.-A. Capolino, "Advances in electrical machine, power electronic, and drive condition monitoring and fault detection: State of the art," *IEEE Transactions on Industrial Electronics*, vol. 62, no. 3, pp. 1746–1759, 2015.

[80] G. Kliman, R. Koegl, J. Stein, R. Endicott, and M. Madden, "Noninvasive detection of broken rotor bars in operating induction motors," *IEEE Transactions on Energy Conversion*, vol. 3, no. 4, pp. 873–879, 1988.

[81] R. C. Kryter and H. D. Haynes, "Condition monitoring of machinery using motor current signature analysis," Jan. 1989.

[82] V. F. Pires, D. Foito, J. F. Martins, and A. J. Pires, "Detection of stator winding fault in induction motors using a motor square current signature analysis (mscsa)," in *2015 IEEE 5th International Conference on Power Engineering, Energy and Electrical Drives (POWERENG)*, 2015, pp. 507–512.

[83] S. Legowski, A. Sadrul Ula, and A. Trzynadlowski, "Instantaneous power as a medium for the signature analysis of induction motors," *IEEE Transactions on Industry Applications*, vol. 32, no. 4, pp. 904–909, 1996.

[84] V. F. Pires, J. F. Martins, A. J. Pires, and L. Rodrigues, "Induction motor broken bar fault detection based on mcsa, mscsa and pca: A comparative study," in *2016 10th International Conference on Compatibility, Power Electronics and Power Engineering (CPE-POWERENG)*, Jun. 2016, pp. 298–303.

[85] E. Clarke, *Circuit Analysis of A-C Power Systems* (Circuit Analysis of A-C Power Systems). J. Wiley & sons, Incorporated, 1943, vol. 1.

[86] L. Shuang and Y. Fujin, "Fault pattern recognition of bearing based on principal components analysis and support vector machine," in *2009 Second International Conference on Intelligent Computation Technology and Automation*, vol. 2, 2009, pp. 533–536.

[87] R. Schoen, T. Habetler, F. Kamran, and R. Bartfield, "Motor bearing damage detection using stator current monitoring," *IEEE Transactions on Industry Applications*, vol. 31, no. 6, pp. 1274–1279, 1995.

[88] L. Jiang, X. Fu, J. Cui, and Z. Li, "Fault detection of rolling element bearing based on principal component analysis," in *2012 24th Chinese Control and Decision Conference (CCDC)*, 2012, pp. 2944–2948.

[89] A. Bubert, S.-H. Lim, and R. W. De Doncker, "Comparison of 2-level b6c and 3-level npc inverter topologies for electric vehicles," in *2017 IEEE Southern Power Electronics Conference (SPEC)*, 2017, pp. 1–6.

[90] K. Oberdieck, "Measurement and mitigation of electromagnetic emissions of propulsion inverters for electric vehicles," Dissertation, Rheinisch-Westfälische Technischen Hochschule Aachen, Aachen, 2020, 1 Online–Ressource (viii, 181 Seiten) : Illustrationen, Diagramme.

[91] M. Drakaki, Y. Karnavas, A. Karlis, I. Chasiotis, and P. Tzionas, "Study on fault diagnosis of broken rotor bars in squirrel cage induction motors: A multi-agent system approach using intelligent classifiers," *IET Electric Power Applications*, Nov. 2019.

[92] C. M. Pezzani, J. M. Fontana, P. D. Donolo, C. H. De Angelo, G. R. Bossio, and L. I. Silva, "Svm-based system for broken rotor bar detection in induction motors," in *2018 IEEE ANDESCON*, Aug. 2018, pp. 1–6.

[93] N. A. Mohsun, "Broken rotor bar fault classification for induction motor based on support vector machine-SVM," in *2017 International Conference on Engineering & MIS (ICEMIS)*, IEEE, May 2017.

[94] Cao Zhitong, Fang Jiazhong, Chen Hongpingn, He Guoguang, and E. Ritchie, "Support vector machine used to diagnose the fault of rotor broken bars of induction motors," in *Sixth International Conference on Electrical Machines and Systems, 2003. ICEMS 2003.*, vol. 2, 2003, 891–894 vol.2.

[95] D. Matić, F. Kulić, I. Kamenko, V. Bugarski, and P. Nikolić, "Design of support vector machine classifier for broken bar detection," in *2012 IEEE International Conference on Control Applications*, 2012, pp. 1670–1673.

[96] B. Amel, Y. Laatra, S. Sami, and D. Nourreddine, "Classification and diagnosis of broken rotor bar faults in induction motor using spectral analysis and svm," in *2013 Eighth International Conference and Exhibition on Ecological Vehicles and Renewable Energies (EVER)*, 2013, pp. 1–5.

[97] W. F. Godoy, I. N. da Silva, T. D. Lopes, A. Goedtel, and R. H. C. Palácios, "Application of intelligent tools to detect and classify broken rotor bars in three-phase induction motors fed by an inverter," *IET Electric Power Applications*, vol. 10, no. 5, pp. 430–439, May 2016.

[98] K. Edomwandekhoe and X. Liang, "Advanced feature selection for broken rotor bar faults in induction motors," in *2018 IEEE/IAS 54th Industrial and Commercial Power Systems Technical Conference (I CPS)*, May 2018, pp. 1–10.

[99] *Keysight n2780b seriesac/dc current probes*, Keysight Technologies Inc., 2022.

[100] M. Kriese, E. Wittek, S. Gattermann, H. Tischmacher, G. Poll, and B. Ponick, "Influence of bearing currents on the bearing lifetime for converter driven machines," in *2012 XXth International Conference on Electrical Machines*, 2012, pp. 1735–1739.

[101] J. Cusido, A. Garcia, L. Navarro, M. Delgado, L. Romeral, and A. Ortega, "On-line measurement device to detect bearing faults on electric motors," in *2009 IEEE Instrumentation and Measurement Technology Conference*, 2009, pp. 749–752.

[102] M. Koch, S. Tenbohlen, and M. Fischer, “The breakdown voltage of insulation oil under the influence of humidity, acidity,particles and pressure,” presented at the International Conference on Advances in Processing, Testing and Application of Dielectric Materials APTADM (Wroclaw, Poland, Sep. 27, 2020), Sep. 27, 2020.

[103] G. Engelmann, S. Quabeck, J. Gottschlich, and R. W. De Doncker, “Experimental and simulative investigations on stray capacitances and stray inductances of power modules,” in *2017 19th European Conference on Power Electronics and Applications (EPE'17 ECCE Europe)*, 2017, P.1–P.10.

[104] A. P. Opgenoorth, S. Quabeck, R. W. de Doncker, and K. Schmitz, “Challenges and possibilities of the integration of electric drives in mobile machinery,” in *12th International Fluid Power Conference (12. IFK) : October 12-14, 2020 in Dresden.*, 12th International Fluid Power Conference, Dresden (Germany), 12 Oct 2020 - 14 Oct 2020, Dresden: Dresdner Verein zur Förderung der Fluidtechnik e. V. Dresden, Oct. 12, 2020, pp. 471–480.

[105] D. Scharfenstein, S. Schüller, S. Quabeck, and R. W. D. Doncker, “Modeling of induction machines with switched stator windings,” in *2020 IEEE Transportation Electrification Conference & Expo (ITEC)*, 2020, pp. 1050–1055.

[106] X. Yu, S. Quabeck, S. Schueller, and R. W. De Doncker, “Modelling of broken rotor bars and eccentricity faults in squirrel cage induction machines,” in *2021 IEEE 13th International Symposium on Diagnostics for Electrical Machines, Power Electronics and Drives (SDEMPED)*, vol. 1, 2021, pp. 133–139.

[107] V. Grau, M. Reisner, S. Quabeck, and R. W. De Doncker, “Sic-based dv/dt generator for insulation testing with fast and adjustable switching transients,” in *2021 IEEE 8th Workshop on Wide Bandgap Power Devices and Applications (WiPDA)*, 2021, pp. 188–193.

List of Publications

Journal Articles (1)

1. S. Quabeck, W. Shangguan, D. Scharfenstein, and R. W. De Doncker, "Detection of broken rotor bars in induction machines using machine learning methods," *IEEJ Journal of Industry Applications*, vol. 10, no. 6, pp. 688–693, Nov. 1, 2021

Conference Proceedings (10)

1. G. Engelmann, S. Quabeck, J. Gottschlich, and R. W. De Doncker, "Experimental and simulative investigations on stray capacitances and stray inductances of power modules," in *2017 19th European Conference on Power Electronics and Applications (EPE'17 ECCE Europe)*, 2017, P.1–P.10
2. S. Quabeck, D. Scharfenstein, and R. W. De Doncker, "Speed dependency of the induction machine phase current spectrum under fault conditions," in *2019 22nd International Conference on Electrical Machines and Systems (ICEMS)*, IEEE, Aug. 2019
3. A. P. Opgenoorth, S. Quabeck, R. W. de Doncker, and K. Schmitz, "Challenges and possibilities of the integration of electric drives in mobile machinery," in *12th International Fluid Power Conference (12. IFK) : October 12-14, 2020 in Dresden.*, 12th International Fluid Power Conference, Dresden (Germany), 12 Oct 2020 - 14 Oct 2020, Dresden: Dresdner Verein zur Förderung der Fluidtechnik e. V. Dresden, Oct. 12, 2020, pp. 471–480
4. S. Quabeck, V. Grau, and R. W. De Doncker, "Modeling and mitigation of bearing currents in electrical traction drives," in *2020 23rd International Conference on Electrical Machines and Systems (ICEMS)*, 2020, pp. 1101–1106
5. S. Quabeck, W. Shangguan, D. Scharfenstein, and R. W. De Doncker, "Detection of broken rotor bars in induction machines using machine learning methods," in *2020 23rd International Conference on Electrical Machines and Systems (ICEMS)*, Nov. 2020, pp. 620–625
6. D. Scharfenstein, S. Schüller, S. Quabeck, and R. W. D. Doncker, "Modeling of induction machines with switched stator windings," in *2020 IEEE Transportation Electrification Conference & Expo (ITEC)*, 2020, pp. 1050–1055
7. S. Quabeck, L. Braun, N. Fritz, S. Klever, and R. W. De Doncker, "A machine integrated rogowski coil for bearing current measurement," in *2021 IEEE 13th International Symposium on Diagnostics for Electrical Machines, Power Electronics and Drives (SDEMPED)*, vol. 1, 2021, pp. 17–23
8. X. Yu, S. Quabeck, S. Schueller, and R. W. De Doncker, "Modelling of broken rotor bars and eccentricity faults in squirrel cage induction machines," in *2021 IEEE 13th International Symposium on Diagnostics for Electrical Machines, Power Electronics and Drives (SDEMPED)*, vol. 1, 2021, pp. 133–139
9. V. Grau, M. Reisner, S. Quabeck, and R. W. De Doncker, "Sic-based dv/dt generator for insulation testing with fast and adjustable switching transients," in *2021 IEEE 8th Workshop on Wide Bandgap Power Devices and Applications (WiPDA)*, 2021, pp. 188–193
10. S. Quabeck, D. C. Rodriguez, and R. W. De Doncker, "Modeling and measuring the bearing capacitance of radially loaded bearings," in *2022 24th European Conference on Power Electronics and Applications (EPE'22 ECCE Europe)*, 2022, pp. 1–10

ABISEA Band 1
Eßer, Albert
Berührungslose, kombinierte Energie- und Informationsübertragung für bewegliche Systeme
1. Aufl. 1992, 129 S.
ISBN 3-86073-046-0

ABISEA Band 2
Vogel, Ulrich
Entwurf und Beurteilung von Verfahren zur Hochausnutzung des Rad-Schiene-Kraftschlusses durch Triebfahrzeuge
1. Aufl. 1992, 131 S.
ISBN 3-86073-060-6

ABISEA Band 3
Reckhorn, Thomas
Stromeinprägendes Antriebssystem mit fremderregter Synchronmaschine
1. Aufl. 1992, 128 S.
ISBN 3-86073-061-4

ABISEA Band 4
Ackva, Ansgar
Spannungseinprägendes Antriebssystem mit Synchronmaschine und direkter Stromregelung
1. Aufl. 1992, 137 S.
ISBN 3-86073-062-2

ABISEA Band 5
Mertens, Axel
Analyse des Oberschwingungsverhaltens von taktsynchronen Delta - Modulationsverfahren zur Steuerung von Pulsstromrichtern bei hoher Taktzahl
1. Aufl. 1992, 178 S.
ISBN 3-86073-069-X

ABISEA Band 6
Geuer, Wolfgang
Untersuchungen über das Alterungsverhalten von Blei-Akkumulatoren
1. Aufl. 1993, 97 S.
ISBN 3-86073-097-5

ABISEA Band 7
Langheim, Jochen
Einzelradantrieb für Elektrostraßenfahrzeuge
1. Aufl. 1993, 213 S.
ISBN 3-86073-123-8
(vergriffen)

ABISEA Band 8
Fetz, Joachim
Fehlertolerante Regelung eines Asynchron-Doppelantriebes für ein Elektrospeicherfahrzeug
1. Aufl. 1993, 136 S.
ISBN 3-86073-124-6
(vergriffen)

ABISEA Band 9
Schülting, Ludger
Optimierte Auslegung induktiver Bauelemente für den Mittelfrequenzbereich
1. Aufl. 1993, 126 S.
ISBN 3-86073-174-2
(vergriffen)

ABISEA Band 10
Skudelny, H.-Ch.
Stromrichtertechnik
4. Aufl. 1997, 259 S.
ISBN 3-86073-189-0

ABISEA Band 11
Skudelny, H.-Ch.
Elektrische Antriebe
3. Aufl. 1997, 124 S.
ISBN 3-86073-231-5

ABISEA Band 12
Schöpe, Friedhelm
Batterie-Management für Nickel-Cadmium Akkumulatoren
1. Aufl. 1994, 148 S.
ISBN 3-86073-232-3
(vergriffen)

ABISEA Band 13
v. d. Weem, Jürgen
Schmalbandige aktive Filter für Schienentriebfahrzeuge am Gleichspannungsfahrdraht
1. Aufl. 1995, 126 S.
ISBN 3-86073-233-1

ABISEA Band 14
Backhaus, Klaus
Spannungseinprägendes Direktantriebssystem mit schnelllaufender geschalteter Reluktanzmaschine
1. Aufl. 1995, 146 S.
ISBN 3-86073-234-X
(vergriffen)

ABISEA Band 15
Reinold, Harry
Optimierung dreiphasiger Pulsdauermodulationsverfahren
1. Aufl. 1996, 107 S.
ISBN 3-86073-235-8

ABISEA Band 16
Köpken, Hans-Georg
Regelverfahren für Parallelschwingkreisumrichter
1. Aufl. 1996, 125 S.
ISBN 3-86073-236-6

ABISEA Band 17
Mauracher, Peter
Modellbildung und Verbundoptimierung bei Elektrostraßenfahrzeugen
1. Aufl. 1996, 192 S.
ISBN 3-86073-237-4

ABISEA Band 18
Protiwa, Franz-Ferdinand
Vergleich dreiphasiger Resonanz-Wechselrichter in Simulation und Messung
1. Aufl. 1997, 178 S.
ISBN 3-86073-238-2

ABISEA Band 19
Brockmeyer, Ansgar
Dimensionierungswerkzeug für magnetische Bauelemente in Stromrichteranwendungen
1. Aufl. 1997, 175 S.
ISBN 3-86073-239-0

ABISEA Band 20
Apeldoorn, Oscar
Simulationsgestützte Bewertung von Steuerverfahren für netzgeführte Stromrichter mit verringerter Netzrückwirkung
1. Aufl. 1997, 134 S.
ISBN 3-86073-680-9

ABISEA Band 21
Lohner, Andreas
Batteriemanagement für verschlossene Blei-Batterien am Beispiel von Unterbrechungsfreien Stromversorgungen
1. Aufl. 1998, 126 S.
ISBN 3-86073-681-7

ABISEA Band 22
Reinert, Jürgen
Optimierung der Betriebseigenschaften von Antrieben mit geschalteter Reluktanzmaschine
1. Aufl. 1998, 153 S.
ISBN 3-86073-682-5

ABISEA Band 23
Nagel, Andreas
Leitungsgebundene Störungen in der Leistungselektronik: Entstehung, Ausbreitung und Filterung
1. Aufl. 1999, 140 S.
ISBN 3-86073-683-3

ABISEA Band 24
Menne, Marcus
Drehschwingungen im Antriebsstrang von Elektrostraßenfahrzeugen - Analyse und aktive Dämpfung
1. Aufl. 2001, 169 S.
ISBN 3-86073-684-1

ABISEA Band 25
von Bloh, Jochen
Multilevel-Umrichter zum Einsatz in Mittelspannungs-Gleichspannungs-Übertragungen
1. Aufl. 2001, 137 S.
ISBN 3-86073-685-X

ABISEA Band 26
Karden, Eckhard
Using low-frequency impedance spectroscopy for characterization, monitoring, and modeling of industrial batteries
1. Aufl. 2002, 137 S.
ISBN 3-8265-9766-4

ABISEA Band 27
Karipidis, Claus-Ulrich
A Versatile DSP/ FPGA Structure optimized for Rapid Prototyping and Digital Real-Time Simulation of Power Electronic and Electrical Drive Systems
1. Aufl. 2001, 164 S.
ISBN 3-8265-9738-9

ABISEA Band 28
Kahlen, Klemens
Regelungsstrategien für permanentmagnetische Direktantriebe mit mehreren Freiheitsgraden
1. Aufl. 2002, 154 S.
ISBN 3-8322-1222-1

ABISEA Band 29
Inderka, Robert B.
Direkte Drehmomentregelung Geschalteter Reluktanzantriebe
1. Aufl. 2003, 182 S.
ISBN 3-8322-1175-6

ABISEA Band 30
Schröder, Stefan
Circuit-Simulation Models of High-Power Devices Based on Semiconductor Physics
1. Aufl. 2003, 123 S.
ISBN 3-8322-1250-7

ABISEA Band 31
Buller, Stephan
Impedance-Based Simulation Models for Energy Storage Devices in Advanced Automotive Power Systems
1. Aufl. 2003, 138 S.
ISBN 3-8322-1225-6

ABISEA Band 32
Schönknecht, Andreas
Topologien und Regelungsstrategien für das induktive Erwärmen mit hohen Frequenz-Leistungsprodukten
1. Aufl. 2004, 157 S.
ISBN 3-8322-2408-4

ABISEA Band 33
Tolle, Tobias
Konvertertopologien für ein aufwandsarmes, zweistufiges Schaltnetzteil zum Laden von Batterien aus dem Netz
1. Aufl. 2004, 148 S.
ISBN 3-8322-2676-1

ABISEA Band 34
Götting, Gunther
Dynamische Antriebsregelung von Elektrostraßenfahrzeugen unter Berücksichtigung eines schwingungsfähigen Antriebsstrangs
1. Aufl. 2004, 157 S.
ISBN 3-8322-2804-7

ABISEA Band 35
Dieckerhoff, Sibylle
Transformatorlose Stromrichterschaltungen für Bahnfahrzeuge am 16 2/3Hz Netz
1. Aufl. 2004, 147 S.
ISBN 3-8322-3094-7

ABISEA Band 36
Hu, Jing
Bewertung von DC-DC-Topologien und Optimierung eines DC-DC-Leistungsmoduls für das 42-V-Kfz-Bordnetz
1. Aufl. 2004, 148 S.
ISBN 3-8322-3201-X

ABISEA Band 37
Detjen, Dirk-Oliver
Characterization and Modeling of Si-Si Bonded Hydrophobie Interfaces for Novel High-Power BIMOS Devices
1. Aufl. 2004, 135 S.
ISBN 3-8322-2963-9

ABISEA Band 38
Walter, Jörg
Simulationsbasierte Zuverlässigkeitsanalyse in der modernen Leistungselektronik
1. Aufl. 2004, 121 S.
ISBN 3-8322-3481-0

ABISEA Band 39
Schwarzer, Ulrich
IGBT versus GCT in der Mittelspannungsanwendung - ein experimenteller und simulativer Vergleich
1. Aufl. 2005, 170 S.
ISBN 3-8322-4489-1

ABISEA Band 40
Bartram, Markus
IGBT-Umrichtersysteme für Windkraftanlagen: Analyse der Zyklenbelastung, Modellbildung, Optimierung und Lebensdauervorhersage
1. Aufl. 2006, 185 S.
ISBN 3-8322-5039-5

ABISEA Band 41
Ponnaluri, Srinivas
Generalized Design, Analysis and Control of Grid side converters with integrated UPS or Islanding functionality
1. Aufl. 2006, 163 S.
ISBN 3-8322-5281-9

ABISEA Band 42
Jacobs, Joseph
Multi-Phase Series Resonant DC-to-DC Converters
1. Aufl. 2006, 185 S.
ISBN 3-8322-5532-X

ABISEA Band 43
Linzen, Dirk
Impedance-Based Loss Calculation and Thermal Modeling of Electrochemical Energy Storage Devices for Design Considerations of Automotive Power Systems
1. Aufl. 2006, 185 S.
ISBN 3-8322-5706-3

ABISEA Band 44
Fiedler, Jens
Design of Low-Noise Switched Reluctance Drives
1. Aufl. 2007, 176 S.
ISBN 978-3-8322-5864-1

ABISEA Band 45
Fuengwarodsakul, Nisai
Predictive PWM-based Direct Instantaneous Torque Control for Switched Reluctance Machines
1. Aufl. 2007, 141 S.
ISBN 978-3-8322-6210-5

ABISEA Band 46
Meyer, Christoph
Key Components for Future Offshore DC Grids
1. Aufl. 2007, 187 S.
ISBN 978-3-8322-6571-7

ABISEA Band 47
Fujii, Kansuke
Characterization and Optimization of Soft-Switched Multi-Level Converters for STATCOMs
1. Aufl. 2008, 199 S.
ISBN 978-3-8322-6981-4

ABISEA Band 48
Carstensen, Christian
Eddy Currents in Windings of Switched Reluctance Machines
1. Aufl. 2008, 179 S.
ISBN 978-3-8322-7118-3

ABISEA Band 49
Bohlen, Oliver
Impedance-based battery monitoring
1. Aufl. 2008, 190 S.
ISBN 978-3-8322-7606-5

ABISEA Band 50
Thele, Marc
A contribution to the modelling of the charge acceptance of lead-acid batteries - using frequency and time domain based concepts
1. Aufl. 2008, 165 S.
ISBN 978-3-8322-7659-1

ABISEA Band 51
König, Andreas
High Temperature DC-to-DC Converters for Downhole Applications
1. Aufl. 2009, 154 S.
ISBN 978-3-8322-8489-3

ABISEA Band 52
Dick, Christian Peter
Multi-Resonant Converters as Photovoltaic Module-Integrated Maximum Power Point Tracker
1. Aufl. 2010, 182 S.
ISBN 978-3-8322-9199-0

ABISEA Band 53
Kowal, Julia
Spatially resolved impedance of nonlinear inhomogeneous devices: using the example of lead-acid batteries
1. Aufl. 2010, 203 S.
ISBN 978-3-8322-9483-0

ABISEA Band 54
Roscher, Michael Andreas
Zustandserkennung von LiFeP04-Batterien für Hybrid- und Elektrofahrzeuge
1. Aufl. 2011, 186 S.
ISBN 978-3-8322-9738-1

ABISEA Band 55
Hirschmann, Dirk
Highly Dynamic Piezoelectric Positioning
1. Aufl. 2011, 146 S.
ISBN 978-3-8322-9746-6

ABISEA Band 56
Rigbers, Klaus
Highly Efficient Inverter Architectures for Three-Phase Grid Connection of Photovoltaic Generators
1. Aufl. 2011, 244 S.
ISBN 978-3-8322-9816-9

ABISEA Band 57
Kasper, Knut
Analysis and Control of the Acoustic Behavior of Switched Reluctance Drives
1. Aufl. 2011, 205 S.
ISBN 978-3-8322-9869-2

ABISEA Band 58
Köllensperger, Peter
The Internally Commutated Thyristor - Concept, Design and Application
1. Aufl. 2011, 214 S.
ISBN 978-3-8322-9909-5

ABISEA Band 59
Schoenen, Timo
Einsatz eines DC/DC-Wandlers zur Spannungsanpassung zwischen Antrieb und Energiespeicher in Elektro-und Hybridfahrzeugen
1. Aufl. 2011, 128 S.
ISBN 978-3-8440-0622-3

ABISEA Band 60
Hennen, Martin
Switched Reluctance Direct Drive with Integrated Distributed Inverter
1. Aufl. 2012, 141 S.
ISBN 978-3-8440-0731-2

ABISEA Band 61
van Treek, Daniel
Position Sensorless Torque Control of Switched Reluctance Machines
1. Aufl. 2012, 144 S.
ISBN 978-3-8440-1014-5

ABISEA Band 62
Bragard, Michael
The Integrated Emitter Turn-Off Thyristor. An Innovative MOS-Gated High-Power Device
1. Aufl. 2012, 164 S.
ISBN 978-3-8440-1152-4

ABISEA Band 63
Gerschler, Jochen B.
Ortsaufgelöste Modellbildung von Lithium-Ionen-Systemen unter spezieller Berücksichtigung der Batteriealterung
1. Aufl. 2012, 334 S.
ISBN 978-3-8440-1307-8

ABISEA Band 64
Neuhaus, Christoph R.
Schaltstrategien für Geschaltete Reluktanzantriebe mit kleinem Zwischenkreis
1. Aufl. 2012, 133 S.
ISBN 978-3-8440-1487-7

ABISEA Band 65
Butschen, Thomas
Dual-ICT- A Clever Way to Unite Conduction and Switching Optimized Properties in a Single Wafer
1. Aufl. 2012, 168 S.
ISBN 978-3-8440-1771-7

ABISEA Band 66
Plum, Thomas
Design and Realization of High-Power MOS Turn-Off Thyristors
1. Aufl. 2013, 113 S.
ISBN 978-3-8440-1884-4

ABISEA Band 67
Kiel, Martin
Impedanzspektroskopie an Batterien unter besonderer Berücksichtigung von Batteriesensoren für den Feldeinsatz
1. Aufl. 2013, 226 S.
ISBN 978-3-8440-1973-5

ABISEA Band 68
Brauer, Helge
Schnelldrehender Geschalteter Reluktanzantrieb mit extremem Längendurchmesserverhältnis
1. Aufl. 2013, 192 S.
ISBN 978-3-8440-2345-9

ABISEA Band 69
Thomas, Stephan
A Medium-Voltage Multi-Level DC/DC Converter with High Voltage Transformation Ratio
1. Aufl. 2014, 226 S.
ISBN 978-3-8440-2605-4

ABISEA Band 70
Richter, Sebastian
Digitale Regelung von PWM Wechselrichtern mit niedrigen Trägerfrequenzen
1. Aufl. 2014, 126 S.
ISBN 978-3-8440-2641-2

ABISEA Band 71
Bösing, Matthias
Acoustic Modeling of Electrical Drives - Noise and Vibration Synthesis based on Force Response Superposition
1. Aufl. 2014, 188 S.
ISBN 978-3-8440-2752-5

ABISEA Band 72
Waag, Wladislaw
Adaptive algorithms for monitoring of lithium-ion batteries in electric vehicles
1. Aufl. 2014, 232 S.
ISBN 978-3-8440-2976-5

ABISEA Band 73
Sanders, Tilman
Spatially Resolved Electrical In-Situ Measurement Techniques for Fuel Cells
1. Aufl. 2014, 126 S.
ISBN 978-3-8440-3121-8

ABISEA Band 74
Baumhöfer, Thorsten
Statistische Betrachtung experimenteller Alterungsuntersuchungen an Lithium-Ionen Batterien
1. Aufl. 2015, 157 S.
ISBN 978-3-8440-3423-3

ABISEA Band 75
Andre, Dave
Systematic Characterization of Ageing Factors for High-Energy Lithium-Ion Cells and Approaches for Lifetime Modelling Regarding an Optimized Operating Strategy in Automotive Applications
1. Aufl. 2015, 196 S.
ISBN 978-3-8440-3587-2

ABISEA Band 76
Merei, Ghada
Optimization of off-grid hybrid PV-wind-diesel power supplies with multi-technology battery systems taking into account battery aging
1. Aufl. 2015, 184 S.
ISBN 978-3-8440-4148-4

ABISEA Band 77
Schulte, Dominik
Modellierung und experimentelle Validierung der Alterung von Blei-Säure Batterien durch inhomogene Stromverteilung und Säureschichtung
1. Aufl. 2016, 165 S.
ISBN 978-3-8440-4216-0

ABISEA Band 78
Schenk, Mareike
Simulative Untersuchung der Wicklungsverluste in Geschalteten Reluktanzmaschinen
1. Aufl. 2016, 126 S.
ISBN 978-3-8440-4282-5

ABISEA Band 79
Wang, Yu
Development of Dynamic Models with Spatial Resolution for Electrochemical Energy Converters as Basis for Control and Management Strategies
1. Aufl. 2016, 188 S.
ISBN 978-3-8440-4303-7

ABISEA Band 80
Ecker, Madeleine
Lithium Plating in Lithium-Ion Batteries:
An Experimental and Simulation Approach
1. Aufl. 2016, 154 S.
ISBN 978-3-8440-4525-3

ABISEA Band 81
Zhou, Wei
Modellbasierte Auslegungsmethode von Temperierungssystemen für Hochvolt-Batterien in Personenkraftfahrzeugen
1. Aufl. 2016, 175 S.
ISBN 978-3-8440-4589-5

ABISEA Band 82
Lunz, Benedikt
Deutschlands Stromversorgung im Jahr 2050
Ein szenariobasiertes Verfahren zur vergleichenden Bewertung von Systemvarianten und Flexibilitätsoptionen
1. Aufl. 2016, 187 S.
ISBN 978-3-8440-4627-4

ABISEA Band 83
Hofmann, Andreas G.
Direct Instantaneous Force Control: Key to Low-Noise Switched Reluctance Traction Drives
1. Aufl. 2016, 228 S.
ISBN 978-3-8440-4715-8

ABISEA Band 84
Budde-Meiwes, Heide
Dynamic Charge Acceptance of Lead-Acid Batteries for Micro-Hybrid Automotive Applications
1. Aufl. 2016, 157 S.
ISBN 978-3-8440-4733-2

ABISEA Band 85
Engel, Stefan P.
Thyristor-Based High-Power On-Load Tap Changers Control under Harsh Load Conditions
1. Aufl. 2016, 156 S.
ISBN 978-3-8440-4986-2

ABISEA Band 86
Van Hoek, Hauke
Design and Operation Considerations of Three-Phase Dual Active Bridge Converters for Low-Power Applications with Wide Voltage Ranges
1. Aufl. 2017, 231 S.
ISBN 978-3-8440-5011-0

ABISEA Band 87
Diekhans, Tobias
Wireless Charging of Electric Vehicles - a Pareto-Based Comparison of Power Electronic Topologies
1. Aufl. 2017, 151 S.
ISBN 978-3-8440-5048-6

ABISEA Band 88
Lehner, Susanne
Reliability Assessment of Lithium-Ion Battery Systems with Special Emphasis on Cell Performance Distribution
1. Aufl. 2017, 184 S.
ISBN 978-3-8440-5090-5

ABISEA Band 89
Käbitz, Stefan
Untersuchung der Alterung von Lithium-Ionen-Batterien mittels Elektroanalytik und elektrochemischer Impedanzspektroskopie
1. Aufl. 2016, 258 S.
DOI: 10.18154/RWTH-2016-12094

ABISEA Band 90
Witzenhausen, Heiko
Elektrische Batteriespeichermodelle: Modellbildung, Parameteridentifikation und Modellreduktion
1. Aufl. 2017, 266 S.
DOI: 10.18154/RWTH-2017-03437

ABISEA Band 91
Münnix, Jens
Einfluss von Stromstärke und Zyklentiefe auf graphitische Anoden
1. Aufl. 2017, 171 S.
DOI: 10.18154/RWTH-2017-01915

ABISEA Band 92
Pilatowicz, Grzegorz
Failure Detection and Battery Management Systems of Lead-Acid Batteries for Micro-Hybrid Vehicles
1. Aufl. 2017, 212 S.
DOI: 10.18154/RWTH-2017-09156

ABISEA Band 93
Drillkens, Julia
Aging in Electrochemical Double Layer Capacitors: An Experimental and Modeling Approach
1. Aufl. 2017, 179 S.
DOI: 10.18154/RWTH-2018-223434

ABISEA Band 94
Magnor, Dirk
Globale Optimierung netzgekoppelter PV-Batteriesysteme unter besonderer Berücksichtigung der Batteriealterung
1. Aufl. 2017, 210 S.
DOI: 10.18154/RWTH-2017-06592

ABISEA Band 95
Iliksu, Merve
Elucidation and Comparison of the Effects of Lithium Salts on Discharge Chemistry of Nonaqueous Li-O_2 Batteries
1. Aufl. 2018, 160 S.
DOI: 10.18154/RWTH-2018-223782

ABISEA Band 96
Schmalstieg, Johannes
Physikalisch-elektrochemische Simulation von Lithium-Ionen-Batterien: Implementierung, Parametrierung und Anwendung
1. Aufl. 2017, 168 S.
DOI: 10.18154/RWTH-2017-04693

ABISEA Band 97
Soltau, Nils
High-Power Medium-Voltage DC-DC Converters: Design, Control and Demonstration
1. Aufl. 2017, 176 S.
DOI: 10.18154/RWTH-2017-04084

ABISEA Band 98
Stieneker, Marco
Analysis of Medium-Voltage Direct-Current Collector Grids in Offshore Wind Parks
1. Aufl. 2017, 144 S.
DOI: 10.18154/RWTH-2017-04667

ABISEA Band 99
Masomtob, Manop
A New Conceptual Design of Battery Cell with an Internal Cooling Channel
1. Aufl. 2017, 167 S.
DOI: 10.18154/RWTH-2018-223281

ABISEA Band 100
Marongiu, Andrea
Performance and Aging Diagnostic on Lithium Iron Phosphate Batteries for Electric Vehicles and Vehicle-to-Grid Strategies
1. Aufl. 2017, 222 S.
DOI: 10.18154/RWTH-2017-09944

ABISEA Band 101
Gitis, Alexander
Flaw detection in the coating process of lithium-ion battery electrodes with acoustic guided waves
1. Aufl. 2017, 109 S.
DOI: 10.18154/RWTH-2017-099519

ABISEA Band 102
Neeb, Christoph
Packaging Technologies for Power Electronics in Automotive Applications
1. Aufl. 2017, 132 S.
DOI: 10.18154/RWTH-2018-224569

ABISEA Band 103
Adler, Felix
A Digital Hardware Platform for Distributed Real-Time Simulation of Power Electronic Systems
1. Aufl. 2017, 156 S.
DOI: 10.18154/RWTH-2017-10761

ABISEA Band 104
Becker, Jan
Flexible Dimensionierung und Optimierung hybrider Lithium-Ionenbatterie-speichersysteme mit verschiedenen Auslegungs-zielen
1. Aufl., 2017, 157 S.
DOI: 10.18154/RWTH-2017-09278

ABISEA Band 105
Warnecke, Alexander J.
Degradation Mechanisms in NMC Based Lithium-Ion Batteries
1. Aufl. 2017, 158 S.
DOI: 10.18154/RWTH-2017-09646

ABISEA Band 106
Taraborrelli, Silvano
Bidirectional Dual Active Bridge Converter using a Tap Changer for Extended Voltage Ranges
1. Aufl. 2017, 94 S.
DOI: 10.18154/RWTH-2018-228242

ABISEA Band 107
Sarriegi, Garikoitz
SiC and GaN Semiconductors: The Future Enablers of Compact and Efficient Converters for Electromobility
1. Aufl. 2017, 106 S.
DOI: 10.18154/RWTH-2018-227548

ABISEA Band 108
Senol, Murat
Drivetrain Integrated Dc-Dc Converters utilizing Zero Sequence Currents
1. Aufl. 2017, 134 S.
DOI: 10.18154/RWTH-2018-226170

ABISEA Band 109
Kojima, Tetsuya
Efficiency Optimized Control of Switched Reluctance Machines
1. Aufl. 2017, 142 S.
DOI: 10.18154/RWTH-2018-226697

ABISEA Band 110
Lewerenz, Meinert
Dissection and Quantitative Description of Aging of Lithium-Ion Batteries Using Non-Destructive Methods Validated by Post-Mortem-Analyses
1. Aufl. 2018, 139 S.
DOI: 10.18154/RWTH-2018-228663

ABISEA Band 111
Büngeler, Johannes
Optimierung der Verfügbarkeit und der Lebensdauer von Traktionsbatterien für den Einsatz in Flurförderfahrzeugen
1. Aufl. 2018, 171 S.
DOI: 10.18154/RWTH-2018-226569

ABISEA Band 112
Wegmann, Raphael
Betriebsstrategien und Potentialbewertung hybrider Batteriespeichersysteme in Elektrofahrzeugen
1. Auflage 2018, 184 S.
DOI: 10.18154/RWTH-2018-228833

ABISEA Band 113
Nordmann, Hannes
Batteriemanagementsysteme unter besonderer Berücksichtigung von Fehlererkennung und Peripherieanalyse
1. Aufl. 2018, 222 S.
DOI: 10.18154/RWTH-2018-228763

ABISEA Band 114
Engelmann, Georges
Reducing Device Stress and Switching Losses Using Active Gate Drivers and Improved Switching Cell Design
1. Aufl. 2018, 195 S.
DOI: 10.18154/RWTH-2018-228973

ABISEA Band 115
Klein-Heßling, Annegret
Active DC-Power Filters for Switched Reluctance Drives during Single-Pulse Operation
1. Aufl. 2018, 166 S.
DOI: 10.18154/RWTH-2018-231030

ABISEA Band 116
Burkhart, Bernhard
Switched Reluctance Generator for Range Extender Applications - Design, Control and Evaluation
1. Aufl. 2018, 194 S.
DOI: 10.18154/RWTH-2019-00025

ABISEA Band 117
Biskoping, Matthias
Discrete Modeling and Control of a versatile Power Electronic Test Bench with Special Focus on Central Photovoltaic Inverter Testing
1. Aufl. 2018, 236 S.
DOI: 10.18154/RWTH-2019-03346

ABISEA Band 118
Schubert, Michael
High-Precision Torque Control of Inverter-Fed Induction Machines with Instantaneous Phase Voltage Sensing
1. Aufl. 2019, 221 S.
DOI: 10.18154/RWTH-2018-231364

ABISEA Band 119
Van der Broeck, Christoph
Methodology for Thermal Modeling, Monitoring and Control of Power Electronic Modules
1. Aufl. 2019, 290 S.
DOI: 10.18154/RWTH-2019-01370

ABISEA Band 120
Hust, Friedrich Emanuel
Physico-chemically motivated parameterization and modelling of real-time capable lithium-ion battery models – a case study on the Tesla Model S battery
1. Aufl. 2019, 203 S.
DOI: 10.18154/RWTH-2019-00249

ABISEA Band 121
Ralev, Iliya
Accurate Torque Control of Position Sensorless Switched Reluctance Drives
1. Aufl. 2019, 154 S.
DOI: 10.18154/RWTH-2019-03071

ABISEA Band 122
Ayeng'o, Sarah Paul
Optimization of number of PV cells connected in series for a direct-coupled PV system with lead-acid and lithium-ion batteries
1. Aufl. 2019, 114 S.
DOI: 10.18154/RWTH-2019-01843

ABISEA Band 123
Koschik, Stefan Andreas
Permanenterregte Synchronmaschinen mit verteilter Einzelzahnsteuerung - Regelkonzepte und Betriebsstrategien für hochintegrierte Antriebssysteme
1. Aufl. 2019, 158 S.
DOI: 10.18154/RWTH-2019-03446

ABISEA Band 124
Farmann, Alexander
A comparative study of reduced-order equivalent circuit models for state-of-available-power prediction of lithium-ion batteries in electric vehicles
1. Aufl. 2019, 214 S.
DOI: 10.18154/RWTH-2019-04700

ABISEA Band 125
Mareev, Ivan
Analyse und Bewertung von batteriegetriebenen, oberleitungsversorgten und brennstoffzellengetriebenen Lastkraftwagen für den Einsatz im Güterfernverkehr in Deutschland
1. Aufl. 2019, 158 S.
DOI: 10.18154/RWTH-2019-04698

ABISEA Band 126
Qi, Fang
Online Model-predictive Thermal Management of Inverter-fed Electrical Machines
1. Aufl. 2019, 154 S.
DOI: 10.18154/RWTH-2019-08304

ABISEA Band 127
Kairies, Kai-Philipp
Auswirkungen dezentraler Solarstromspeicher auf Netzbetreiber und Energieversorger
1. Aufl. 2019, 140 S.
DOI: 10.18154/RWTH-2019-06706

ABISEA Band 128
Fleischer, Michael
Traction control for Railway Vehicles
1. Aufl. 2019, 162 S.
DOI: 10.18154/RWTH-2019-10570

ABISEA Band 129
Teuber, Moritz
Lifetime Assessment and Degradation Mechanisms in Electric Double-Layer Capacitors
1. Aufl. 2019, 150 S.
DOI: 10.18154/RWTH-2019-10071

ABISEA Band 130
Bußar, Christian
Investigation of Optimal Transformation Pathways towards 2050 for the Successful Implementation of a Sustainable Reduction of Carbon Emissions from Power Generation
1. Aufl. 2019, 204 S.
DOI: 10.18154/RWTH-2019-09975

ABISEA Band 131
Wienhausen, Arne Hendrik
High Integration of Power Electronic Converters enabled by 3D Printing
1. Aufl. 2019, 146 S.
DOI: 10.18154/RWTH-2019-08746

ABISEA Band 132
Kwiecien, Monika
Electrochemical Impedance Spectroscopy on Lead-Acid Cells during Aging
1. Aufl. 2019, 138 S.
DOI: 10.18154/RWTH-2019-09480

ABISEA Band 133
Titiz, Furkan Kaan
A Three-phase Low-voltage Grid-connected Current Source Inverter
1. Aufl. 2019, 128 S.
DOI: 10.18154/RWTH-2020-00458

ABISEA Band 134
Wünsch, Martin
Separation der Kathoden-alterung in Lithium-Ionen-Batteriezellen mittels elektrochemischer Impedanzspektroskopie
1. Aufl. 2019, 177 S.
DOI: 10.18154/RWTH-2019-11017

ABISEA Band 135
Badeda, Julia
Modeling and Steering of Multi-Use Operation with Uninterruptible Power Supply Systems - utilizing the example of lead-acid batteries
1. Aufl. 2020, 282 S.
DOI: 10.18154/RWTH-2020-05456

ABISEA Band 136
Kleinsteinberg, Björn
Energy Efficiency Increase of a Vanadium Redox Flow Battery with a Power-Based Model
1. Aufl. 2020, 163 S.
DOI: 10.18154/RWTH-2020-06092

ABISEA Band 137
Cai, Zhuang
Optimization of dimension and operation strategy for a wind-battery energy system in German electricity market under consideration of battery ageing process
1. Aufl. 2020, 144 S.
DOI: 10.18154/RWTH-2020-06525

ABISEA Band 138
Sabet, Pouyan Shafiei
Analysis of Predominant Processes in Electrochemical Impedance Spectra and Investigation of Aging Processes of Lithium-Ion Batteries with Layered Oxide Cathodes and Graphitic Anodes
1. Aufl. 2020, 136 S.
DOI: 10.18154/RWTH-2020-07683

ABISEA Band 139
Angenendt, Georg
Operation, Optimization and Additional Market Participation of Households with PV Battery Storage System and Power-to-Heat Application
1. Aufl. 2020, 221 S.
DOI: 10.18154/RWTH-2020-05200

ABISEA Band 140
Oberdieck, Karl Friedrich
Measurement and Mitigation of Electromagnetic Emissions of Propulsion Inverters for Electric Vehicles
1. Aufl. 2020, 181 S.
DOI: 10.18154/RWTH-2020-09215

ABISEA Band 141
Bubert, Andreas Martin
Optimierung des elektrischen Antriebsstrangs von Elektrofahrzeugen mit Betrachtung parasitärer Ströme innerhalb der elektrischen Maschine
1. Aufl. 2020, 215 S.
DOI: 10.18154/RWTH-2020-09556

ABISEA Band 142
Fleischer, Christian Georg
Model-Driven Software Development and Verification Solutions for Safety Critical Battery Management Systems
1. Aufl. 2021, 356 S.
DOI: 10.18154/RWTH-2021-00436

ABISEA Band 143
Arzberger, Arno
Thermografische Methoden zur zerstörungsfreien Messung der anisotropen Wärmeleitfähigkeit von Lithium-Ionen Zellen
1. Aufl. 2020, 131 S.
DOI: 10.18154/RWTH-2021-00479

ABISEA Band 144
Lange, Tobias
Oberwellenbasierte Modellierung, Regelung und Auslegung von Permanentmagnet- und Reluktanz-Synchronmaschinen
1. Aufl. 2020, S.
DOI: 10.18154/RWTH-2021-02537

ABISEA Band 145
Weiss, Claude
Fault Tolerant Switched Reluctance Machines with Distributed Inverters – Modeling and Control
1. Aufl. 2020, S.
DOI: 10.18154/RWTH-2021-02327

ABISEA Band 146
Huck, Moritz
Modelling the Transient Behaviour of Lead-Acid Batteries: Electrochemical Impedance of Adsorbed Species
1. Aufl. 2020, 151 S.
DOI: 10.18154/RWTH-2020-08362

ABISEA Band 147
Willenberg, Lisa
Volumenausdehnung und ihre Auswirkungen auf die Alterung einer zylindrischen Lithium-Ionen-Batterie
1. Aufl. 2020, S.
DOI: 10.18154/RWTH-2021-01906

ABISEA Band 148
Rogge, Matthias
Electrification of Public Transport Bus Fleets with Battery Electric Busses
1. Aufl. 2020, 161 S.
DOI: 10.18154/RWTH-2021-02146

ABISEA Band 149
Münderlein, Jeanette
Numerische Methodik zur Auslegung eines Hybriden Speichersystems mit Multinutzen“
1. Aufl. 2020, 221 S.
DOI: 10.18154/RWTH-2021-00867

ABISEA Band 150
Merten, Michael
Participation of Battery Storage Systems in the Secondary Control Reserve Market
1. Aufl. 2020, 187 S.
DOI: 10.18154/RWTH-2021-01029

ABISEA Band 151
Ge, Lefei
Performance Enhancement of Switched Reluctance Machines for High-speed Back-up Generators
1. Aufl. 2020, 152 S.
DOI: 10.18154/RWTH-2020-11546

ABISEA Band 152
Neubert, Markus
Modeling, Synthesis and Operation of Multiport-Active Bridge Converters
1. Aufl. 2020, 227 S.
DOI: 10.18154/RWTH-2020-10814

ABISEA Band 153
Schülting, Philipp
Optimierte Auslegung von hochintegrierten und bidirektionalen Onboard GaN-Ladegeräten
1. Aufl. 2020, 158 S.
DOI: 10.18154/RWTH-2020-09771

ABISEA Band 154
Sewergin, Alexander
Design Challenges and Solutions for the Practical Application of SiC Power Moduls – Exemplified by an Automotive DC-DC Converter. 1. Aufl. 2021, 154 S.
DOI: 10.18154/RWTH-2021-04498

ABISEA Band 155
Stippich, Alexander
Exploiting the Full Potential of Silicon Carbide Devices via Optimized Highly Integrated Power Modules
1. Aufl. 2021, 188 S.
DOI: 10.18154/RWTH-2021-08122

ABISEA Band 156
Gottschlich, Jan
Hilfsspannungsversorgungskonzepte für Mittelspannungs-DC/DC-Wandler
1. Aufl. 2021, 178 S.
DOI: 10.18154/RWTH-2021-11881

ABISEA Band 157
Hollstegge, Philipp
Injektion raumzeigerzerlegter Stromharmonischer zur Minderung tonaler Geräuschanteile in asymmetrisch sechsphasigen Permanentmagnetsynchronmaschinen
1. Aufl. 2021, 191 S.
DOI: 10.18154/RWTH-2021-11040

ABISEA Band 158
Grau, Vivien
Development of a Test Bench to Investigate the Impact of Steep Voltage Slopes on the Lifetime of Insulation Systems for Coil Windings
1. Aufl. 2021, 182 S.
DOI: 10.18154/RWTH-2021-09577

ABISEA Band 159
Ringbeck, Florian
Optimized Charging of Lithium-Ion Batteries with Physico-Chemical Models
1. Aufl. 2021, 174 S.
DOI: 10.18154/RWTH-2021-11038

ABISEA Band 160
Bank, Thomas
Performance and Aging Analysis of High-Power Lithium Titanate Oxide Cells for Low-Voltage Vehicle Applications
1. Aufl. 2021, 148 S.
DOI: 10.18154/RWTH-2021-10369

ABISEA Band 161
Aupperle, Felix
Realizing High-Performance Silicon-Based Lithium-Ion Batteries
1. Aufl. 2022, 138 S.
DOI: 10.18154/RWTH-2022-05155

ABISEA Band 162
Schröer, Philipp A.
Entwicklung einer adaptiven Leistungsprognosefunktion für Starterbatterien mit Lithium-Titanat-Oxid-Anode als Grundlage zur sicheren Energieversorgung im Fahrzeug
1. Aufl. 2021, 187 S.
DOI: 10.18154/RWTH-2021-10819

ABISEA Band 163
Dechent, Philipp
Simulation and Real-Life assessment of cell-to-cell variation of ageing lithium-ion batteries
1. Aufl. 2022, 149 S.
DOI: 10.18154/RWTH-2022-09298

ABISEA Band 164
Li, Weihan
Battery Digital Twin with Physics-Based Modeling, Battery Data and Machine Learning
1. Aufl. 2022, 234 S.
DOI: 10.18154/RWTH-2022-02292

ABISEA Band 165
Thien, Tjark G. C.
Optimaler Betrieb von stationären Hybrid-Batteriespeichern am Beispiel des Projekts M5BAT
1. Aufl. 2022, 172 S.
DOI: 10.18154/RWTH-2022-00997

ABISEA Band 166
Lüdecke, Christoph
Compensating Asymmetries of Parallel-Connected SiC MOSFETs Using Intelligent Gate Drivers
1. Aufl. 2022, 166 S.
DOI: 10.18154/RWTH-2022-09587

ABISEA Band 167
Rahe, Christiane
Untersuchung von Batterieelektroden mit optischen Verfahren
1. Aufl. 2022, 214 S.
DOI: 10.18154/RWTH-2022-08794

ABISEA Band 168
Weber, Felix Martin
Stability of lithium electrolyte interphase enabling rechargeable lithium-metal batteries
1. Aufl. 2023, S.
DOI:

ABISEA Band 169
Henn, Jochen
Gate Driver Integrated Closed-Loop Control for Electromagnetic Emissions and Switching Losses of Wide Bandgap Power Electronic Converters
1. Aufl. 2023, S.
DOI:

Highly integrated e-axles, combining inverter, electrical machine and a gearbox in one housing, feature high power densities and short current paths between inverter and machine. However, the parasitic currents flowing in these integrated e-axles can be much higher compared to the parasitic currents in conventional e-drives due to the reduced parasitic inductances and increased parasitic capacitances.

With the increased use of wide-bandgap semiconductor devices with very fast switching transients in these highly integrated e-axles, the impact of parasitic currents grows. These parasitic currents can have a negative impact on electromagnetic compatibility and the lifetime of bearings and gearboxes in the drive.

This thesis presents an in-depth investigation of parasitic effects in electrical drives, putting emphasis on physics-based models of the electrical machine and the bearings. Herein, the influence of different failure modes of the machine on the parasitic currents is investigated and fault detection methods are derived and evaluated.

ISSN 1437-675X